Study on Size Effect of Cluster Ion Beam Irradiation

Kazuya Ichiki

February 2012

Abstract

A gas cluster is an aggregate of more than several hundred atoms. Each constituent atom of a keV energetic gas cluster ion has thus only a few eV of energy. When an energetic gas cluster ion strikes a target surface, each constituent atom hits the local area at the same time and multiple-collision processes occur. It was found that the irradiation effects induced by cluster ion exceed by far the sum of all the individual irradiation effects of its constituent atoms. Such so called "cluster size effects", and many unique phenomena such as high sputtering yield and surface smoothing under large gas cluster ion beam (GCIB) bombardment have been observed. GCIB has therefore recently been proposed to serve as a powerful tool for surface smoothing, surface analysis and film formation.

In studies based on molecular dynamics simulation, we found that the effects of irradiation with large cluster ions on defect formation and sputtering depend on both the incident cluster size and energy of each constituent atom (energy per atom), suggesting that the optimum irradiation conditions for surface-smoothing with GCIB would differ from those for fast etching. Nevertheless, in literature there are only a few experimental studies on the relationship between incident cluster size and irradiation effects with large GCIB. Indeed the usual distribution of sizes in the beam has a range of more than several thousand atoms and therefore the irradiation effects of a cluster of specific size cannot be measured experimentally without size selection. In this work, we thus investigate the effects of cluster size and energy per atom on the interactions between GCIB and organic or inorganic targets. The cluster size was selected with a time-of-flight method, which permits effective cluster size selection, whether light(small) or heavy(large) clusters are to be selected. The irradiation effects investigated were sputtering, secondary ion emission, surface damaging and surface roughening.

Fundamentally, the amount of irradiation effects were found to decrease monotonously with decreasing incident energy per atom, which the effect of cluster size was relatively low. For example, the enhancement factor of Si sputtering yield with GCIB was about 10 regardless of cluster size. This is attributed to a saturation of the cluster size effects, the gas cluster being sufficiently large abobe an initial threshold. The threshold energy per atom for sputtering was found to depend on the incident cluster size and the type of effect. The irradiation effects on organic and inorganic targets were also found to be different, and this was mainly attributed to the difference in target atoms binding energy and structures. In conclusion, different irradiation effects could be specifically obtained by using size-controlled GCIB. The use of GCIB in nanoprocesses such as no-damage surface smoothing of inorganic materials or 3-dimensional secondary ion mass spectrometry imaging of organic samples has thus been enabled by size selection.

Acknowledgments

I would like to express my deep gratitude to Professor Akio Itoh and Associate Professor Jiro Matsuo of Kyoto University for many helpful discussions, their continuous guidance, encouragement throughout this study and giving me the opportunity to complete this work.

I am very grateful to lecturer Toshio Seki and Takaaki Aoki for their comments, scientific advice and helpful discussions in this study. I would like to thank to Associate Professor Hiromi Shibata, Hidetsugu Tsuchida, Assistant Professor Makoto Imai and Takuya Majima for valuable assistance and stimulating comments. I also show my thanks to Chief in editor of Edite Associate Rafael Manory for helpful comments in correcting and improving the English in my papers. I wish to thank Ms. Masae Mogami and Ms. Sachi Ibuki for their continuous cooperation and encourgement.

This research was made possible by the many cooperation and assistance of many students and research fellows at Kyoto University. I would like to thank to Mr. Syunnichiro Nakagawa, Mr. Yasuyuki Yamamoto and Mr. Takahumi Yamanobe for analytical support and kind discussions. I also show my thanks to Mr. Yoshinobu Wakamatsu, Mr. Yusaku Hontani and Mr. Sho Shitomoto for sparing the time for discussion and continuous encouragement in this work. I would like to express my thanks to Dr. Matthieu Py for kind comments in my paper.

To Assistant Professor Satoshi Ninomiya of University of Yamanashi, I would like to show my hearty thanks for significant discussion and experimental advice. To Dr. Yoshihiko Nakata and Dr. Masaki Hada, I would like to show deep gratitude for helpful discussions and many advices in solving the problems. I wish to thank to Professor Hubert Gnaser of University of Kaiserslautern for their helpful discussions.

Finally, I especially thank my parents and brothers for their continuous

care, support and encouragement.

Contents

1 Introduction **1**
1.1 What are clusters? 1
1.2 Interaction between cluster ion and solids 2
1.3 GCIB applications for nano-processing 5
1.4 Purpose of this study 8

2 Sputtering yield with GCIB **11**
2.1 Sputtering effects of ion beam bombardment 11
2.2 Size select GCIB irradiation 16
2.3 Results-Si target 23
2.4 Results-PMMA target 32

3 Secondary ion emission with GCIB **39**
3.1 Secondary ion mass spectrometry 39
3.2 Size-selected cluster SIMS 40
3.2.1 Time-of-flight mass spectrometry 40
3.2.2 Size selected SIMS 42
3.3 Results-Si target 46
3.3.1 Secondary cluster ion emission 46
3.3.2 Enhancement of Si^+ emission 51
3.4 Results-Organic materials 57

4 Surface damage with GCIB **69**
4.1 Low damage processing with GCIB irradiation 69
4.2 Surface damage-Si target 75
4.3 Surface damage-Organic materials 82

5 Surface morphology with GCIB **91**
5.1 Surface smoothing with GCIB irradiation 91
5.2 Surface morphology-Si target 92
5.3 Surface morphology-PMMA target 99

6 Summary and conclusions **107**

7 Appendix **109**
7.1 Energy loss during transportation 109

References **119**

Chapter 1

Introduction

1.1 What are clusters?

It is well known that the physical and chemical properties of matter change from the isolated atom to bulk materials. For example, bulk mercury has the properties of a metal; however, an isolated mercury atom does not behave as metal anymore. The 'cluster' has been studied as the additional phase that stands between the isolated atom and the bulk solid. The word 'cluster' means "a number of things that are grouped close together", and in this study these 'things' are atoms or molecules.

A cluster consists of more than two atoms or molecules that are bound by various binding forces. The characteristics of a small cluster that consists of a few atoms are similar to the isolated atom because all atoms are at the surface of the cluster. On the other hand, the characteristic of large clusters that consist of more than millions of atoms would be similar to the bulk materials because only a small percent of atoms are at the surface. In the case of band gap energy of mercury cluster, an insulator-to-metal transition occurs at an intermediate cluster size, which is about 400 atoms [1)]. The understanding of clusters is by itself very important in fundamental research, because clusters have a potential role in many fields of application and technology.

Clusters can be roughly classified according to their binding force. Van der Waals clusters, such as Ar_n and $(O_2)_n$ are agglomerated by van der Waals forces, and their binding energies are very weak (less than 0.1 eV). Ionic clusters, such as $(NaCl)_n$ and $Ir_4(CO)_{12}$ are held together by ionic

bonding, and their binding energies are relatively strong (2 to 4 eV). Molecular clusters, such as $(I_2)_n$ are bound by dispersive electrostatic bonds, and their bonding strength is between van der Waals and ionic bonding. Hydrogen-bonded clusters, such as $(H_2O)_n$ are associated by intermolecular H-bonding whose strength is as strong as molecular clusters. Valence clusters, such as C_n and Si_n are held together by covalent chemical bonds, which are as strong as the ionic bonds. Metal clusters, such as Cu_n and Au_n are bound together by metallic or covalent bonds, and their binding energies are in the range of a few eV. The properties of clusters are strongly dependent on the type of bond and cluster size.

1.2 Interaction between cluster ion and solids

Not only the physical and chemical properties of the cluster itself, but the interactions between energetic clusters and solids as well have attracted much interest in the research community. When an energetic cluster bombards the solid surface, clusters are broken up, and the constituents of the cluster deposit the energy in the local area at the same time. Some phenomena such as sputtering, are enhanced with energetic cluster bombardment compared with energetic atom bombardment. In addition, some unique phenomena, such as high chemical reactivity are achieved. Therefore, cluster has been proposed as an ion beam source, and a vast quantity of experimental data has been reported since the 1970's. Figure 1.1 represents the typical clusters that have been used for ion beam sources. Their size and structure is also shown.

The irradiation effect of cluster ion was first documented by Andersen and Bay in 1974 by comparing dimers to monomers [2), and the irradiated cluster ion was a metal cluster. Metal clusters are usually formed by laser evaporation, field evaporation or inert gas condensation, and the size of the cluster is up to about 15 atoms. Metal cluster formation was reported for various metal atoms, and works on the irradiation effects of metal cluster ion have accumulated since 1974. However, the quantity of metal clusters produced decreases with cluster size and large metal clusters are difficult to use. Metal cluster complexes are chemically synthesized from organometal-

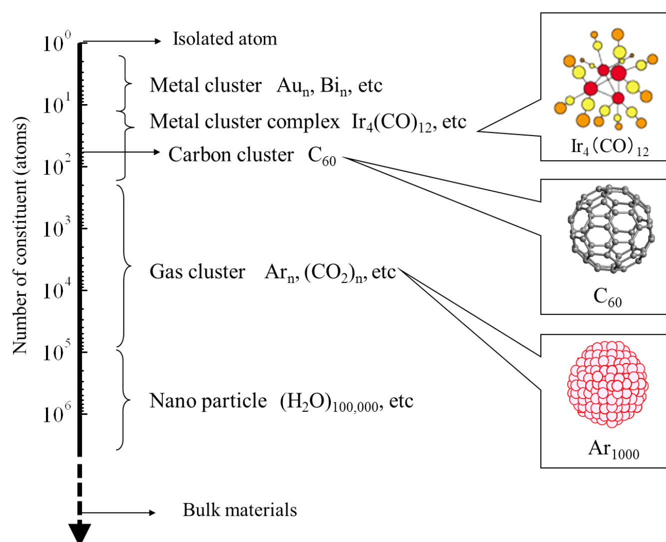

Figure 1.1: The size and structure of typical clusters

lic compounds such as $Ir_4(CO)_{12}$ and $Os_3(CO)_{12}$, and they are larger than typical metal clusters [3, 4]. They consist of a metallic framework of several metal atoms and surrounding ligands that are bound by covalent chemical bonds. A metal cluster complex ion is relatively easy to produce to the specific mass of a large cluster ion.

Fullerenes (C_{60}) are one of the valence clusters and its soccer ball-like structure is well known. C_{60} was discovered by Kroto and Smally in 1985 [5] as a new form of the element carbon, whose properties differ from those of diamond or graphite. The study and application of C_{60} advanced in 1990's because of the discovery and development of a method of mass synthesis by Krätschmer [6]. The number of constituent atoms in C_{60} is much larger than in metal clusters, but its mass (720 u) is roughly the same than small metal clusters such as Au_3 (591 u) and Bi_3 (627 u).

Metal and carbon cluster ion beam presents however some problems. For example, their constituents can be deposited on the surface if operated under low-energy ion bombardment. Furthermore, the applicable cluster size is small.

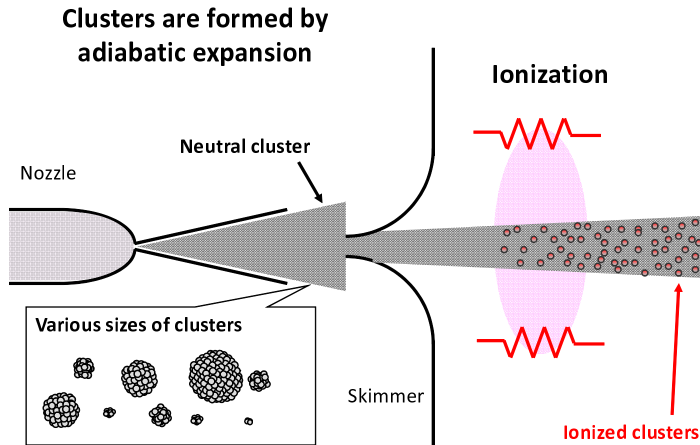

Figure 1.2: Schematic representation of gas cluster formation and ionization

On the other hand, gas cluster is an aggregate of more than hundreds of gaseous atoms, and it is formed by gas expansion in vacuum. The size of gas clusters is much larger than that of metal and carbon clusters, and their constituents atoms evaporate from the surface after irradiation. A method for the generation and irradiation of large gas cluster ions has been developed at Kyoto University since 1990's [7].

Figure 1.2 represents the model of gas cluster ion formation and ionization. When a high-pressure gas is ejected into vacuum through a nozzle shaped like a trumpet, the atoms momenta align with the beam direction. The velocity of the gas atoms are in the range of a hundred to a thousand meters per second. However, adiabatic expansion reduces the relative velocity of the gaseous atoms and, as a result, clusters are formed. Shockwaves generated by supersonic flow ejection from the nozzle disturb the generation of neutral clusters and break the formed clusters. The emplacement of shockwave formation can be calculated, and depend on the throat diameter of the nozzle, the pressure of the inlet gas and the pressure in the vacuum chamber. When the throat diameter of the nozzle, the pressure of inlet gaseous and vacuum chamber are respectively of 0.1 mm, 0.6 MPa and 1 Pa, a shockwave forms at a distance of 20 mm from the nozzle edge.

To avoid the formation of such a shockwave, the skimmer is placed at the center of the cluster beam flow and at about 20 mm from the nozzle edge. Neutral clusters are introduced into the ionization chamber, and are ionized by energized electrons emitted from a hot tungsten filament.

1.3 GCIB applications for nano-processing

When a gas cluster ion beam (GCIB) bombards a solid surface, thousands of atoms strike the surface at the same time. The cluster energy is divided to each constituent when cluster ion is broken up on the solid surface. For example, a single constituent atom of 10 keV Ar_{1000} bears only 10 eV. Individual atomic ion bombardment with the energy of 10 eV hardly penetrates the surface because the binding energy of inorganic atoms is more than a few eV. However, 10 keV Ar_{1000} cluster penetrates a solid surface such as silicon, and induces various irradiation effects, which are fundamentally different from those associated with atomic or small cluster ion impact. The characteristics of GCIB are enumerated below.

1. Low charge-to-mass ratio: an ionized gas cluster carries only single or double charge, despite a cluster size of more than several hundred atoms. Therefore, the space-charge repulsion of GCIB is small in high-current ion beam transport, although the beam velocity is very low. Because of this, GCIB can also avoid the charge-up effect during ion beam irradiation.

2. Low-velocity bombardment: as mentioned, a typical gas cluster ion has energy of a few tens eV/atom because the number of atoms in the gas cluster is more than several hundreds. Consequently, the damaged layer thickness under GCIB irradiation is very shallow compared to atomic ion beam irradiation at comparable total energy. This characteristic can be also applied to shallow implantation.

3. Strong chemical reaction: When an energetic GCIB bombards the surface, the clusters transfer their energy to a very local and shallow area on the solid surface. Surface atoms are excited by the GCIB

irradiation, resulting inan increase of the chemical reactions near the surface with incident cluster species or atmospheric gas. Therefore, the sputtering yield of a cluster ion of nonreactive gas is more than one order of magnitude higher than that of atomic ions, and that of a reactive GCIB is more than two orders of magnitude higher than that of atomic ion at equal total energy.

4. Lateral migration effect: the CGIB impact deposits energy at high-density on the surface, and numerous surface atoms are displaced. Crater-like damage is formed by cluster ion. Under atomic bombardment, the sputtered atoms are ejected with a cosine distribution. On the other hand, GCIB bombardment induces lateral sputtering, therefore reducing the surface grain and having a smoothing effect on rough surfaces.

Because of their unique irradiation effects, GCIB processes can produce unusual surface modification effects. Figure 1.3 shows GCIB applications for nanoprocessing. High quality vanadium oxide films were obtained with the O_2-GCIB-assisted deposition technique [8)] and fast and high-selectivity etching of Si was performed with SF_6-GCIB [9)] thanks to the high chemical reactivity of the beam. Because of the lateral migration effects, smoothing of a rough diamond surface by Ar cluster ion beam was also possible regardless of the target hardness [10)]. Formation of an ultra-shallow junction was achieved by using B implantation through $B_{10}H_{14}$ GCIB [11)].

In simulation and experiment, it was reported that incident cluster size and energy are the important factors for large cluster irradiation effects. The physics between the GCIB and the solid surface needs to be understood in order to study the optimum gas cluster conditions for each processing. The size of gas cluster can be controlled by adjusting the supply gas and ionization conditions. For example, the mean cluster size increases with increasing supply gas pressure (P_s) and decreasing ionization electron voltage (V_e).

The size distributions of Ar cluster ion beam for different P_s and V_e conditions are shown in Figure 1.4. The mean size of these cluster ions was 2000 and 7000 atoms, respectively. However, these beams contain various

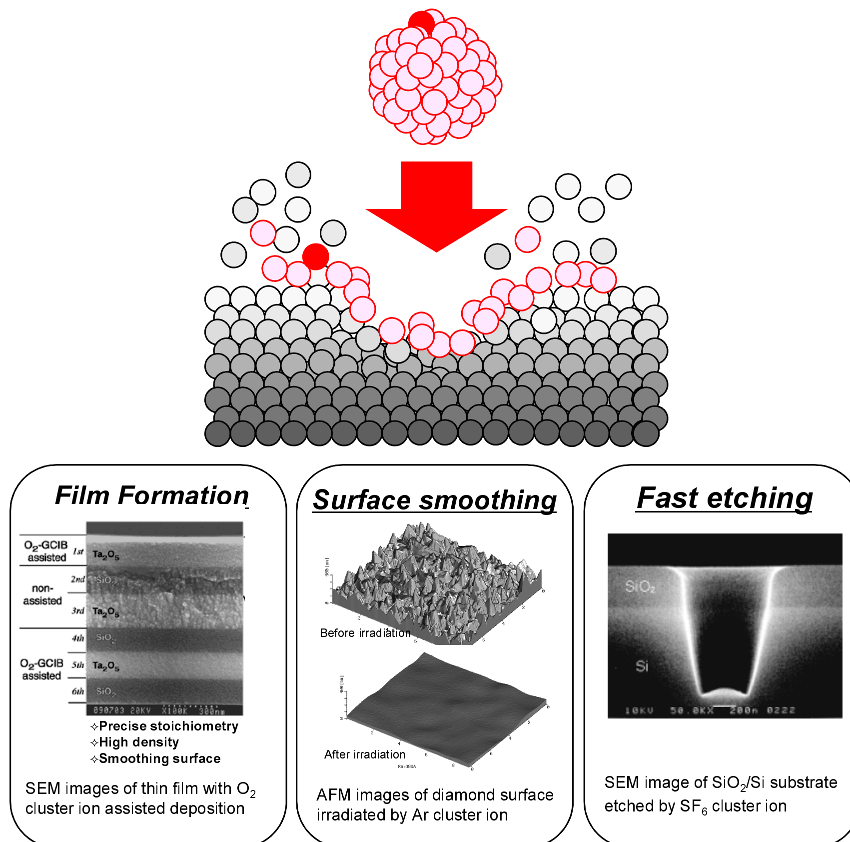

Figure 1.3: GCIB applications for nano-processing

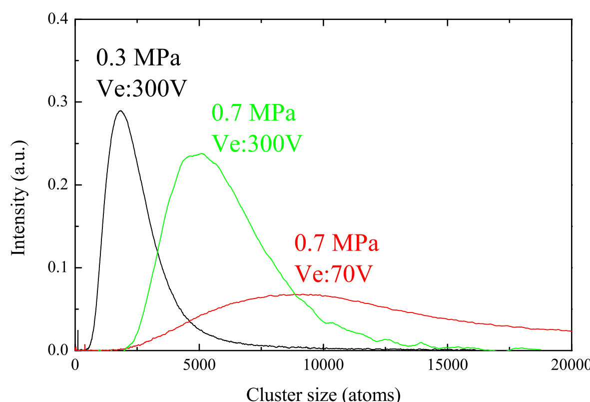

Figure 1.4: Size distribution of Ar cluster ion beam

sizes of clusters, and it is impossible to form a gas cluster of specific size without further manipulation. Therefore, only a few reports exist on the optimum size and energy for GCIB processing.

In this study, we investigated the effect of cluster size and energy on various interactions between gas cluster and solid surface by using size separate GCIBs for inorganic and organic targets.

1.4 Purpose of this study

This thesis work aims to understand the surface physics of the interaction between an energetic large GCIB and the target surface, and evaluate the optimum GCIB condition for various irradiation effects.

In chapter 2, the size-selected GCIB irradiation system will be introduced. The sputtering yield of Si and PMMA by using size selected gas cluster ion beam will be investigated. We will discuss the non-linear effect of sputtering and the mechanism of energy deposition with GCIB bombardment in this chapter.

Chapter 3 will present the secondary ion mass spectrometry system with size selected GCIB. In this chapter, we will discuss the secondary ion emission of Si and of various organic materials such as amino acids and

polymers. The secondary ion yield and intensity ratio of large secondary ion will be investigated.

In chapter 4, the surface damage with GCIB bombardment will be investigated. In the search for the optimum cluster conditions for low damage processing, the surface damage depth of a Si target and surface damage accumulation of various organic materials will be discussed.

In chapter 5, we will discuss changes in the surface morphology of Si and PMMA by GCIB bombardment. Surface smoothing is one of the important irradiation effects of GCIB. The incident cluster condition effect on surface roughnesswill be investigated in this chapter.

Finally, we will summarize the effect of incident cluster size and energy per atom on surface irradiation effects, and the optimum conditions for cluster irradiation in chapter 6.

Chapter 2

Sputtering yield with GCIB

2.1 Sputtering effects of ion beam bombardment

When a solid is bombarded by energetic ions, some atoms are ejected from the surface and this process is known as "sputtering". Typical energetic ions with energy in the keV range penetrate the solid surface and their energy is transferred to the solid atoms. In the case of Si, the calculated projection range for 0 degree incidence of 10 keV Ar atomic ions is about 15 nm as calculated with TRIM, indicating that the transferred energy is larger than 600 eV per nm [12)]. The atoms placed in the primary ion trajectory in the solid collide elastically and recoil because their binding energies are only in the order of a few eV. The recoiled atom continues to move and causes next collisions with near atoms, and a cascade of atomic collisions occurs near the solid surface. The sputtering phenomena take place when the recoiled atoms produced at or near the surface have enough energy to eject from the surface in an appropriate direction to escape the target.

Sputtering is one of the most important effects of ion beam irradiation, and a large number of experimental and simulation results on sputtering by energetic ions bombardment has been accumulated. The sputtering effect with ion bombardment was first documented by J. J. Thomson in 1907, and the physical process of sputtering was established by P. Sigmund *etal.* in 1969 [13)]. The energy transfer occurs in nuclear and electron interactions between a primary ion and solid atoms. The energy is mainly transferred via nuclear interactions in the energy range of below a few keV and by electron interactions in the energy range larger than 1 MeV.

Under atomic ion bombardment in the keV energy range, the sputtering yield is proportional to the nuclear stopping power of the target for the energetic ions because the numbers of disordered atoms increase with increasing transferred energy. Figure 2.1 (a) presents the model of target atom displacement with atomic bombardment, under which target atoms are energized and displaced by binary collision with incident ions, and the sputtering yield with atomic ion bombardment can be calculated by the linear collision cascade theory (Y_{lin})as follows.

$$Y_{lin}(E) \propto \frac{F(E)}{U_0} \tag{2.1}$$

where, E, F and U_0 represent the incident energy, the deposited and surface binding potential, respectively.

This theory insists on the sputtering yield being proportional to the stopping power and inversely proportional to the surface binding energy. The linear collision cascade theory has been the most successful in describing sputtering by keV atomic ion bombardment [14].

With Ar bombardment onto Si, sputtering occurs at an energy higher than 40 eV. The sputtering yield of Si increases with increasing incident Ar energy, and reaches the maximum value of about 2 atoms/ion at 10-50 keV Ar irradiation.

When solids are bombarded with cluster ions, collision cascades are induced by each constituent atom of the cluster and they overlap. The density of recoil atoms and the density of energy deposited on the solid surface by cluster ions is much higher than with atomic ions, and multiple collisions take place between incident ions and target atoms. It was found that the irradiation effects of cluster ions exceed the sum of the individual irradiation effects of constituent atom because of the multiple-collision processes on the surface. For example, it was found that the sputtering yield induced by a dimer hitting a surface was more than double that induced by an atomic projectile at the same velocity. This enhancement of sputtering yield is generally called “nonlinear effects” or “cluster effects”, and has been observed experimentally since the 1970’s. Andersen and Bay first reported [2] that the Ag sputtering yield by a Te dimer was about four

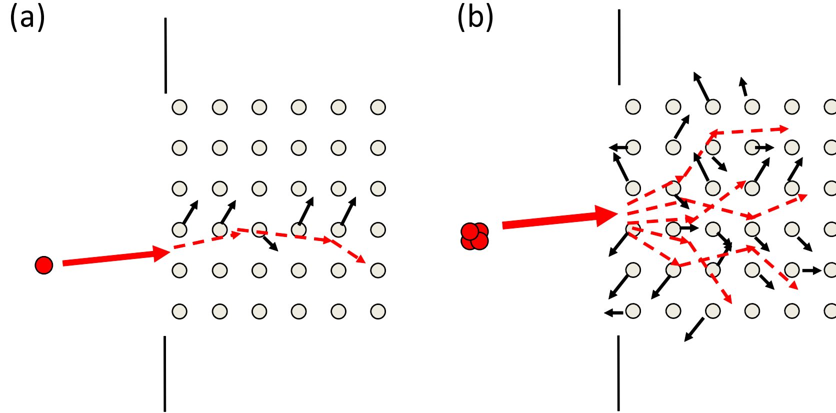

Figure 2.1: Irradiation effect with (a)atomic and (b)cluster bombardment

times higher than that by a Te atom at the same velocity (200 keV/atom). Bouneau *etal*. reported in 2002 that the nonlinear effect of Au sputtering yield increased with increasing incident cluster size under small Au cluster ($\leq$ 13 atoms/ion) ion bombardment [15)]. The enhancement factor of $Au_{13}{}^{+}$ would be 20 to sputter an Au surface at the same velocity, indicating that the Au sputtering yield by $Au_{13}{}^{+}$ was about 260 times higher than by Au^{+}.

Figure 2.1 (b) represents the model of target atom displacement with cluster bombardment. The sputtering yield is not in good agreement with the linear collision cascade theory under cluster ion bombardment. As long as the collision density is sufficient small, the energy deposition is can be described by the linear Boltzmann transport equation because a single binary collision occurred between the primary ion and the target atom. The target atom has to be stable in the linear Boltzmann transport theory when the collision occurs, however target atoms are no longer stable under high density energy deposition with cluster ion bombardment. The cascade evolves resulting in the formation of a highly disrupted, very hot region inside the solid. This region where this takes place is called a thermal spike.

A model of the sputtering yield with thermal spike, Y_{th}, was described by Sigmund and Claussen in 1981 [16)] as:

$$Y_{th}(E) \propto \frac{F(E)^2}{U_0^2} \tag{2.2}$$

Y_{lin} is proportional to the deposited energy, whereas Y_{th} varies proportional to the square of deposited energy.

Monte-Carlo (MC) simulations are used to calculate the collision process of atomic ions in a solid. The MC simulation method which is based on the binary collision theory made it possible to examine the evolution of collision cascades, formation of damage and sputtering with atomic ion bombardment. However, this method is not suitable for analyzing the cluster impact process because of the multiple collisions between incident ion and surface atoms.

Instead of the MC simulation method, the method of molecular dynamics (MD) simulation has been developed for describing cluster-solid interactions since the 1990's. In MD simulation, the motion of all atoms involved in the collision process is described, and the Newton's equation of motion is solved numerically for all atoms in the system within steps of the order of femtoseconds to picoseconds, which permit in-situ-, real time-like observation.

The concept of the MD method is very simple, but it requires quite larger memory resources and longer computational times than the MC method based on binary collision theory. Because of improvements in computers and low-cost availability, theoretical research through MD simulation is now the normal approach for understanding the complexity of the interactions in a collision which is more difficult to be solved analytically. Nonlinear effects between cluster ion and target were first calculated by MD simulations by Shapiro *etal.* in 1989 [17)] and Shugla *etal.* in 1990 [18)].

Figure 2.2 presents snapshots of atomic and cluster carbon impacting on a diamond surface in MD simulation [19)]. Each carbon atom was energized to an energy of 2 keV/atom, so that the total incident energy of C_{60} was 120 keV. To compare the result of C_{60}, Fig. 2.2 (a) presents a sum of 60 atomic bombardments. The yellow dots represent incident atoms and the green dots represent the displaced atoms with atomic or cluster bombardment. This MD simulation indicates that the number of displaced atoms

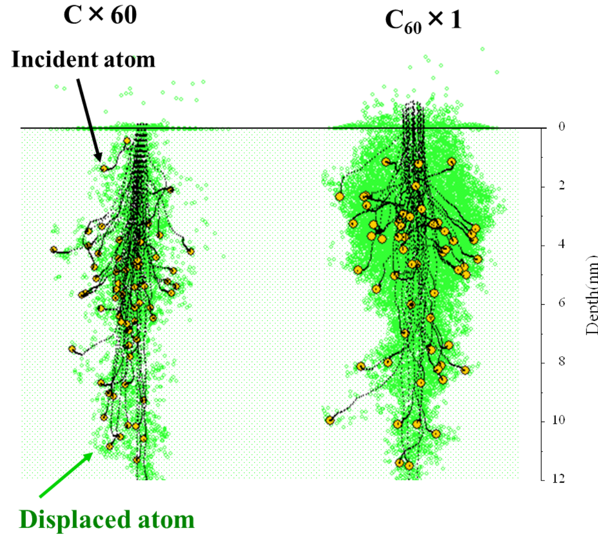

Figure 2.2: MD simulation of atomic bombardment and cluster bombardment into diamond with 2 keV/atom incident energy [19)]

was much higher with cluster than the sum of individual atomic impacts, and the penetration depth of C_{60} was as deep as C at the same velocity, indicating that the number of displaced atoms would increase non-linearly with increasing incident cluster size and it agrees with the experimental results.

Understanding the physics of energetic cluster bombardment near the surface is very important, and the sputtering phenomenon is strongly related to the energy deposition process. Under small ($\leq$ 10 atoms/ion) cluster ion bombardment, these nonlinear effects were reported to be experimentally a function of cluster size [15, 20, 21)]. In contrast, there were only a few reports investigating the nonlinear effects under large ($\gg$ 100atoms/cluster) cluster ion bombardment.

In this chapter, we investigate the sputtering yield and cluster effects for sputtering under bombardment with large gas cluster ions.

2.2 Size select GCIB irradiation

As mentioned in section 2-1, it was believed that large clusters would be more efficient in inducing the nonlinear effect. Gas clusters consist of more than several hundreds of atoms and are much larger than typical metal or carbon clusters. However, the nonlinear effects of the large gas clusters could not be measured precisely because of a number of reasons.

1. A typical gas cluster ion is too slow to be compared with atomic ions. Each constituent atom of typical gas cluster has energy of a few 10eV, which is below the threshold energy for sputtering with atomic ion bombardment, but nonetheless high sputtering yields are obtained with GCIB. To compare the irradiation effect of GCIB with that of an atomic ion at the same energy-per-atom, high energy and small gas cluster ions are required.

2. GCIB has a very broad size distribution and therefore it is very difficult to investigate the irradiation effects of a cluster of specific size. The mean gas cluster size can be roughly controlled by inlet gas pressure and ionization condition However, without size selection, the GCIB size distribution can extend from about a few to several thousand atoms.

It was reported that the sputtering yields with GCIB strongly depends on the mean cluster size in MD simulation. For instance, Figure 2.3 shows the snapshots of Si(100) surface after 20 keV Ar_{2000} and Ar_{10000} impacting in MD simulation [22]. Black dots represent displaced Si atoms. When the incident size is 2000, the Ar cluster penetrates the Si surface and Si atoms are displaced spherically. As a result of 20 keV Ar cluster bombardment, a crater-like damage remains on the surface. On the other hand, under Ar_{10000} bombardment the cluster does not penetrate the surface but breaks up on the surface and displacement of surface atoms does not occur, indicating the irradiation effect such as sputtering and implantation with 20keV Ar_{10000} is far from that with 20 keV Ar_{2000}, although the total incident energy is the same. However, the cluster ion beam without size selection

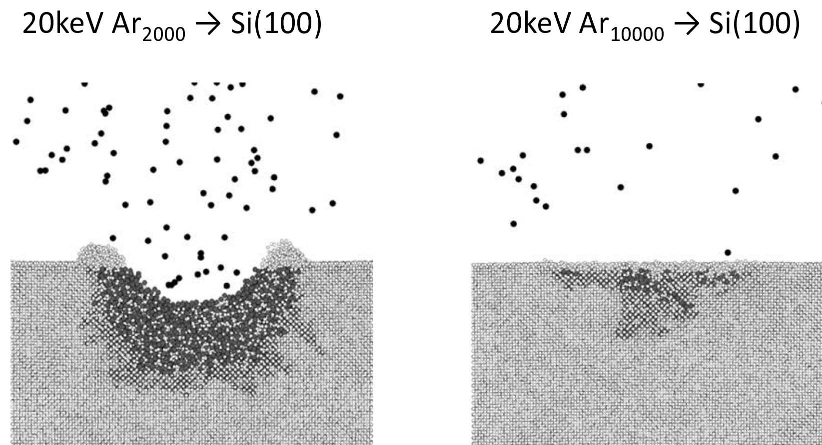

Figure 2.3: MD simulation of Si sputtering with 20 keV Ar_{2000} and Ar_{10000} [22]

contains clusters of various sizes, and therefore the irradiation effects of the unselected cluster would be a mixture of effects of various sizes.

To investigate the irradiation effects of a cluster of specific size, the incident cluster has to be selected in some way. There are various methods for cluster size separation, but it has been difficult to obtain both high ion current and high size resolution after size selection. The application of a E×B filter for size separation has been reported [23], but the size resolution by this technique was not satisfactory.

The irradiation effect with size-selected gas cluster beams by using a strong magnet has been also studied. However, the magnetic field intensity needed to bend same-energy ions is proportional to the square root of the incident ion size, and therefore it is difficult to select the large ions by using magnetic fields.

Toyoda *etal*. reported that both strong magnetic field (1.2 T) and long effective field length (450 mm) are necessary to realize separation of the large gas cluster ion beam in high size resolution [24, 25]. The cluster size was selected in this study with the time-of-flight (TOF) method, because it can accurately select the wished incident cluster size irrespective of its number of constituents.

Figure 2.4: Photograph of GCIB irradiation equipment

A photograph of the GCIB irradiation apparatus is shown in Fig. 2.4 and a schematic view of this equipment is shown in Fig. 2.5. The apparatus consists of source, ionization and target chambers. Each chamber was put under vacuum by a turbo molecular pump and the base pressure was about 1×10^{-5} Pa. Adiabatic expansion of a high pressure gas through a nozzle is used to form Ar gas clusters, whicn are introduced into the second source camber via the skimmer.

The throat of the nozzle and the orifice of the skimmers in this equipment were of 0.1 and 1 mm in diameter respectively. The inlet pressure of Ar gas was 0.4-1.0 MPa and gas flow rate was about 400-700 sccm.

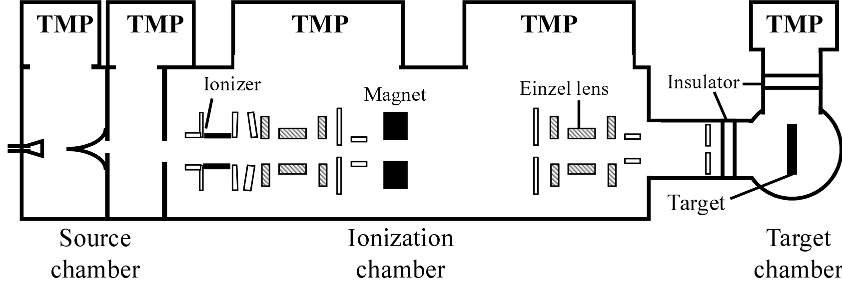

Figure 2.5: The experimental setup for size-selected GCIB irradiation

The working pressure of first and second source chamber was about 1 and 10^{-3}Pa, respectively.

The source and ionization chambers were separated by an aperture of 3mm diameter in order to keep the ionization chamber in high vacuum. The neutral clusters were ionized by electrons with energy in the range of 70-300 eV emitted from a hot tungsten filament. The mean cluster size of the GCIB was roughly controlled by the inlet source gas pressure, ionization voltage and emission current.

A photograph of the ionizer is shown in Fig. 2.6. The ionizer consists of filaments, anode, extraction electrode, einzel lens and first deflector. The ionized clusters were accelerated in the energy range of 5-60 keV and transported to the target chamber. Atomic and small cluster ions were removed by magnets (0.3 T) when the unselected GCIB was directed towards the target.

The primary ion beam size selection was performed by the TOF method using two pairs of ion deflectors installed along the beam line. A schematic diagram of cluster size selection with the TOF method is shown in Fig. 2.7. First, the Ar cluster ion beam was chopped to a width of 5-20 μs by applying a high-voltage pulse at the first deflector. The pulsed ion beam after the first deflector has the same energy and contains various sizes of cluster ions because of the wide size distribution. Therefore small cluster ions would reach the second deflector before larger ones. At the second deflector the pulsed ion beam was chopped again to the same width as the

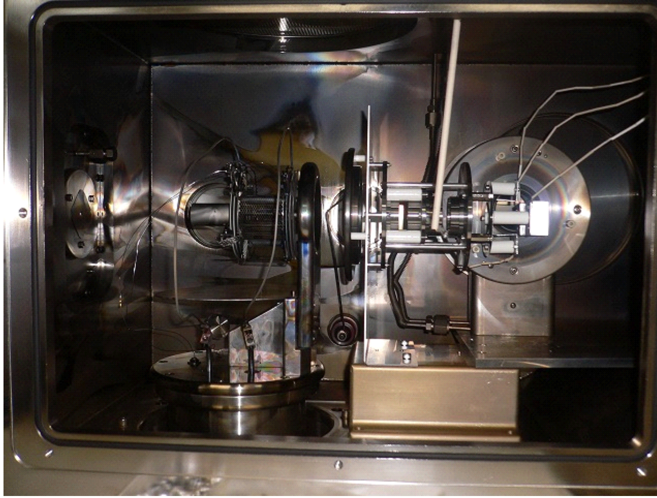

Figure 2.6: Photograph of the ionizer

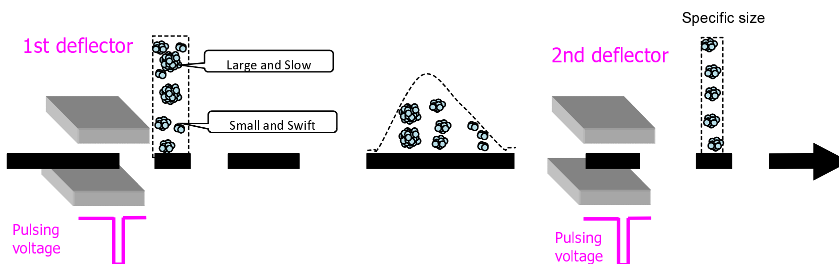

Figure 2.7: Schematic diagram of cluster size selection with the TOF method

first pulse after an appropriate time delay from the first pulse. The pulsed ion beam at the second deflector contained a specific size of cluster ions depending on the delay time (t_D) between the two pulses. The flight length between the first and second deflectors was of 1000 mm.

The selected Ar cluster size N is proportional to V_a and t_D^2, where V_a is the acceleration voltage. For instance, the flight time of 20 keV Ar_{1000} from first to second deflector is of 102 μs, and that of 20 keV Ar_{4000} is of 204 μs.

Figure 2.7 shows the cluster size distributions of the unselected and size-selected Ar cluster ion beam. The full width at half maximum (FWHM) of

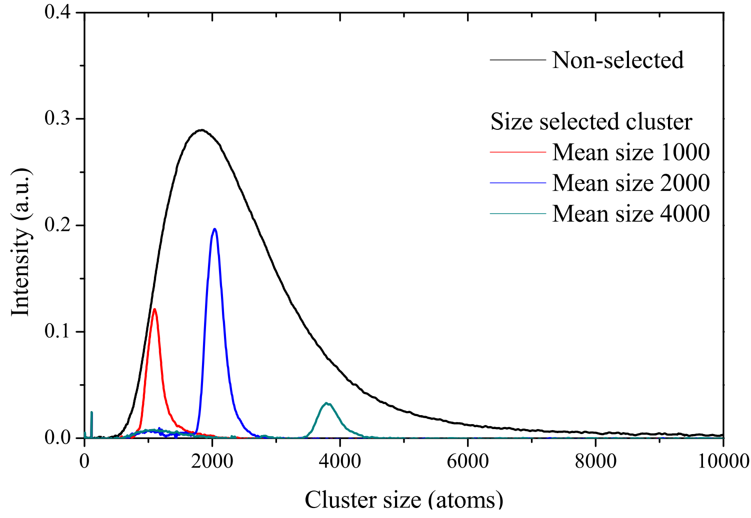

Figure 2.8: Cluster size distributions of the unselected and size-selected Ar cluster ions

the size distribution of the cluster ion beam without size selection was about 2000 atoms, and that of the size-selected cluster ion beams was about a few hundred atoms, about 10% of the original distribution. The size resolution ($M/\Delta M$) of the size-selected cluster ion beam can be controlled by t_D and the pulse width of first and second deflectors. The electrostatic einzel lens installed in front of the second deflector was used for focusing the ion beam to a 1 mm spot on the target.

The primary ion beam was incident on the target at an angle of 0 degree with respect to the surface normal. The ion beam current was measured in the target chamber. The target chamber was separated from ionization chamber by an insulator and served as a Faraday cup during irradiation. The working pressure in the ionization and target chamber was 1×10^{-4}Pa. The repetition frequency was 5000 Hz and the current intensity was from 0.5 to 5 nA after size selection. The current density of the unselected cluster ion beam was higher than 100 μA/cm^2. The maximum current density of the size-selected cluster ion beam was about 500 nA/cm^2 for

Ar_{1000} irradiation, and the current density was maintained at about 50 nA/cm^2 for Ar_{16000} irradiation. The sputtering yields of Si as the inorganic target and polymethylmethacrylate (PMMA) as the organic target were investigated under impact of the Argon GCIB at various conditions.

2.3 Results-Si target

The cluster ion beam was not scanned during irradiation of the Si sample, in order to save irradiation time.

The crystal orientation of the Si substrate was (100). The etched volume was measured ex situ by an interferometric surface profiler (Maxim-NT, Zygo, USA) and a contact surface profiler (Dektak3, Veeco, New York, USA). The observation area was 2.6 mm $\times$ 2.4 mm and the spatial resolution was 10 μm (x, y axes) and 0.1 nm (z axis) respectively.

Figure 2.9 shows a typical example of a surface profile image for the Si surface irradiated with 20 keV unselected Ar cluster ions with a mean size of 2000 atoms/cluster at an irradiation dose of 3×10^{13} ions. The sputtered volume was calculated directly from the surface profile because of the high depth resolution. The sputtered depth of the Si sample irradiated with unselected GCIB with scanning was measured with an interferometric surface profiler and with contact surface profiler measurement and the results of the two measurements were in good agreement.

Figure 2.10 shows the variation in sputtered volume of Si with an irradiation dose of a 20 keV Ar GCIB. The sputtered volume was proportional to the irradiation dose, indicating that the sputtering yield can be evaluated by the surface profiles and Ar cluster ion dose, even if the irradiation dose was as small as 1×10^{13} ions. From this proportionality constant, the Si sputtering yield with 20 keV Ar cluster was estimated to be about 35atoms/ion.

In irradiation experiments for size-selected Ar cluster ions, the dose used was higher than 5×10^{13} ions. The effects of incident cluster size on Si sputtering yield for 20, 40 and 60 keV Ar cluster ions are shown in Fig. 2.11.

Under bombardment with 40 keV Ar_{1000}, more than 200 Si atoms were sputtered, and this sputtering yield was more than 100 times higher than that with 40 keV Ar atomic ions. The sputtering yields decreased with increasing cluster size because of the lower incident energy of each constituent atom. The sputtering yield of 40 keV Ar_{4000} was still higher than about 70 atoms/ion, and 40 keV Ar_{16000} was about 40 atoms/ion, i.e. 20 times

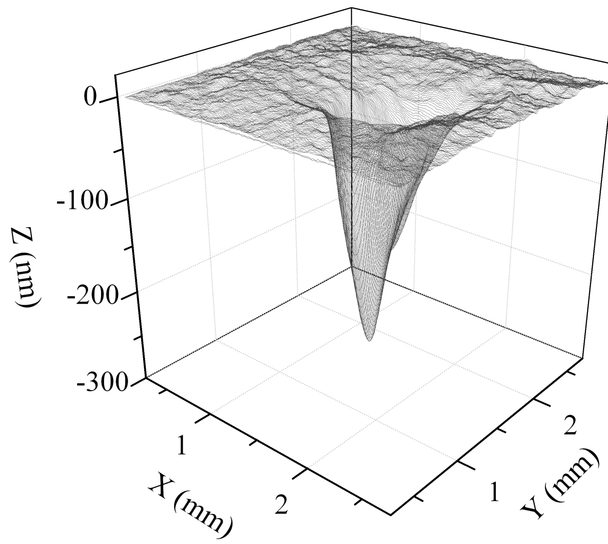

Figure 2.9: The surface profile of Si measured with an interferometric surface profiler after irradiation with 20 keV unselected Ar GCIB with mean size of 2000 atoms/cluster at the fluence of 3×10^{13} ions

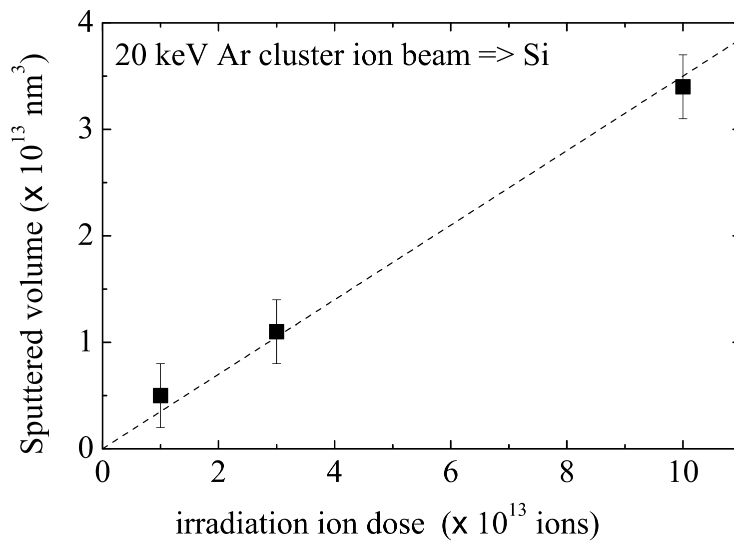

Figure 2.10: Variation of sputtered volume of Si with irradiation dose for 20 keV Ar cluster ions

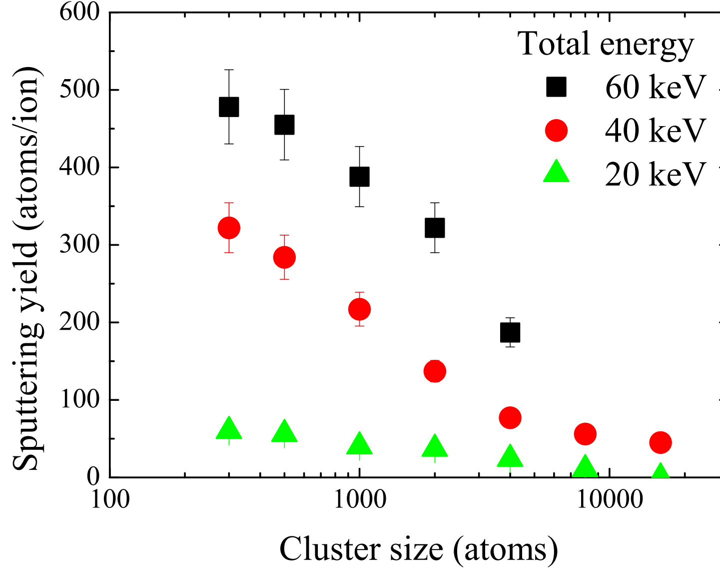

Figure 2.11: Si sputtering yield with varying incident cluster size for 20, 40 and 60 keV Ar cluster ions

higher than with 40 keV Ar atomic ions. The energy of each constituent atom for 40 keV Ar_{16000} was about 2.5 eV, which is lower than the surface binding energy of Si (about 4.6 eV [26]), and this is assumed to result from the multiple collisions between the cluster ion constituents and surface atoms.

Figure 2.12 shows the sputtering yields of Si with Ar cluster ions. The solid squares present the sputtering yields for 20-60 keV unselected Ar cluster ions and the mean size of incident cluster ions was 2000 atoms/cluster. The sputtering yields of Si with Ar clusters increased non-linearly with acceleration voltage. These sputtering yields (Y) for cluster ion beams containing various sizes of clusters can be represented as:

$$Y = \frac{\int Y(n)I(n)dn}{\int I(n)dn} \tag{2.3}$$

where n is the number of constituent atoms, $I(n)$ is the beam intensity of the n-size cluster ions and $Y(n)$ is the sputtering yield for the n-size cluster

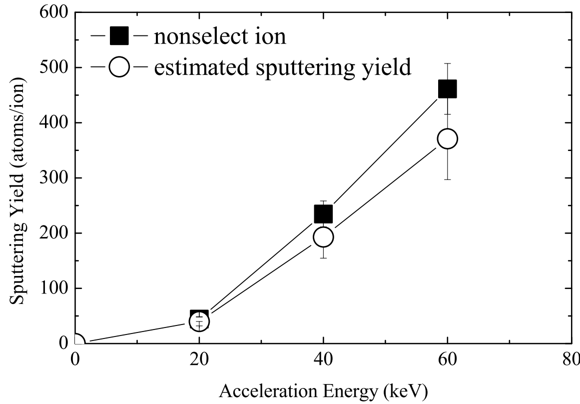

Figure 2.12: The sputtering yields of Si with 20-60 keV Ar cluster ion

ion. Open circles in the figure present the calculated sputtering yields from this equation. As clearly shown in Fig. 2.12, the calculated yields agreed well with the yields for unselected Ar cluster ions, and this indicates that the irradiation effects under the incidence of clusters of varying size can be reproduced by the sputtering yield integral for each size of cluster ions. It also shows that the cluster size selection with the TOF method is useful for investigating irradiation effects with large cluster ions.

Figure 2.13 shows the variation in sputtering yield for various sizes of Ar cluster ion and energy per atom. The dotted and solid lines represent the experimental data and the approximated curve. There was a threshold incident energy-per-atom to cause sputtering of the target, and the threshold energy depends precisely on the incident cluster size. For example, the threshold energy for sputtering was about 5 eV/atom under Ar_{1000} bombardment, and 1 eV/atom under Ar_{16000} bombardment. It would be natural that the threshold energy is dependent on incident cluster size, because the threshold energy for sputtering with Ar atomic ion is about 25eV.

The effect of incident cluster size on Si sputtering and displacing threshold energy shows in Figure 2.14. The solid circles represent experimental results and open triangles represent the threshold energy for Si displacement energy in MD simulation [27]. Each of the threshold energies decreased

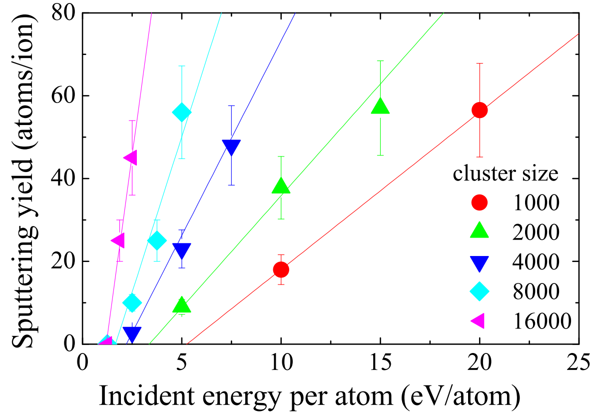

Figure 2.13: Si sputtering yield with cluster ion bombardment at low energy per atom

with increasing incident cluster size in a similar way. The dotted line represents the simple power law equations where power index was 1/3, and they are in good agreement with experimental and simulation results. This power index can be quantified as the volume of damage region. If the aspect ratio of the damage region does not change as a function of cluster size, it can concluded that the deposited energy density is proportional to the cube root of the incident cluster size.

Figure 2.15 shows the sputtering yield of various sizes of Ar cluster as a function of the incident energy. The sputtering yield and incident enregy was normarized to the dimension of damage region ($N^{2/3}$) and the energy density ($N^{-1/3}$), respectively. The red-dotted line represents the incident energy dependence of F^2 where F is the deposited energy. As can be seen in the figure, the incident energy-per-atom effect on Si sputtering yield is in good agreement with the square of the deposited energy.

As will be mentioned in the following section, the sputtering yield by linear collision cascade model is proportional to the deposition energy, and that by thermal spike model is proportional to the square of the deposition energy. This result indicates that GCIB irradiation induces thermal spike

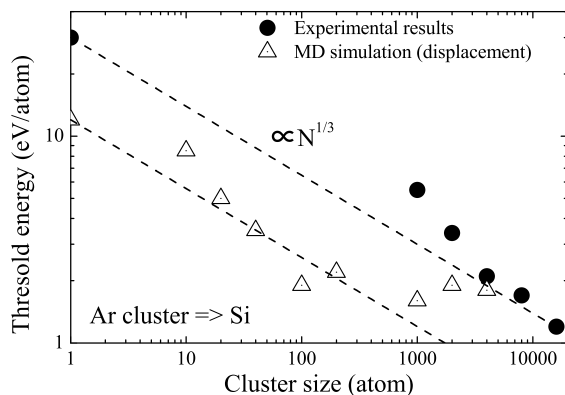

Figure 2.14: Si sputtering threshold energy with varying cluster size

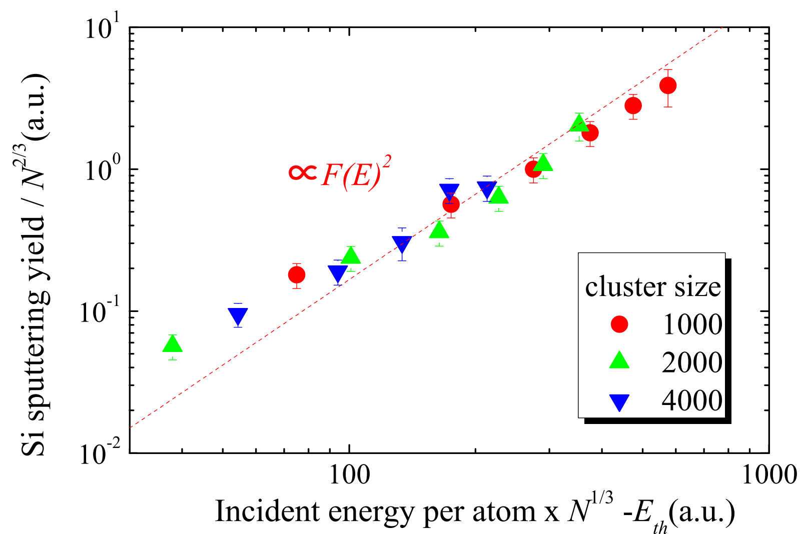

Figure 2.15: Si sputtering yield with varying incident energy cluster ions

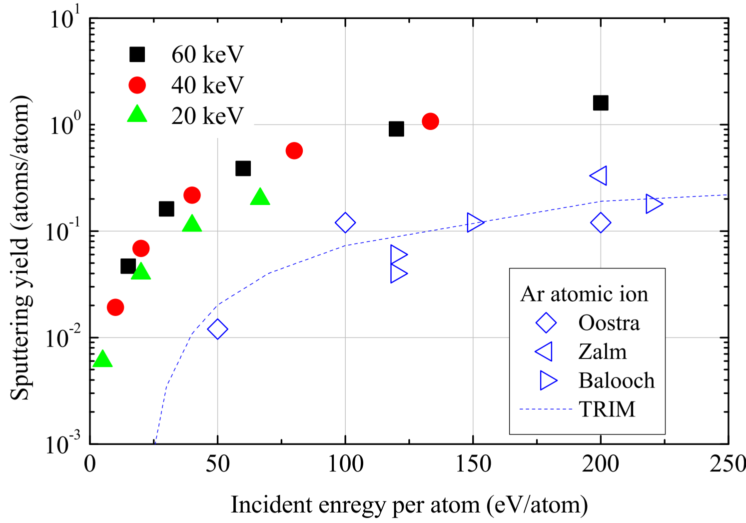

Figure 2.16: The nonlinear effects of Si sputtering with Ar GCIB irradiation

on the surface.

Figure 2.16 shows the sputtering yields of Si per incident atom with Ar cluster and atomic ions as a function of incident energy per atom. The yields per atom with Ar cluster ion beams were calculated by the total yield divided by cluster size. Blue dots represent the experimental results of Ar atomic ion reported by Oostra *etal.* in 1987 [28)], Zalm in 1983 [29)] and Balooch *etal.* in 1996 [30)], and the blue-dotted line represents the sputtering yield calculated in this work with TRIM. In both cluster ion and atomic ion bombardment, the sputtering yield increased rapidly with increasing incident energy per atom near the sputtering threshold energy, and saturated under a few hundreds eV/atom. The Si sputtering yield is about 0.2 atoms with 200 eV Ar atomic ion bombardment and about 1.8 atoms with 200 eV/atom Ar cluster ion bombardment (60 keV Ar_{300}). This result suggests that the sputtering enhancement with Ar_{300} would be 9.

Figure 2.17 shows the Si sputtering enhancement factor with B_{18} and C_{60} as reported by Tanjo and Hill *etal.* [31)],respectively. As shown, the enhancement factor with B_{18} was 11 and with C_{60} was 10. This result sug-

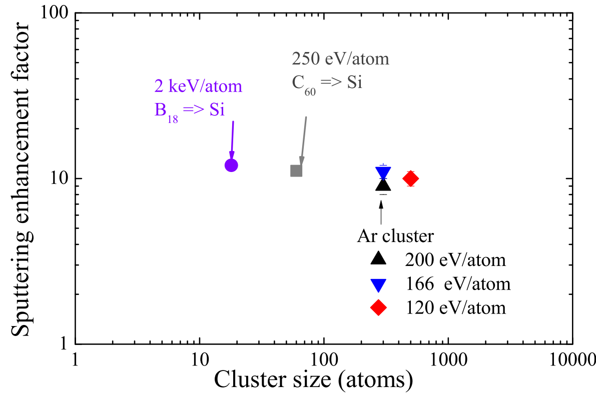

Figure 2.17: The nonlinear effects of sputtering with varying cluster ion bombardment

gests that the enhancement factor with cluster ion would increase rapidly with increasing cluster size under small cluster (N$\leq$ 20) bombardment, and saturate at around 10.

In MD simulation, the correlation between the number of displaced atoms and size has also been reported for carbon cluster bombardment [32]. The number of displacements caused by atomic impact shows first an increase and then a decrease towards the end because some of the displaced atoms are recovered into the lattice. On the other hand, the number of displacements caused by cluster impact only increases because of the high-density energy deposition. When an energetic ion bombards to the surface, the incident atom energizes to the surface atoms. Under atomic ion bombardment, some of atoms are displaced permanently and trigger damage, but most of them are only excited. Under small cluster ion bombardment, the cluster is broken and the constituents are scattered on the local area. Then, excited areas start to overlap and some of the excited atoms are finally displaced and trigger damage. Therefore, the number of displaced atoms increases nonlinearly under cluster ion bombardment. These nonlinear effects increase with increasing incident cluster size because all of the excited areas becomes damaged areas.

The nonlinear effects with large cluster are saturated because the entire irradiated area would be no longer excited, and the number of displaced atoms is proportional only to the incident energy. For Si, the ratio between damaged and excited atoms with atomic ion bombardment is 9:1.

Figure 2.18 represents the experimental results and calculation curve of Si sputtering yield with Ar cluster ion bombardment. The sputtering yield can be expressed as the product of the sputtering yield with atomic ion and enhancement factor($E/N \geq 25$eV) or the square of the depositted energy ($E/N \leq 25$eV). Therefore, the calculated sputtering yield can represented as follows.

$$Y_c(E,N) = k(N) \times Y(E/N + E_{th.a} - E_{th.c}) = 9 \times N \times Y(E/N + E_{th.a} - E_{th.c}), \tag{2.4}$$

for the high energy cluster ions ($E/N \geq 25$eV), and

$$Y_c(E,N) = \alpha \times N^{2/3} \times (E/N \times N^{1/3} - E_{th.a})^2, \tag{2.5}$$

for the low energy cluster ions ($E/N \leq 25$eV). E, N, k and E_{th} represents the total energy, the cluster size, the enhancement factor and the sputtering threshold energy, respectively.

The enhancement factor of gas cluster ion would be of a constant value, 9. The dotted lines describe this calculation results, and these curves are in good agreement with the experimental results.

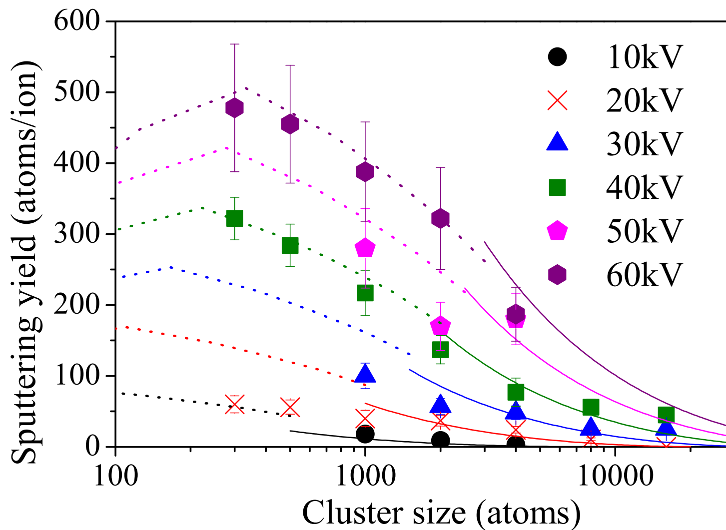

Figure 2.18: Model of Si sputtering yield with Ar cluster ion

2.4 Results-PMMA target

For organic materials, it has also been reported that the sputtering yields are enhanced by one order of magnitude by using GCIB. Moreover, gas cluster ion bombardment onto organic materials has attracted interest not only because of the high sputtering yield, but also because of the constant sputtering rate.

Atomic ion bombardment causes chain scission, cross-linking and carbonization of polymeric surfaces because of the large energy transfer for organic materials [33, 34, 35]. In other words, under atomic ion bombardment irradiation damage accumulates on the underlying surface. Small cluster ion beams, such as SF_5^+ and C_{60}^+ can reduce the surface damage and the sputtering rates with small cluster ions are sufficiently high [36, 37]. However,these small cluster ions do not work well for constant etching on some polymeric materials, such as polycarbonate (PC) and polystyrene (PS) because of carbon deposition and damage accumulation [38, 39]. In contrast, with GCIB, constant etching rates with little or no damage to the un-

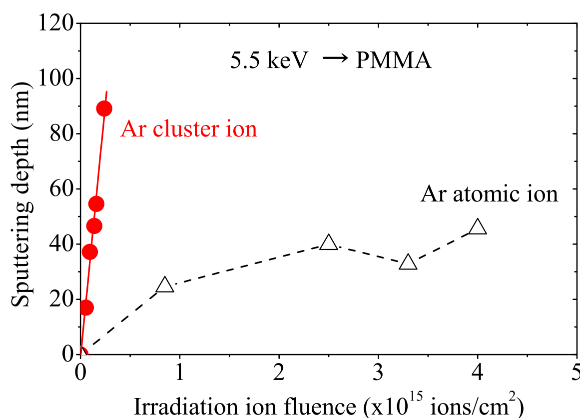

Figure 2.19: Variation in sputtered depth of PMMA with irradiation dose for 5.5 keV Ar cluster and atomic ions

derlying structure have been reported for various organic and polymeric materials such as leucine, arginine, PC, PS and PMMA [40, 41, 42].

Figure 2.19 shows the etching depth of PMMA with 5.5 keV Ar atomic ion and cluster ion beam [41]. The sputtering rate of PMMA with atomic Ar^+ incidence decreased with increasing fluence. It could be considered that the chemical transformation of PMMA to a carbon-rich material causes the decrease in sputtering rate with fluence. In contrast, the sputtering depth of PMMA with Ar cluster ion shows linear dependence on fluence and more than 10 times that with Ar atomic ion at low fluence. In view of this, GCIB is proposed as one of the solutions to the problem of sputtering of organic and polymeric materials at high speed without damage.

For irradiation of organic materials, the sample was mounted on a scanning stage and rastered for uniform etching. PMMA (repeat unit mass of 100 u, molecular weight (Mw) 700,000-750,000 u; Nacalai Tesque Inc. (Kyoto, Japan)) was dissolved in toluene as a 2-5 wt% solution. PMMA thin films were prepared by spin coating on a Si substrate (10 mm $\times$ 10 mm) with a thickness of about 100-300 nm. The irradiation ion fluence was 2 $\times$ 10^{13}-1 $\times$ 10^{14} ions/cm^2 and the etching area was 4 mm $\times$ 5 mm. The etching depth was measured ex situ with a contact surface profiler.

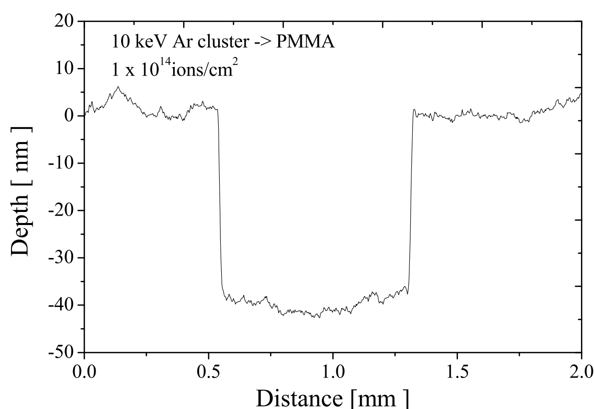

Figure 2.20: Surface profile image of PMMA irradiated with 10 keV Ar cluster ion

Figure 2.20 shows the surface profile image of the PMMA surface irradiated by 10 keV Ar cluster ion. The irradiation dose was 1×10^{14} ions/cm^2 and the estimated etching depth was about 40 nm. The sputtering yield of PMMA was calculated from the etched depth and ion fluence assuming a PMMA density of 1.2 g/cm^3, and was about 400 units/ion.

Figure 2.21 shows the effects of incident Ar cluster size on PMMA sputtering yield for 20 keV Ar (black dots) and C cluster ions (red square) [37]. The PMMA sputtering yield with Ar cluster was higher than with C cluster. The sputtering yields with size-selected Ar cluster ion beam decreased with increasing cluster size, and this decrease is attributed to the lower energy of each constituent atom. The sputtering yield with 20 keV Ar_{16000} was maintained relatively high, but the energy of each constituent atom for 20 keV Ar_{16000} was only 1.25 eV, which is lower than the value of the bond energy, for example C-C bonding (about 3.5 eV) in PMMA.

The threshold energy per atom for PMMA sputtering was estimated to be less than 1 eV/atom with 20 keV Ar cluster ion bombardment, and this could be attributed to the effect of multiple collisions between the cluster ion and surface atoms. The Si sputtering yield with Ar cluster increased monotonously with increasing incident energy-per-atom, but in

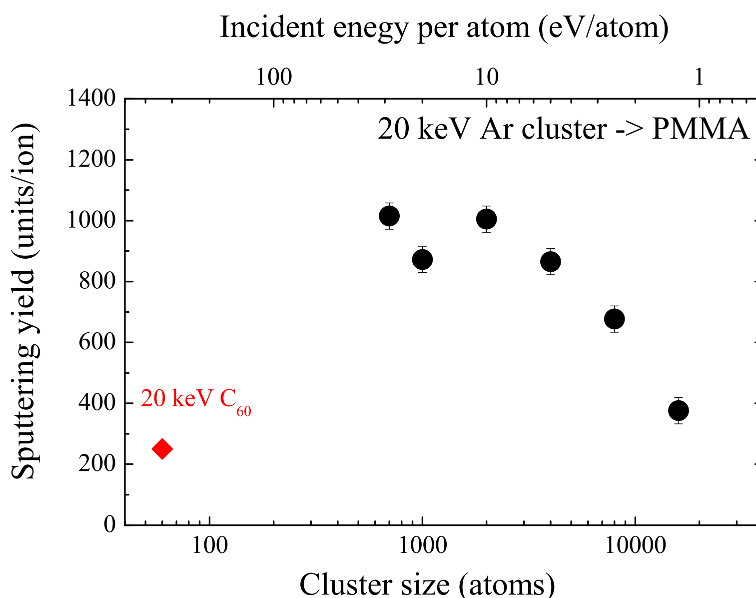

Figure 2.21: Variation in PMMA sputtering yield with incident Ar cluster size for 20 keV Ar cluster ions

contrast PMMA sputtering yield remained about the same under cluster ion bombardment in the range of Ar_{1000} to Ar_{4000}.

Figure 2.22 shows the effects of incident Ar cluster size on PMMA sputtering yield for 5-30 keV Ar cluster ions. As shown, PMMA sputtering yields increased with increasing incident energy per atom up to 10 eV/atom and saturated independent of the total energy. The saturated value with 20 keV Ar cluster was about 1000 units/ion, and the energy efficiency for sputtering with this condition was only 20 eV/unit, suggesting that more than 20 % of displaced PMMA units were ejected from the surface. This value is much higher than the sputtering probability of an inorganic target such as Si, which was less than 1 %, and therefore the sputtering yield with small cluster ion would be saturated in PMMA. This effect of incident energy on the sputtering yields of organic targets has been observed earlier in MD simulations [43, 44)], and is in good agreement with this experimental result.

Figure 2.23 shows PMMA sputtering yield with Ar_{1000} and Ar_{4000} as a

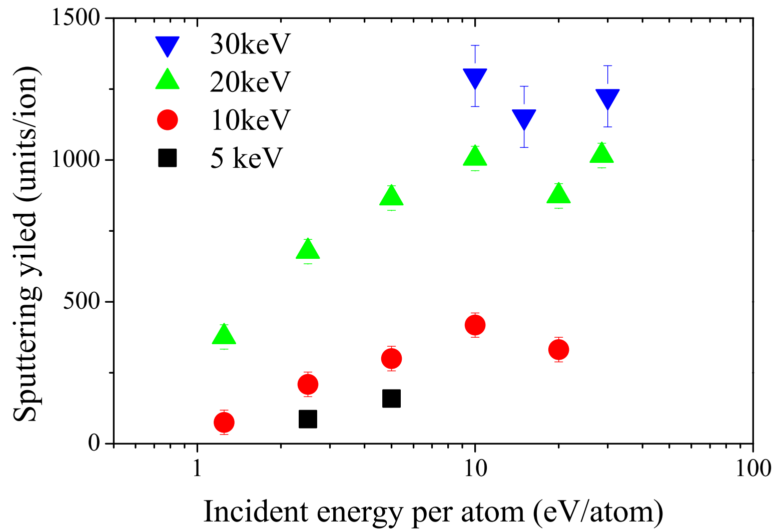

Figure 2.22: Variation in PMMA sputtering yield with varying incident Ar cluster energy-per-atom for 5-30 keV Ar cluster ions.

function of incident energy per atom. The threshold energy for sputtering with Ar_{1000} and Ar_{4000} was estimated from approximated curves to be about 2.5 and 1.5 eV, respectively, indicating that the threshold energy decreased with increasing incident cluster size, and this is similar to the results of Si sputtering. As shown, the sputtering yield increased linearly with the incident energy per atom, indicating that the incident energy was mostly used for sputtering PMMA, and the efficiency of sputtering was independent of the incident energy per atom.

It would be easy to control the etching rate by controlling the incident cluster size and energy per atom. In terms of fast etching with GCIB, fast and large clusters would be the optimum cluster condition.

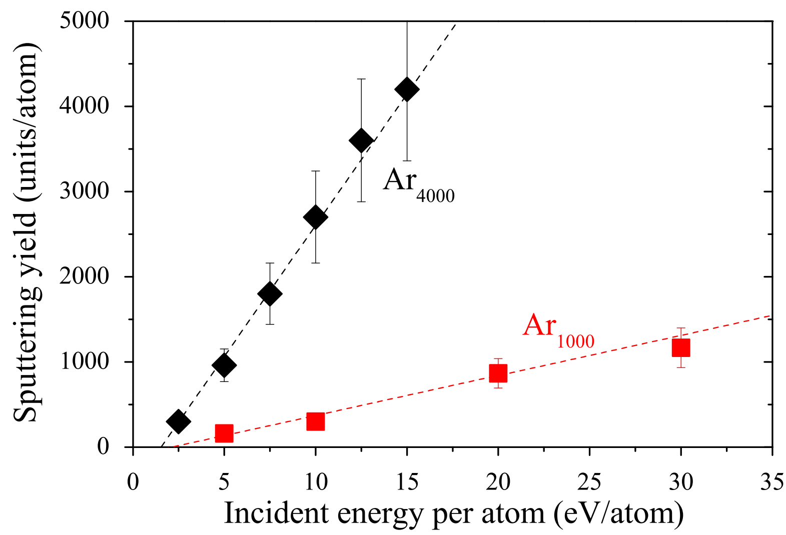

Figure 2.23: Variation in PMMA sputtering yield with varying energy per atom for Ar_{1000} and Ar_{4000} clusters.

Chapter 3

Secondary ion emission with GCIB

3.1 Secondary ion mass spectrometry

When energetic ions bombard a solid surface, some particles are emitted from the surface, as mentioned in chapter 2. The sputtered particles emitted from the surface are mostly neutral, with less than one percent being in a charge state called "secondary ions".

The existence of ionized particles when sputtering various surfaces was first documented by J.J. Thomson in 1910, but it took about 30 years to build an instrument capable of measuring the emitted ions. These emitted ions, called "secondary ions" are easy to detect using various means and can help understanding the surface structure. For this reason, the Secondary Ion Mass Spectrometry (SIMS) technique has been one of the most popular and useful surface analysis methods. SIMS has been also applied in the investigation of irradiation effects of GCIB because detected secondary ions reflect both the surface structure of the target and the irradiation effects of the incident cluster.

Under cluster ion bombardment, the "nonlinear effects" have been only observed not only for sputtering yield, but also for secondary ion yield. For instance, SIMS with cluster ions such as Au_3^+, C_{60}^+ has been frequently studied, and numerous experimental results have shown that secondary ion yields are significantly enhanced by cluster ion impact.

Thomas *etal*. reported in 1985 on the secondary ion yield of CsI with H cluster [45]; they found that the enhancement effect of cluster ion for secondary ion emission was similar or higher than that for sputtering.

Benguerba *etal*. reported on the secondary ion yield of gold and some other molecules with Au and CsI clusters in 1991 [46]; they found that the enhancement factor depends not only on cluster size but also on the target material. In their work, the enhancement of the secondary molecular ions yield was higher than that of the secondary atomic ions yield, suggesting that large secondary ions are more efficiently detected when using large cluster ions.

Unique irradiation effects have also been reported for secondary ion emission under large gas cluster ion bombardment. Figure 3.1 represents the secondary ion spectra of Si with obtained with Ar atomic ion and Ar cluster ion at an energy of 20 keV [47]. Under bombardment with Ar cluster ions, Si cluster ions such as Si_2^+ and Si_3^+ appeared with high intensity. On the other hand, their intensity is very low when using atomic Ar ions. Meanwhile, that triggers the emission of multiply charged ions such as Si^{2+} and Si^{3+}. There were however never observed using Ar cluster ion bombardment. This indicates that the secondary ion was ejected more softly by GCIB bombardment, the amount of energy transferred to the ejected particles being too low to allow for multiple charging. In this chapter we investigates the effect of the primary Ar cluster size and energy-per-atom on secondary ion emission, and discuss the energy deposition and emission processes of secondary ions under large cluster ion bombardment.

3.2 Size-selected cluster SIMS

3.2.1 Time-of-flight mass spectrometry

Mass spectrometric techniques provide information about the mass-to-charge ratio (m/z) of charged particles generated from a target sample. The mass-to-charge ratio can be measured with various methods, namely time-of-flight (TOF), magnetic sector, quadrupole mass spectrometer, and Fourier transform ion cyclotron resonance.

In this SIMS analysis, secondary ions were measured using a TOF mass spectrometer (MS) because of its simple instrumentation and ability to detect all ions at one time, even in the high-mass range (in principle, up to infinity). The principle of a TOF instrument is described below.

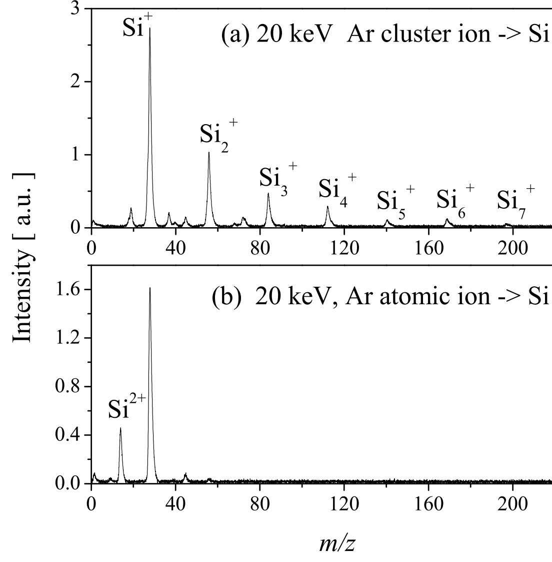

Figure 3.1: Secondary ion spectra of Si obtained with cluster and Ar atomic ions at 20 keV [47)]

In methods based on TOF-MS, emitted ions are accelerated through an electric field into a field-free region, and transported to a detector installed at the end of the field-free region. Light ions fly faster than heavy ions in the field free region because every ion has same energy, and thus arrive earlier at the detector. In this experiment, we measured the flight time only in the field-free region; therefore the calculation of flight time was very simple. The secondary ion energy E is expressed as

$$E = zV + E_0 \tag{3.1}$$

where z, V and E_0 correspond to the charge of ions, acceleration voltage and initial energy of the secondary ions, respectively. When energetic ions fly in the field-free region of length L, the flight time t of the ions is given by

$$t = L\sqrt{\frac{m}{2zV + 2E_0}} \tag{3.2}$$

The mass resolution of the analyzer is defined by the pulse width, Δt_p,

the energy distribution leading to a flight time difference Δt_E for different ions with the same mass, and the precision of the registration system Δt_d,

$$\frac{m}{\Delta m} = \frac{t}{2\Delta t} = \frac{t}{2\sqrt{\Delta t_p^2 + \Delta t_E^2 + \Delta t_d^2}} \tag{3.3}$$

Because the emitted secondary ion has an energy distribution width of a few eV, Δt_E is typically the largest of the three, and a reflectron SIMS system is widely used for reducing Δt_E. However, Δt_p is larger than Δt_E in gas cluster-SIMS because the GCIB has a wide velocity distribution, and therefore in this study we measured the time-of-flight by a linear TOF-SIMS system. In this study, zV was 2 keV and L was 400 mm. For an ion of m/z 100 the following values were calculated: $t = 6.4\ \mu s$, $\Delta t_p = 0.1\ \mu s$ and $\Delta t_E = 0.02\ \mu s$, suggesting that the estimated $m/\Delta m$ was about 30 in this SIMS measurement.

3.2.2 Size selected SIMS

Figure 3.2 presents the experimental setup for cluster-SIMS. The basic setup of the irradiation system was similar to that described in Ch. 2, but in this system the second primary ion beam deflector was removed. The target chamber was separated from the ionization chamber with two apertures for differential evacuation in order to keep target chamber under high vacuum ($\leq 10^{-6}$ Pa). The secondary ions were measured using a linear TOF system and detected by a microchannel plate detector(MCP).

Figure 3.3 presents the schematic diagram of the TOF-SIMS technique for size-selected ions. First, the primary ion beam is chopped to a width of 5 μs by a high-voltage pulse applied between the parallel electrodes installed along the beam line. Before the pulsed ion beam hits the target, the pulse widens beyond 100 μs because of the size difference between the incident cluster ions. The primary cluster ion beam is continuously bombarded onto the target at an angle of 45 degree with respect to the surface normal, and secondary ions are emitted. Then, the secondary ions are extracted with a parallel electrode and reach a secondary ion deflector installed between the target and the secondary ion detector. This secondary ion deflector is known as the interleaved comb ion mass deflection gate (Fig. 3.4). The

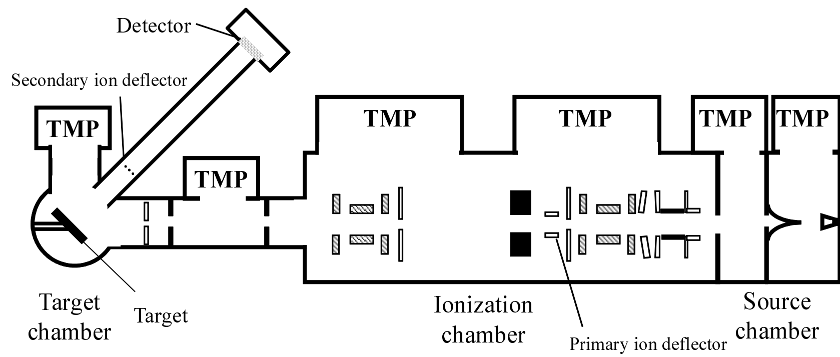

Figure 3.2: The experimental setup for size-selected SIMS

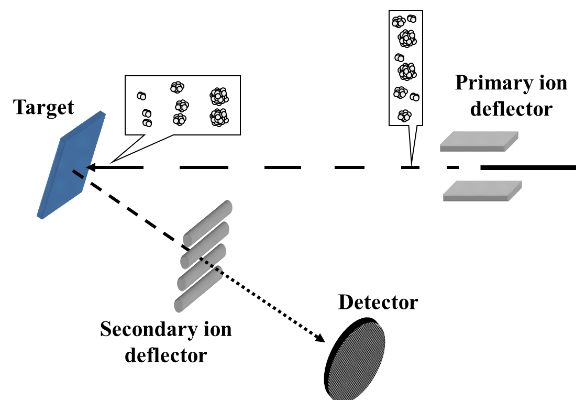

Figure 3.3: Schematic diagram of the size-selected SIMS

secondary ion deflector consists of two electrically insulated sets of thin wires mounted parallel to each other and perpendicular to the target surface normal. The wire diameter is 0.35 mm and the distance between wires is 0.85 mm. Finally, the secondary ion beams are chopped to a width of 200ns by applying a relatively low voltage pulse between the wires.

We could selectively measure secondary ions produced by different sizes of cluster ions by changing the time interval (delay time) between the primary and the secondary ion beam chopping. The pulse repetition rate of primary ion and secondary ion chopping was 1000-10000 Hz. Secondary ion were extracted with 2 keV kinetic energy and detected with MCP set on

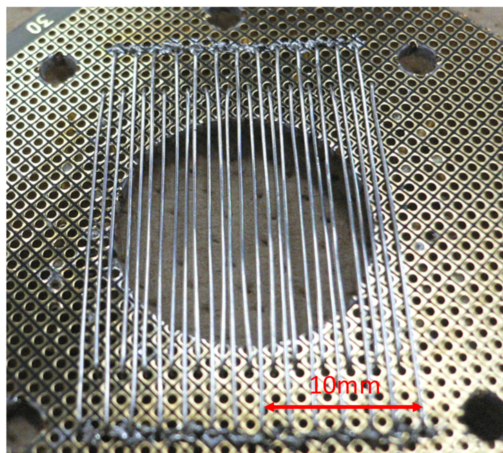

Figure 3.4: The secondary ion deflector

the axis of the surface normal. The incident cluster size resolution of size selected gas cluster was about the same as that described in Ch. 2.

The cluster size distribution before size-selection is shown in Figure 3.5. In this experiment, the inlet gas pressure was about 0.7 MPa and the average cluster size was about 1000 atoms. The number of incident cluster ions was estimated from this size distribution.

Figure 3.6 presents a schematic diagram of the TOF electronics used in this study. A pulse generator, DG535, generated pulses for both the primary and secondary ion beam chopping to a high voltage (H.V.) switching circuit. The pulse to the switching circuit of the secondary ion chopper was also provided as a start pulse into a fast multi-channel scalar (SRS: SRS430). The output from the MCP was amplified with an ORTEC 9306 preamplifier and was provided as a stop pulse into MCS.

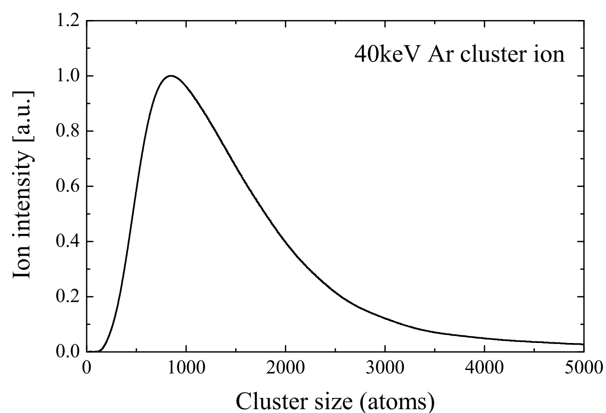

Figure 3.5: Size distribution of Ar cluster ion beam with total energy of 40 keV

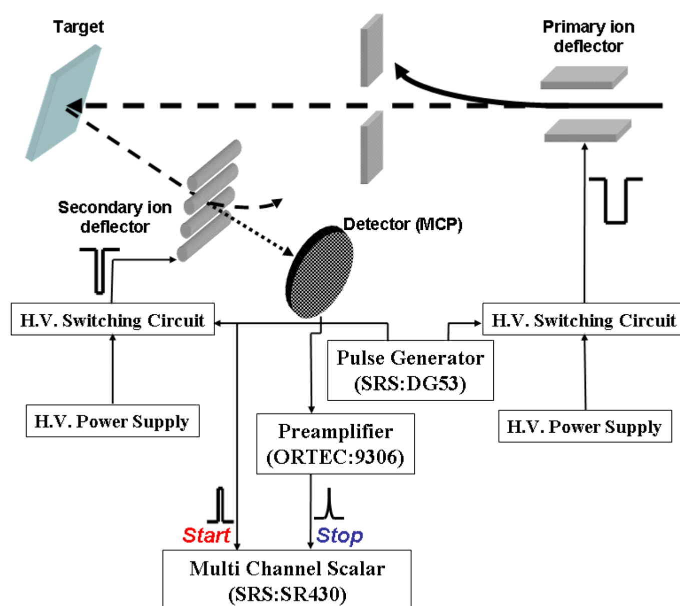

Figure 3.6: Schematic diagram of the electronic components used in this TOF-SIMS

3.3 Results-Si target

3.3.1 Secondary cluster ion emission

For irradiation of the Si (100) target, the oxidized surface layer was etched with Ar GCIB in the high-vacuum ($\leq 10^{-6}$Pa) target chamber before SIMS measurements. The incident cluster energy was in the range 10-60 keV and the cluster size was in the range of 300-2500 atoms/ion.

Figure 3.7 represents the secondary ion spectra obtained under the incidence of 40 keV Ar_{300}(133 eV/atom), Ar_{600}(67 eV/atom) and Ar_{1100}(36eV/atom). The secondary ion intensity was normalized to the intensity of Si^+. Under 40 keV Ar_{300} bombardment,mainly Si^+ ions were detected, and the yields of Si cluster ions such as Si_3^+ and Si_4^+ were extremely low compared to that of Si^+. In contrast, the ratio of Si cluster ion yield was clearly high with 40 keV Ar_{1100} bombardment, suggesting that the secondary ion species intensities are strongly dependent on the incident cluster condition for the same total energy.

Figure 3.8 presents the intensity ratio of Si_n^+/Si^+ with 40 keV Ar_{300}, Ar_{600} and Ar_{1100}. In this experiment, Si cluster ions were detected with strong intensities up to Si_{11}^+. The cluster ion ratio increased with increasing impinging cluster size, and this effect was more enhanced for large secondary ions. For example, the ratios Si_3^+/Si^+ and Si_9^+/Si^+ with Ar_{1100} bombardment were about 6 and 30 times higher than with Ar_{300} bombardment, respectively. One of the possible reasons for the difference is the ionization probability of Si atomic and cluster ions. However, the difference in ionization potential of the Si atom and cluster hardly affects the ratio of Si cluster ion because the ionization potential of Si atom and clusters were only in the range of 7.5-8.5 eV.

The probability of cluster particle emission can be calculated by the ratio of secondary cluster ion and cluster size. The results of this calculation indicate that about 40 % of Si was emitted as single Si under 40 keV Ar_{300} bombardment, and only 5 % of Si was emitted as single Si under 40 keV Ar_{1100} bombardment. The intensity ratio of the Si cluster decreased with decreasing secondary cluster size, but that of Si_6^+ was higher than that of Si_5^+. This experimental result is attributed to the magic number of Si,

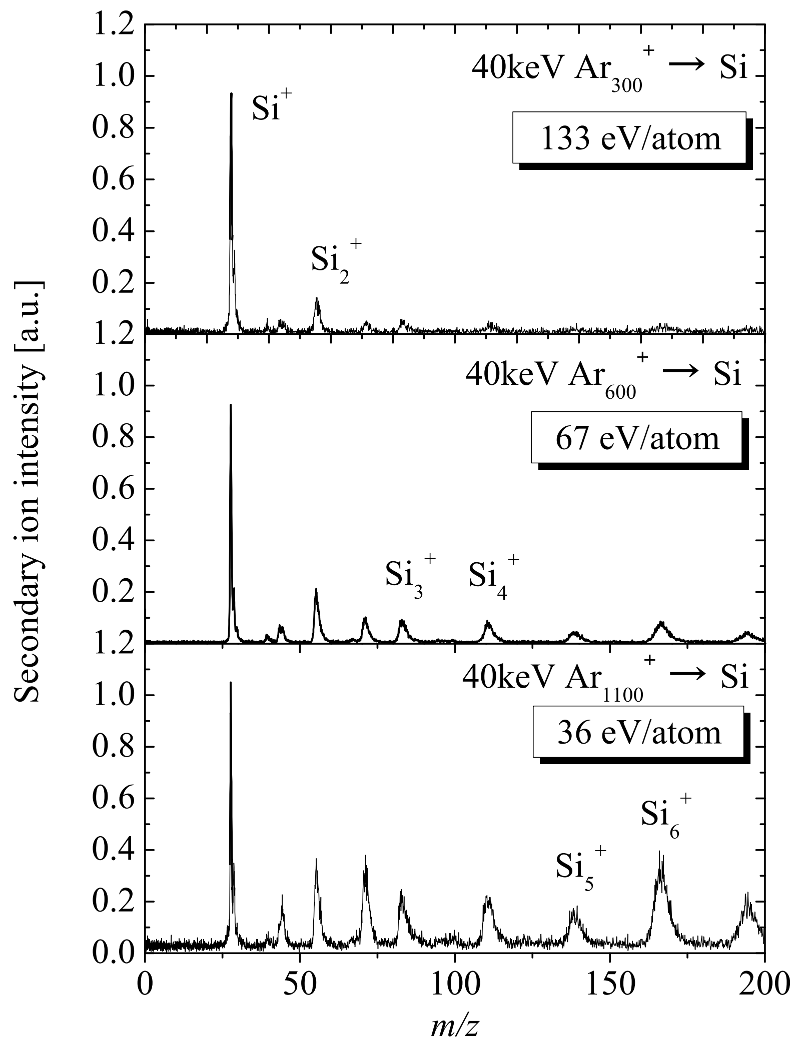

Figure 3.7: Secondary ion spectra of Si with various sizes of 40 keV Ar cluster ions

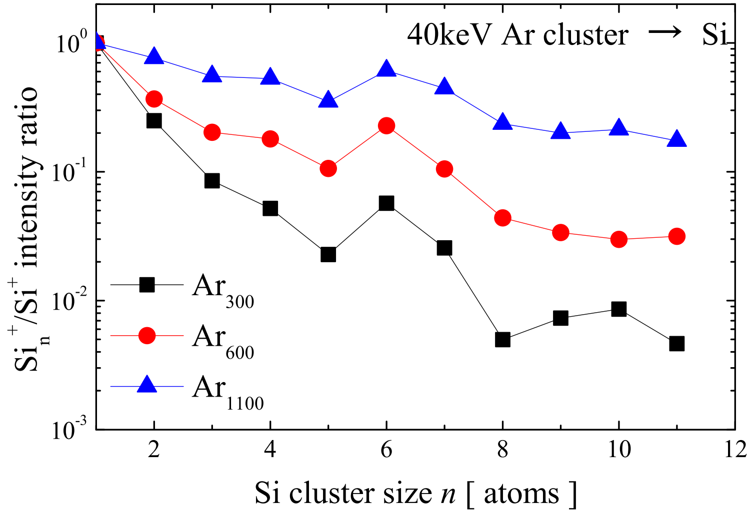

Figure 3.8: Secondary Si_n^+/Si^+ intensity ratio with Ar cluster ion bombardment at 40 keV

and in good agreement with other experimental reports with Au cluster bombardment and laser ablation [48, 49)].

As mentioned in Ch. 2, the irradiation effects were strongly affected by the incident cluster size and incident energy-per-atom. The incident size and energy-per-atom effects on secondary cluster ion emission are shown in Figure 3.9. The secondary cluster ion intensity ratio with 10 keV Ar_{400} and 40 keV Ar_{1500} bombardment were approximately the same for every size of Si_n^+, although the total energy of 40 keV Ar_{1500} is 4 times higher than 10keV Ar_{400}. On the other hand, the intensity ratios of the secondary Ar_{300} cluster ion with 10 and 40 keV were far from each other. For instance, the ratio of Si_6^+/Si^+ with 10 keV Ar_{300} was 0.72 and this value was more than one order of magnitude higher than the value of 0.06 obtained with 40keV Ar_{300}. This result indicated that secondary ion emission was strongly dependent on the energy-per-atom in the incident cluster, and the effect of the actual incident cluster size would be very small.

Figure 3.10 presents the effect of the incident energy per atom on the

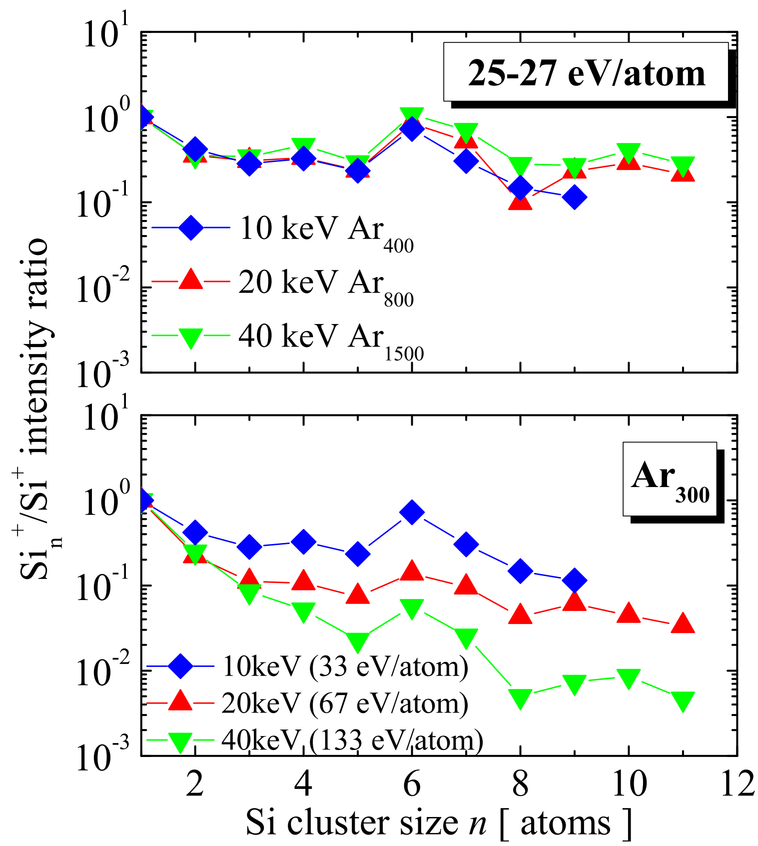

Figure 3.9: Effects of incident size and energy-per-atom on secondary cluster ion intensity

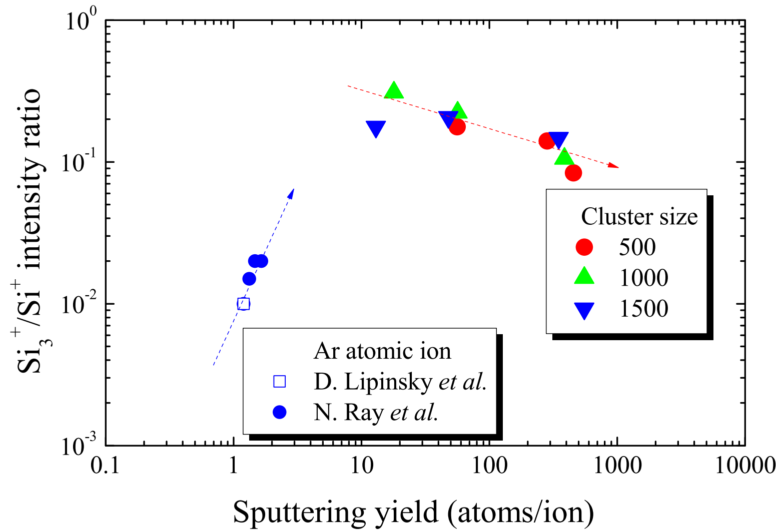

Figure 3.10: The effect of incident energy per atom on the intensity ratio Si_3^+/Si^+

value of the Si_3^+/Si^+ ratio under Ar cluster and atomic ion bombardment. Under cluster ion bombardment, the ratios Si_3^+/Si^+ clearly decreased with increasing incident energy per atom under each cluster size. The Si_3^+/Si^+ ratio with 3 keV Ar atomic ion was lower than with 200 eV/atom Ar cluster ion bombardment. However, under bombardment with atomic ions, the Si_3^+/Si^+ ratio increased with increasing incident energy, indicating that the secondary cluster particle emission process is different for cluster or atomic ion bombardment.

Two models of cluster particle emission from the target surface are shown in Figure 3.11. Cluster particles are either emitted directly from the surface (a), or recombined after emission (b). Under atomic ion bombardment, target atoms and energies are transferred by binary collisions, and matter is mostly sputtered as individual atoms. Therefore, the secondary cluster species would not leave the surface as clusters, but rather form in a region above the surface [50, 51, 52]. This is called the "recombination model" and is shown in Fig. 3.11 (b). In this model, the secondary cluster ratio

increases with increasing sputtering yield.

Reports of experiments and MD simulations have shown that the cluster ion ratio increased with increasing sputtering yield under atomic or small cluster impact [53, 54, 55]. On the other hand, in the direct emission model, cluster particles are emitted from the surface as clusters when many surface atoms are energized at the same time. In this model, the ratio of cluster particles decreases with increasing deposition energy because high energy deposition breaks the secondary clusters. Direct emission of cluster particles has also been reported in experiments and MD simulations [56, 57, 58]. Experimentally, it has mainly been reported in laser ablation and thermal evaporation. The deposited energy density with laser ablation is around 100 mJ/cm^2, more than one order of magnitude lower than the value for atomic ion bombardment. Moreover, the sputtering phenomena observed with energetic atom bombardment result from binary collisions. Therefore, it would be difficult to obtain direct emission of cluster particles by atomic ion or small cluster ion bombardment. With large cluster impacts the deposited energy density was as large as for laser ablation and the thermal spike deposits energy to many surface atoms at the same time.

Figure 3.12 represents the value of the Si_3^+/Si^+ ratio as a function of deposited energy density by cluster ion bombardment. The incident energy density was calculated taking into account cluster energy and cluster cross section. The van der Waals radius of the argon atom was calculated to be of 0.19 nm. The secondary cluster ion ratio decreased exponentially with deposited energy density, and this result was in good agreement with reports on laser ablation. This dependence of secondary cluster intensity ratio on deposited energy does however not work wwll for high-energy cluster ion bombardment. Indeed, the sputtering yield with this kind of cluster was higher than 500 atoms/ion as shown in Ch. 2, therefore recombination would be as large as direct emission under these conditions.

3.3.2 Enhancement of Si^+ emission

Figure 3.13 represents the Si^+ yield per incident ion with 40 keV Ar cluster at various cluster sizes. The Si^+ yield was calculated from the secondary

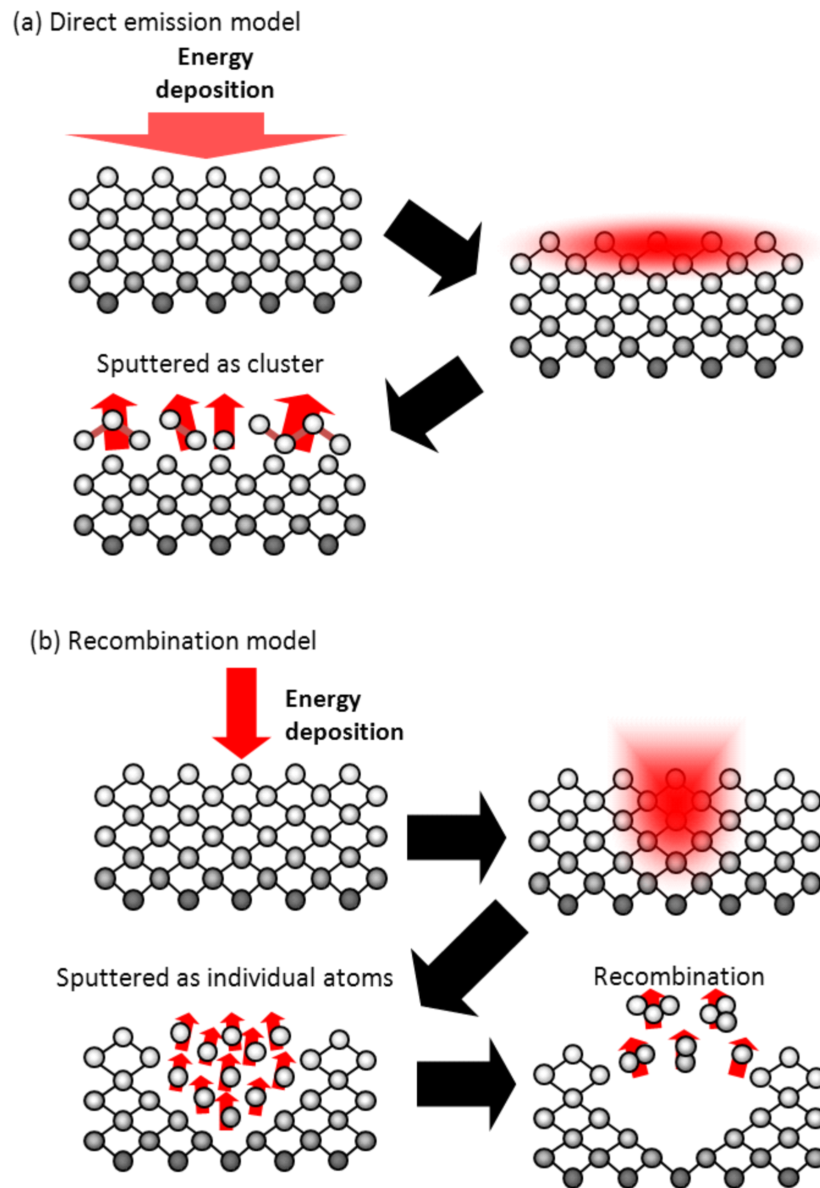

Figure 3.11: Models of secondary cluster particle emission

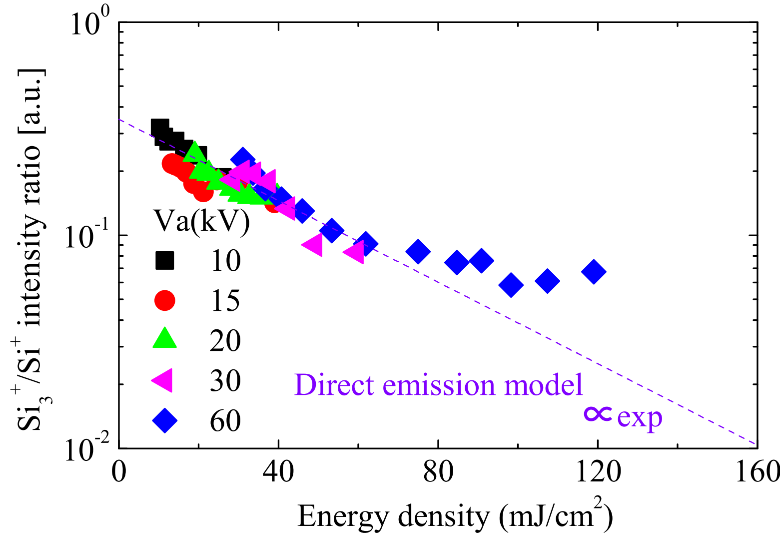

Figure 3.12: The effect of deposited energy density on the intensity of Si_3^+/Si^+ (V_a is 'acceleration energy')

ion counts and the number of incident cluster ions, as measured from the cluster size distribution shown in Fig. 3.5. As shown in the Fig. 3.13, with small clusters the Si^+ yield was almost steady and did not vary with cluster size but was dependent on total energy. Under large cluster ion bombardment, the secondary ion yield decreased with increasing incident cluster size and this shows the same tendency as the sputtering yield. Si^+ yield with 40 keV Ar cluster was one to two orders of magnitude higher than that with 40 keV Ar atomic ion bombardment.

The Si sputtering yield with 40 keV Ar cluster was also one to two orders of magnitude higher than that with 40 keV Ar atomic ion bombardment, indicating that the ionization probability of sputtered Si with Ar cluster ion was as large as that with Ar atomic ion, although the incident energy per atom of Ar cluster ion is much lower than an Ar atomic ion. The ionization probability is strongly dependent on the incident ion and target species, and the kinetic energy of the secondary particle. The effect of kinetic energy on the ionization probability P_i is simply described as follows;

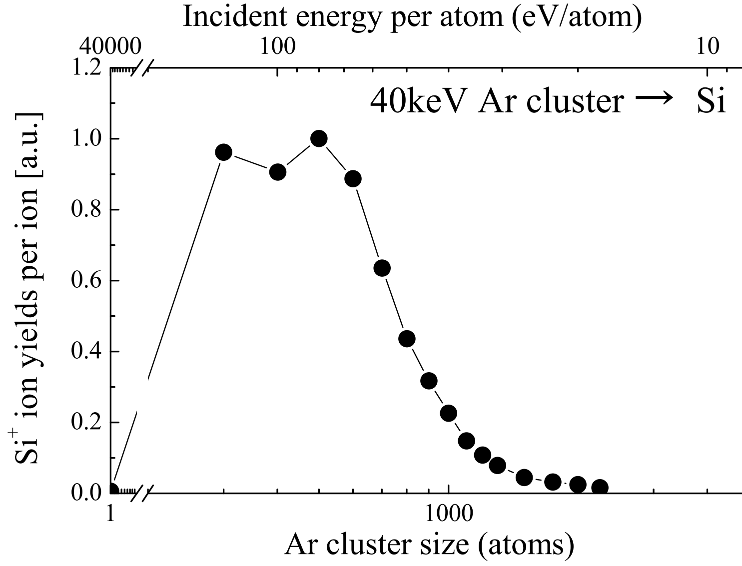

Figure 3.13: Si^+ intensity with various sizes of 40 keV Ar cluster ion

$$P_i = exp(-bE_i^{-0.5}), \tag{3.4}$$

where b is a fitting parameter that depends on the ionization potential and E is the kinetic energy of the secondary particle [59, 60]. The kinetic energy of the secondary particle would be about the same under Ar atomic or cluster ion bombardment.

A comparison of the Si sputtering yield and the Si^+ yield under 60 and 20 keV Ar cluster ion bombardment is shown in Fig. 3.14. The secondary ion intensity Y_i can be described as

$$Y_i(E) = P_i \times Y(E), \tag{3.5}$$

where P_i is ionization probability and Y is sputtering yield. As shown in Fig. 3.14(a), the effect of incident energy per atom on secondary ion and sputtering yield is the same under bombardment at high energy per atom ($\geq$ 40eV/atom). It indicates that the ionization probability of these

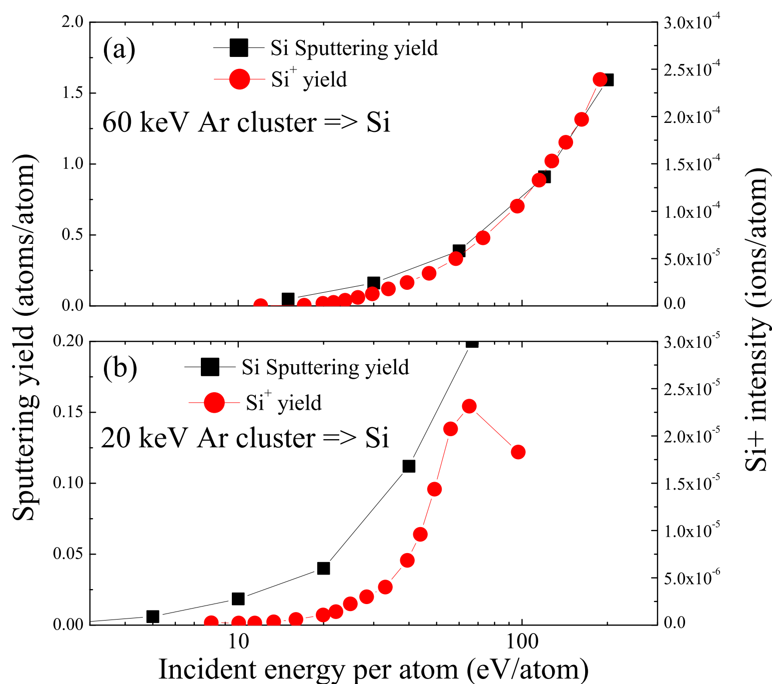

Figure 3.14: Variation of Si and Si^+ yield with incident energy per atom and cluster size for size-selected 20 and 60 keV Ar cluster ion beams.

clusters is independent on the condition of the incident cluster. As shown by solid circles in Fig. 3.14 (b), the secondary ion yield decreased with decreasing incident energy per atom more rapidly than the Si sputtering yield.

When the energy per atom of the bombarding cluster was higher than 20eV/atom, Si and Si^+ were emitted from the Si surface with high intensity. On the other hand, when energy per atom of the bombarding cluster was about 10 eV/atom, Si^+ ions were rarely emitted, although neutral Si atoms were still emitted. The threshold energy of incident cluster ion for Si^+ emission was estimated to be about 8 eV/atom, which was a few times higher than the threshold energy for Si sputtering. This difference between Si and Si^+ emissions is attributed to the ionization process of sputtered Si

particles.

The ionization energy of Si is 8.16 eV and it is about the same as the threshold energy per atom of Si^+ emission, and much higher than the binding energy of Si, 3.4 eV. The secondary particle cannot have enough kinetic energy to ionize under bombardment with cluster ion with low energy per atom. This result indicates that the surface atoms were easily sputtered with cluster ion bombardment because of multiple collisions, but the sputtered particles couldn't gain sufficient energy to become ionized when the energy per bombarding atom was at a value between sputtering and ionization threshold energy and only neutral particles were emitted.

3.4 Results-Organic materials

Atomic ion beams produce weak signals for large organic molecules because of critical problems, such as low sputtering yield and damage to biomolecules. Cluster ions such as C_{60}^{+} and Au_3^{+} have been studied as primary ions for SIMS [61, 62], because yields of both neutral and ionized particles increase considerably with cluster size. However, even cluster ions could not solve the problem of damage to biomolecules caused by incident ions. GCIB was proposed to be one of the solutions to the problem of sputtering organic and polymeric materials without damage [63].

Figure 3.15(a, b) presents the mass spectra of positively charged secondary ions emitted from a leucine ($C_6H_{13}NO_2$, 131 u, one of the amino acids) film with 8 keV Ar cluster and Ar atomic ion, respectively. Protonated leucine molecular ions ($C_6H_{14}NO_2^{+}$, $m/z = 132$) and characteristic fragment ions such as $m/z = 44$ (CO_2^{+}) and $m/z = 86$ ($C_5H_{12}N^{+}$ or $[\text{m-COOH}]^{+}$) were detected with high intensity. The yields of protonated leucine molecular ions emitted by Ar atomic ions were extremely low compared to fragment ions. In contrast, the yields of protonated leucine molecular ions emitted by Ar cluster ions were the same or higher than those of fragment ions, indicating that large gas cluster ions can sputter and ionize leucine molecules with little damage. In this section, we investigate the effect of the bombarding cluster condition on the damage to the surface and on secondary ion emission in polymethylmetacrylate (PMMA), tris(8-hydroxyquinoline)aluminum (Alq3), Arginine and Phenylalanine.

Figure 3.16 presents the molecular structure of PMMA, Alq3, arginine and phenylalanine. PMMA is one of the typical polymeric materials. Its repeated unit is $C_5H_8O_2$ (m = 100 u), and its molecular weight (Mw) was 700,000-750,000 in this study. Alq3 is one of the components of organic light-emitting diodes (OLED). Its composition formula is $C_{27}H_{18}AlN_3O_3$ (m = 459.4 u). Arginine and phenylalanine are amino acids, and their composition formulas are $C_6H_{14}N_4O_2$ (m = 174 u) and $C_9H_{11}NO_2$ (m = 165 u), respectively.

PMMA, arginine and phenylalanine were obtained from Nacalai Tesque Inc. (Kyoto, Japan). Alq3 was obtained from Chemipro Kasei Kaisha,

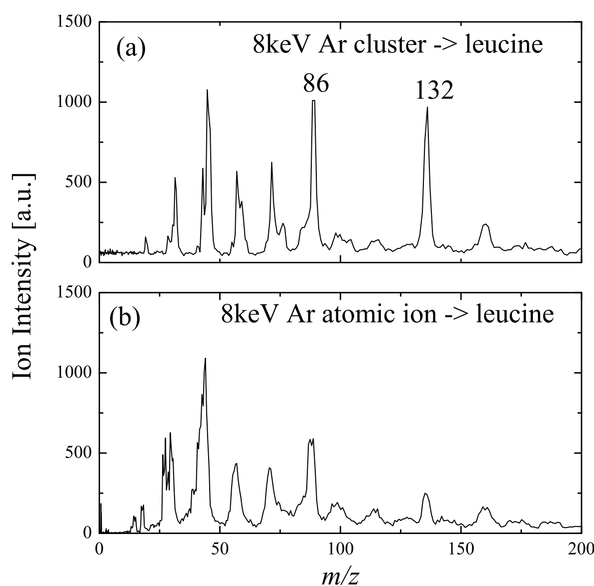

Figure 3.15: Secondary ion spectra of leucine obtained with 8 keV Ar cluster and atomic ion bombardment

LTD. (Hyogo, Japan). The PMMA and arginine films were prepared by spin-casting method, and the Alq3 and phenylalanine films were prepared by vapor deposition method on clean silicon substrates. The silicon substrate was washed with water, ethanol and acetone in an ultrasonic cleaner. PMMA was dissolved in toluene as a 2 wt% solution, and arginine was dissolved in water as a 15 wt% solution. The thickness of the organic films was about 100-200 nm.

Figure 3.17 presents the mass spectra of positively charged secondary ions emitted from the arginine film under bombardment with 11 keV Ar_{600}, Ar_{1200} and Ar_{2500}. The secondary ion intensity was normalized to the intensity of the protonated arginine molecular ion, $m/z = 175(C_6H_{15}N_4O_2^+$ or $[m+H]^+$). Under 11 keV Ar_{600} bombardment, m/z = 45 and 70 also had strong intensities, and they were assigned as $COOH^+$ and $C_4H_8N^+$, respectively. As shown, the intensity ratio of fragment ions to the arginine ion decreased with increasing incident cluster size, and the characteristic fragment ions were hardly detected under 11 keV Ar_{2500} bombardment,

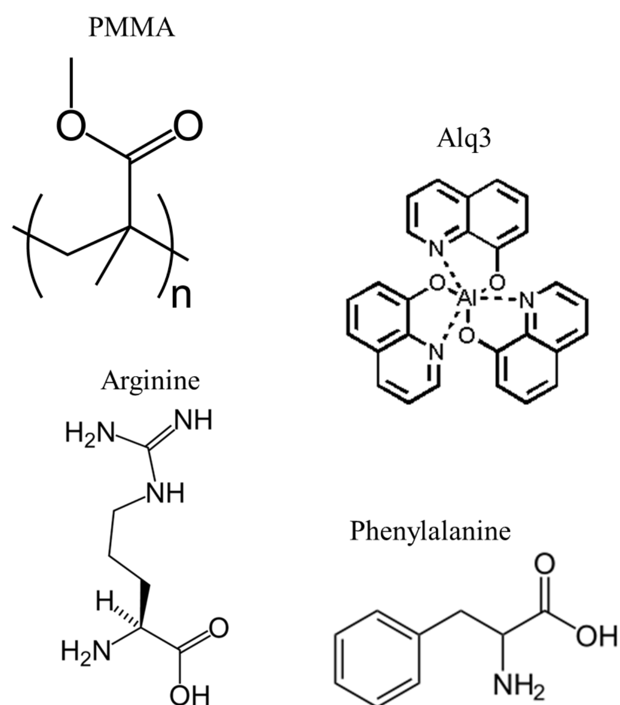

Figure 3.16: Schematic diagrams of the molecular structures of the organic targets

because the bond association energy of C-O and C-C is stronger than the van der Waals energy between arginine molecules, and the incident energy per atom of 11 keV Ar_{2500} (4.4 eV/atom) was similar to the bond association energy of C-O and C-C.

Figure 3.18 presents the mass spectra of positively charged secondary ion emitted from the phenylalanine film with 11 keV Ar_{600}, Ar_{1200} and Ar_{2200}. The secondary ion intensity was normalized to the protonated phenylalanine molecular ion, $m/z = 166(C_9H_{12}NO_2^+$ or $[m+H]^+)$. A characteristic fragment ion was also observed at $m/z = 120$ ($C_8H_{10}N^+$ or $[m+COOH]^+$). The intensity ratio of fragment ions to the phenylalanine ion decreased with increasing incident cluster size, like for arginine. In the case of phenylalanine, protonated phenylalanine dimer ($m/z = 331$) was detected with Ar cluster ion bombardment. The intensity ratio of the dimer increased with increasing incident cluster size, and was seen to be as large as the protonated single phenylalanine under 11 keV Ar_{2200}. The threshold energy per atom for no-damage processing was the same for phenylalanine and arginine because these structures are close.

Figure 3.19 presents the intensity ratio between the characteristic fragment ion and the protonated molecular ions of arginine and phenylalanine targets. The intensity ratio of the fragment ions was about the same under cluster ion bombardment with high energy per atom ($\geq$20 eV/atom), but decreased drastically with low energy per atom below 10 eV/atom. Under cluster ion bombardment with 5 eV/atom, the fragment intensity ratio was one order of magnitude lower than that of the protonated molecular ion.

Figure 3.20 presents the mass spectra of positively charged secondary ions emitted from the PMMA film bombarded with 8 keV Ar atomic ions, Ar_{500} and Ar_{2000}. The secondary ion intensity was normalized to the intensity of characteristic fragment $m/z = 69(C_4H_5O^+$ or $[m\text{-}OCH_3]^+)$. Under atomic ion bombardment, $m/z =55$ ($C_4H_7^+$) also had strong intensity, and the large ion of protonated MMA (m/z=101) was not detected. Under bombardment with large cluster ions, the protonated MMA ion was clearly detected. However, the secondary ion spectra with Ar_{500} and Ar_{2000} seem to be similar, and this is different from the results of amino acids. This could be attributed to the difference in bond energy between PMMA and

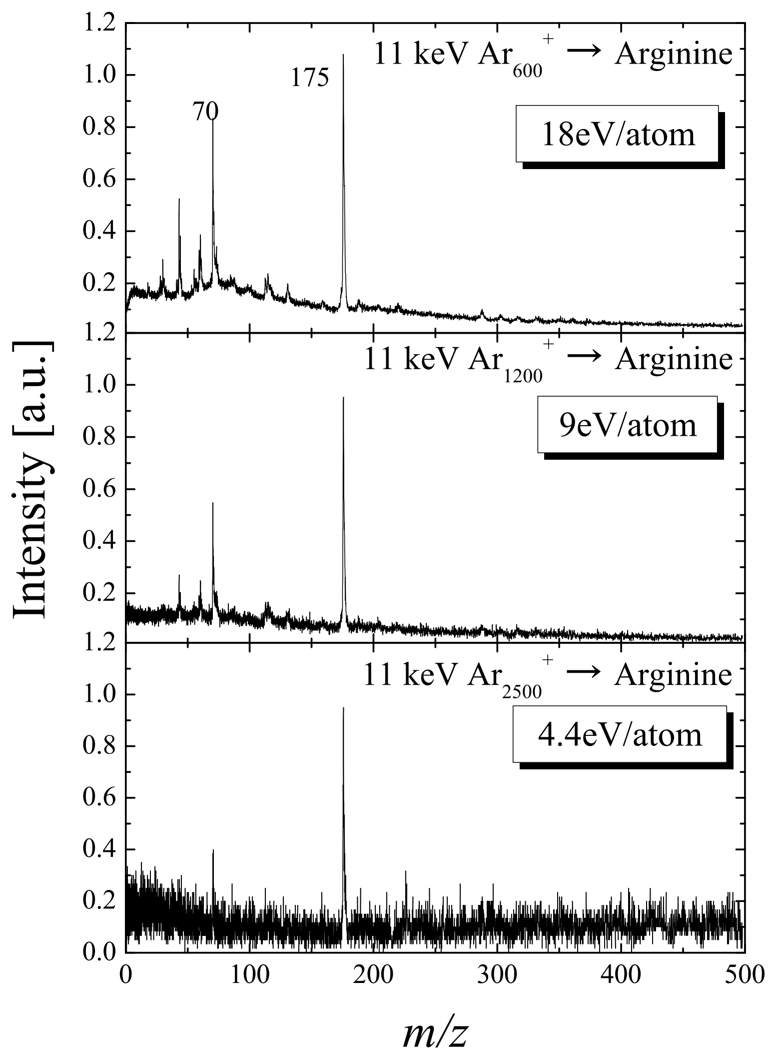

Figure 3.17: Secondary ion spectra of arginine with 11 keV Ar cluster ion bombardment

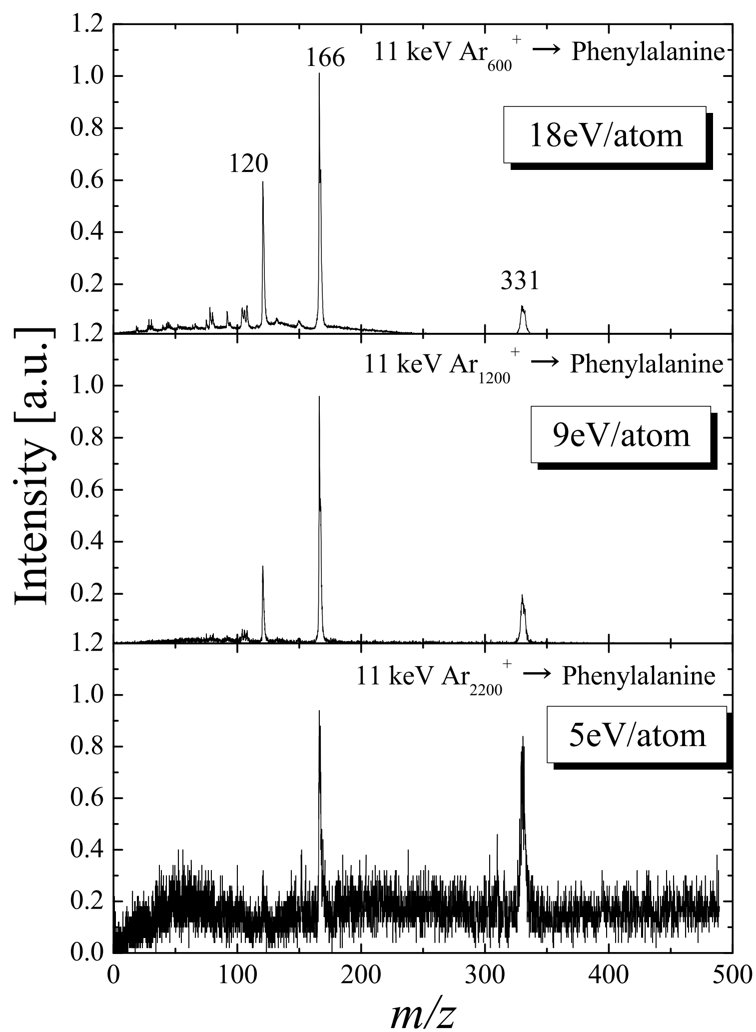

Figure 3.18: Secondary ion spectra of phenylalanine with 11 keV Ar cluster ion bombardment

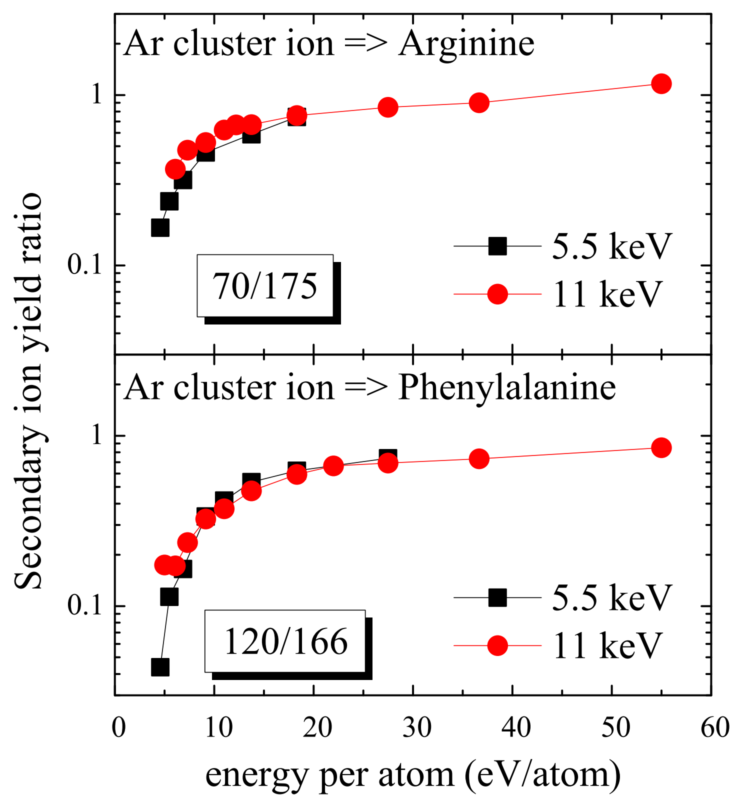

Figure 3.19: Secondary ion intensity ratio between the characteristic fragment ion and the protonated molecular ion

amino acids. The bonding energy working between amino acid molecules is the van der Waals force, which is much weaker than the bond association energy of C-O and C-C. On the other hand, the bonding energy between MMA is C-C bonding and the association energy of C-C bonding is equal to that of C-O bonding. If the C-O bonding between C_4H_5O and OCH_3 was stronger than the C-C bonding between MMA molecules, the intensity of MMA would increase under bombardment with low energy per atom. However, the intensity ratio of $C_4H_5O^+$ to MMA with Ar_{500} was lower than that with Ar_{2000} . Therefore, the bond association energy of C-O bonding is smaller than that of C-C bonding. The C-O bonding was broken by energy deposition first, C-C bonding was broken second, and then the particles were emitted from the PMMA surface. Under cluster ion bombardment with the energy of 4 eV/atom, e.g., the Ar_{2500} cluster at 10 keV, the Si^+ yield decreased drastically compared to the high energy-per-atom cluster ion bombardment, such as 10 keV Ar_{600} (17 eV/atom). However, the secondary ion intensity of PMMA with 8 keV Ar_{2000} was still high, because the ionization energies for organic molecules are lower than for Si.

Figure 3.21 presents the mass spectra of positively charged secondary ions emitted from the Alq3 film under bombardment with 13 keV Ar atomic ion, Ar_{250} and Ar_{1500}. With atomic ions under these conditions, m/z =27 (Al) was detected with high intensity, but no large particles were detected, indicating that the underlying structure of Alq3 was completely damaged. Under bombardment with 13 keV Ar_{250}, m/z = 27, 172, 188, 190 and 315 were detected and were assigned as Al^+, $Alq{+}H^+$, $Alq{+}OH^+$, $Alq{+}OH_3^+$ and $Alq2^+$. Alq3 surfaces were still damaged by 13 keV Ar_{250} bombardment, but the damage was much smaller than with Ar atomic ion bombardment because the intensity of $Alq2^+$ was as high as Al^+. When bombardment with 13 keV Ar_{1500} was used on Alq3, most of the secondary particles were emitted as $Alq2^+$, and there was much less surface damage than that with 13 keV Ar_{250}. The threshold energy of Alq3 for no-damage processing was higher than 8.6 eV/atom, and this relatively high value compared to the amino acids is attributed to the binding energy between Al and q(C_9H_6NO). As mentioned earlier (see Fig. 3.16), Al and q are held together with both Al-O and Al-N bonding, therefore the threshold

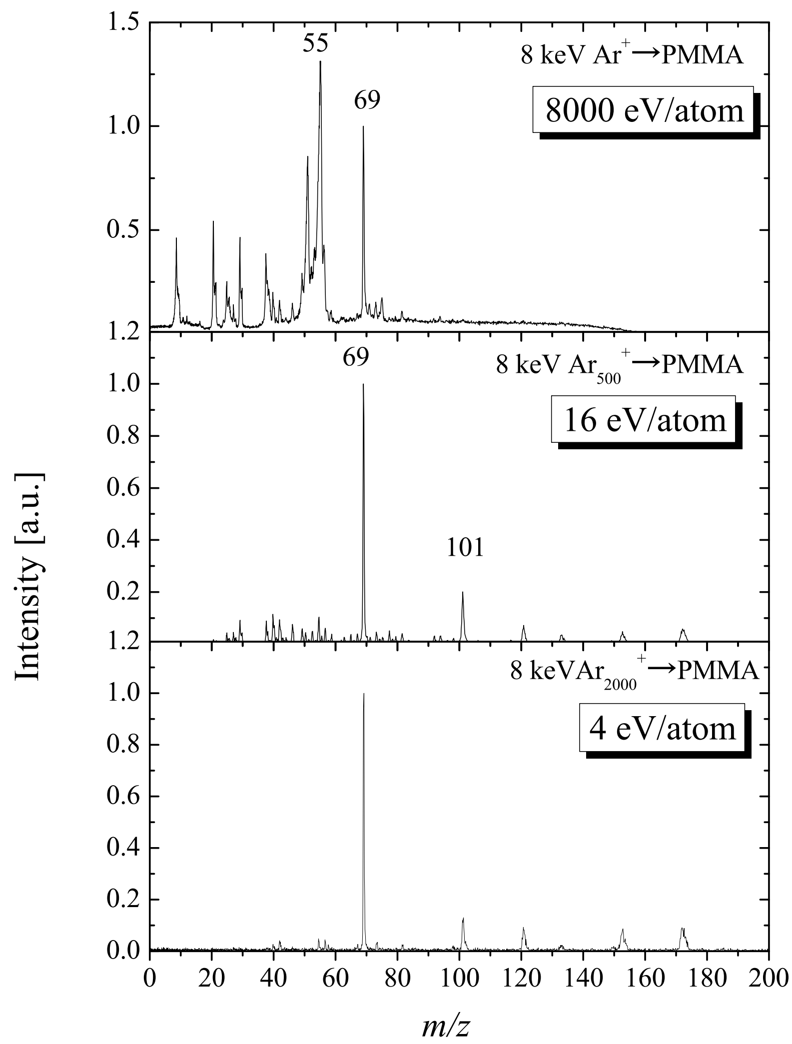

Figure 3.20: Secondary ion spectra of PMMA with 8 keV Ar cluster and atomic ion bombardment

energy is higher than that of amino acid. As mentioned in Ch. 2, the sputtering yield of PMMA with 20 keV Ar_{8000} (2.5 eV/atom) was more than 600units/ion, which was more than half of that observed with Ar_{2000} at the same total energy. Therefore, both low damage and high speed etching can be achieved concurrently by controlling the incident cluster ion condition (size and energy).

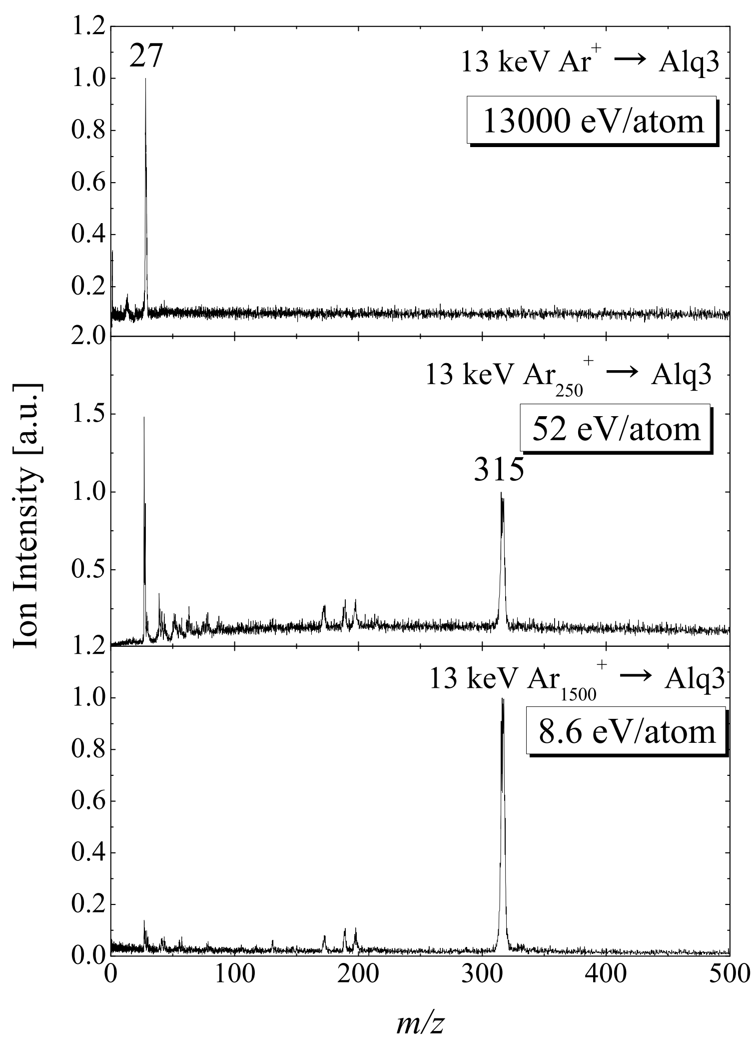

Figure 3.21: Secondary ion spectra of Alq3 with 13 keV Ar cluster and atomic ion bombardment

Chapter 4

Surface damage with GCIB

4.1 Low damage processing with GCIB irradiation

When GCIB bombards a surface with an energy per atom less than a few hundred eV/atom, the high-density energy deposition induces various irradiation effects. One of the characteristic irradiation effects caused by high-density energy deposition is enhancement of chemical reactivity, and for instance, a well-oxidized and smooth film can be formed by O_2 GCIB-assisted deposition at room temperature [8, 64].

Figure 4.1 shows the X-ray reflectometry (XRR spectra) of the Si surface before and after ion irradiation with 20 keV O_2. The average O_2 cluster size was 1500 molecules, and the irradiation dose was 1×10^{16} ions/cm^2. The thickness, density and roughness of each film were investigated by XRR with CuKα radiation on a computer-controlled reflectometer (Rigaku ATX. Osaka). The thickness of the oxidized films was calculated by the wavelength of the XRR spectra curve.

The oxidized film formed on the Si substrate before irradiation was not dense, and its wavelength was very long. On the other hand, a thick oxidized layer was formed by O_2 cluster ion irradiation, and the XRR spectrum was far from that of before irradiation. The estimated oxidized film thickness was about 12 nm. The blue line represents the surface state irradiated by O_2 molecular ions and there was little difference between the XRR spectra before and after O_2 molecular ion irradiation. It was thus found that ion irradiation with O_2 cluster considerably enhances surface

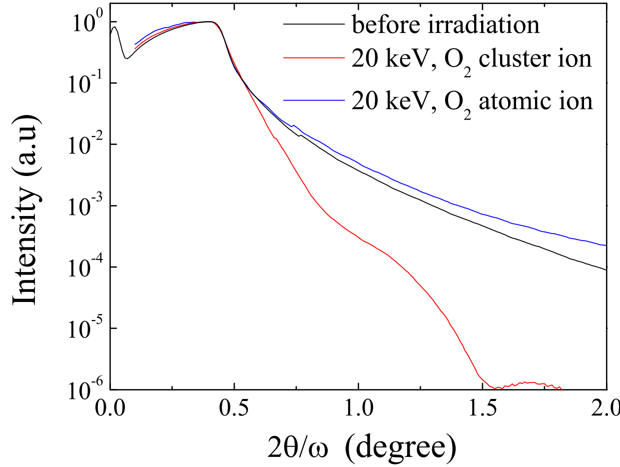

Figure 4.1: XRR spectra of the Si surface before and after O_2 ion beam irradiation the dose of 1×10^{16} ioss/cm^2.

oxidation compared to O_2 molecular ion.

When a GCIB bombards a surface, numerous surface atoms are energized and excited, and even the nonreactive GCIB excites the target surface and enhances the chemical reactions between target atoms and the gaseous atmosphere. The target surface would be oxidized by O_2 cluster ions both directly and indirectly. Direct oxidation is the reaction of O_2 cluster ions with the target surface, and indirect oxidation is the reaction of atmospheric O_2 gas with the target surface activated by the cluster ion irradiation. By contrast, only indirect oxidation occurs with Ar GCIB bombardment in O_2 atmosphere. The reactive probability for the direct reaction with O_2 cluster should be higher than for the indirect reaction because the energy of the constituent of O_2 cluster ion is higher than that of atmospheric O_2 gas.

Figure 4.2 shows the XRR spectra of the Si surface irradiated by 20 keV Ar cluster ion in O_2 atmosphere of 6.5×10^{-3} Pa (a) and (b) O_2 cluster ions. The irradiation dose of ion beam was 1×10^{16} ions/cm^2, in both cases and average cluster size of Ar cluster was 2000 atoms. The solid and dotted lines in Fig. 4.2 are, respectively, the experimental and simulated XRR spectra. The estimated thickness of the SiO_2 films formed by ion

irradiation with Ar and O_2 clusters was 15 and 12 nm, respectively.

Figure 4.3 shows secondary ion spectra of the Si target after oxidation by irradiation with (a) 20 keV Ar cluster ion irradiation in O_2 atmosphere of 6.5×10^{-3} Pa, and (b) 15 keV O_2 cluster ion. The secondary ions emitted from the Si surface were measured using a quadrupole mass spectrometer (ANELVA AQA-360). Their intensity was normalized to the intensity of Si^+. The SiO^+/Si^+ intensity ratio obtained from the Si samples oxidized by either irradiation with Ar cluster ion in O_2 atmosphere or O_2 cluster ion was similar. This means that is, the oxygen density of the surface oxidized by either Ar or O_2 cluster ion irradiation can be considered to be roughly the same and the Si surface was sufficiently excited for the oxidation reaction to occur by irradiation with the nonreactive cluster ion.

Figure 4.4 shows the variation in SiO^+ intensity with increasing oxygen partial pressure (P_o) during Ar cluster ion irradiation. The SiO^+ intensity increased linearly with P_o below 4×10^{-3} Pa, and remained constant with increasing P_o above 4×10^{-3} Pa. As the incident energy in this experiment was fixed at 20 keV, the excited and mixed volume on the surface by Ar cluster ion irradiation is expected to be kept constant. This correlation of the oxidation on O_2 partial pressure could be explained as follows.

(i) For the low P_o range ($P_o \leq 4 \times 10^{-3}$ Pa), the Si surface was excited and the top layer was mixed with cluster ion irradiation, but has not oxidized sufficiently because insufficient amounts of oxygen were supplied to the excited surface. Thus the SiO^+ intensity was proportional to P_o.

(ii) In the higher P_o range ($P_o \geq 4 \times 10^{-3}$ Pa) the Si surface was excited and the top layer that was mixed with cluster ion irradiation was fully oxidized by sufficient amounts of oxygen. Further additon of oxygen resulted only in excess atmosphere O_2, and thus the SiO^+ intensity became independent of P_o.

These experimental results indicate that the GCIB irradiation strongly affected the solid surface, and with 20 keV GCIB the affected depth was more than 10 nm. In other words, the surface structure was damaged more than 10 nm by 20 keV cluster ion irradiation, and this was much deeper than the penetration depth of an Ar atom with 10 eV, which is about 0.4nm. Of course, this irradiation effect of GCIB mainly depends on incident cluster

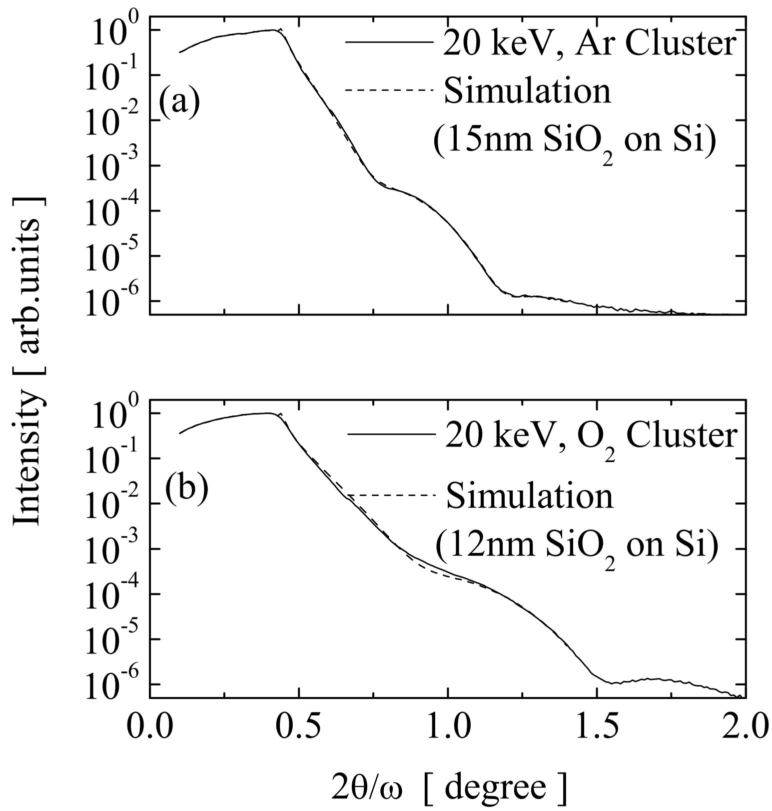

Figure 4.2: XRR and simulated spectra of the Si target after oxidation obtained with 20 keV GCIB irradiation at a dose of 1×10^{16} ions/cm^2 (a) Ar cluster ion (size 2000) in O_2 atmosphere at 6.5×10^{-3} Pa; (b) 20 keV O_2 cluster ion.

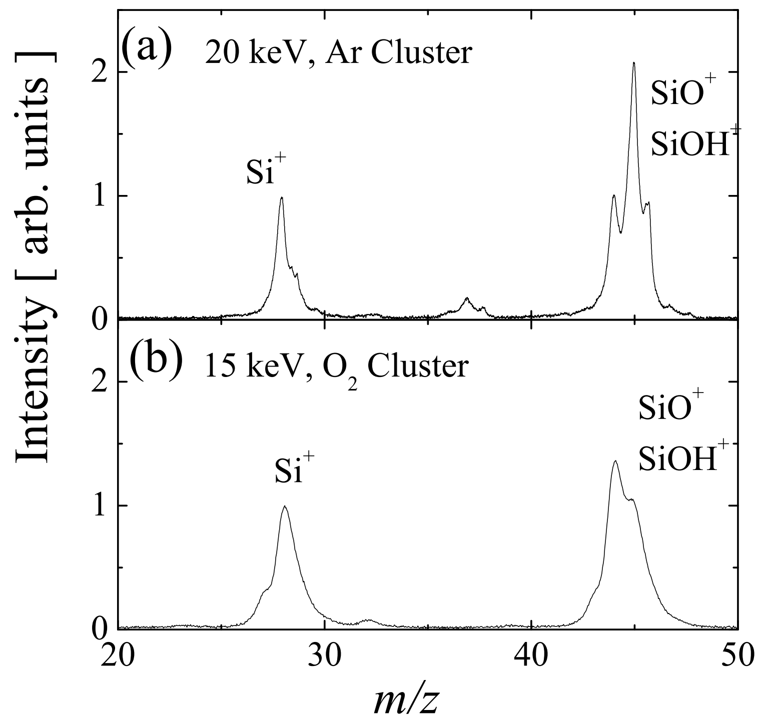

Figure 4.3: Secondary ion spectra of the Si target after oxidation obtained under irradiation with (a)20 keV Ar cluster ion irradiation in O_2 atmosphere at 6.5×10^{-3} Pa, and (b) 15 keV O_2 cluster ion.

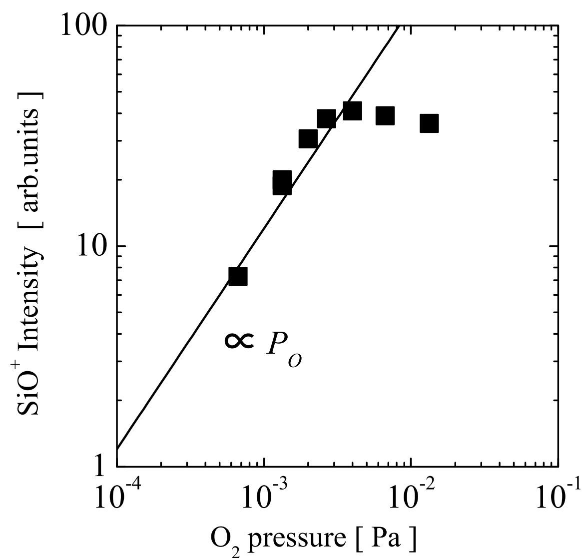

Figure 4.4: The SiO^+ intensities as a function of oxygen partial pressure during Ar cluster ion irradiation

energy, but also on incident cluster size. In this chapter, we discuss the effect of incident GCIB size and energy per atom on surface damage.

4.2 Surface damage-Si target

In this part if the work, crystalline Si (100) substrates were irradiated with Ar cluster ion beam and the thickness of the damaged surface layer was evaluated. The incident energy of cluster ion beam was in the range of 5-20 keV. The irradiation apparatus and size selection methods were the same as detailed in Ch. 2, and Ar GCIB irradiation was carried out at normal incidence. The Si target was rastered for uniform irradiation and the irradiated area was 4 mm $\times$ 6 mm. The incident cluster size was in the range 500-16000, and the ion dose was 1×10^{13} ions/cm^2.

The damaged layer thickness caused by irradiation of the Si substrate was characterized by ex situ ellipsometry measurements. The two optical parameters, the intensity ratio (Ψ) and phase difference (Δ) of the p and s waves can be measured at one laser wavelength and light incident angle. The ellipsometric parameters are related to the changes in amplitude and phase of the reflected polarized light. The thickness of the oxide and amorphous layers caused by various sizes and energies of cluster ions can be determined by using a two layer model. An increase in Ψ means increase in the amorphous layer thickness and a decrease in Δ means an increase in the oxide layer thickness. The total damaged layer thickness was defined as the sum of the amorphous and oxide layer thicknesses. The laser wavelength was 635 nm and the light incident angle was 75 degree.

Figure 4.5 presents Ψ and Δ plots after size-selected 10 keV Ar cluster ion irradiation on the Si substrate. The red and black lines represent the thickness of the oxide and amorphous layer (15 Å/line), respectively. Before cluster ion beam irradiation, the oxide layer thickness of the Si substrate was about 3 nm, and there was no amorphous layer. The surface damage with non-size-selected GCIB is shown as a red square, for comparison with size-selected cluster ions. The damaged layer thickness with non-selected cluster ion was similar to that with Ar_{1000} bombardment, although the mean size of the non-size-selected cluster was about 1500, indicating that the surface damage is more affected by small clusters than by large ones. The oxide layer thickness decreased with increasing incident cluster size. On the other hand, the amorphous layer thickness has maximum value at

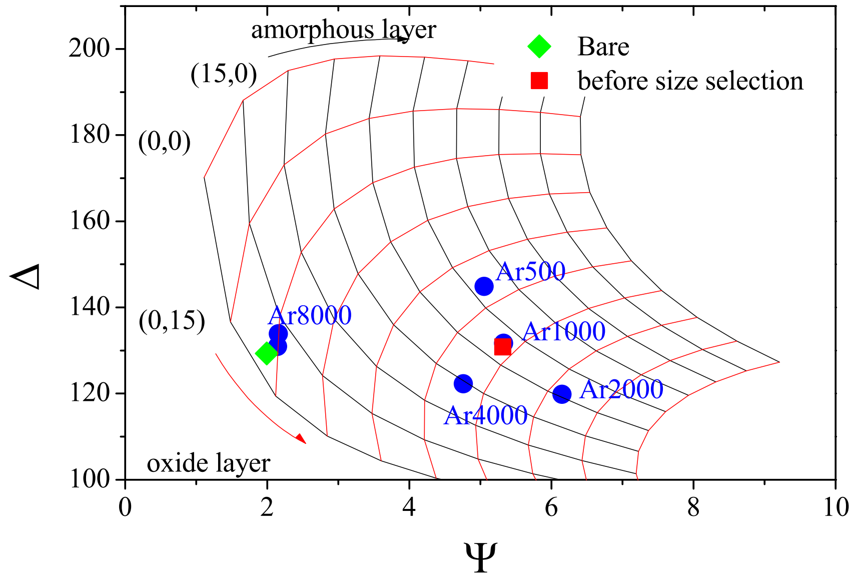

Figure 4.5: Ψ and Δ plots of Si substrates by ellipsometry measurements after unselected and size-selected 10 keV Ar cluster ion beam irradiation with fluence of 1 × 10^{13} ions/cm^2

Ar_{2000} bombardment. Between Ar_{4000} and Ar_{8000}, there was a sudden drop in the damaged layer thickness.

Figure 4.6 shows the effect of cluster size on the oxide (SiO_x) and amorphous (a-Si) layer thickness with size-elected 10 keV Ar GCIB bombardment. Blue triangles in the figure represent the sum of the layer thicknesses of silicon oxide and amorphous silicon. The oxide and amorphous layer thickness for Ar_{8000} and Ar_{16000} were about 3 and 0.2 nm, which is as large as the native oxide on the silicon substrate. As shown, the total damaged layer thickness with GCIB bombardment in the size range of 500-4000 was similar, although the thickness of the a-Si layer decreased with increasing incident cluster size, indicating that the mean depth of displacement does not depend on both incident cluster size and energy per atom but only the total incident energy if it is sufficiently higher than the damaging threshold energy. On the other hand, the damage depth decreased with decreasing

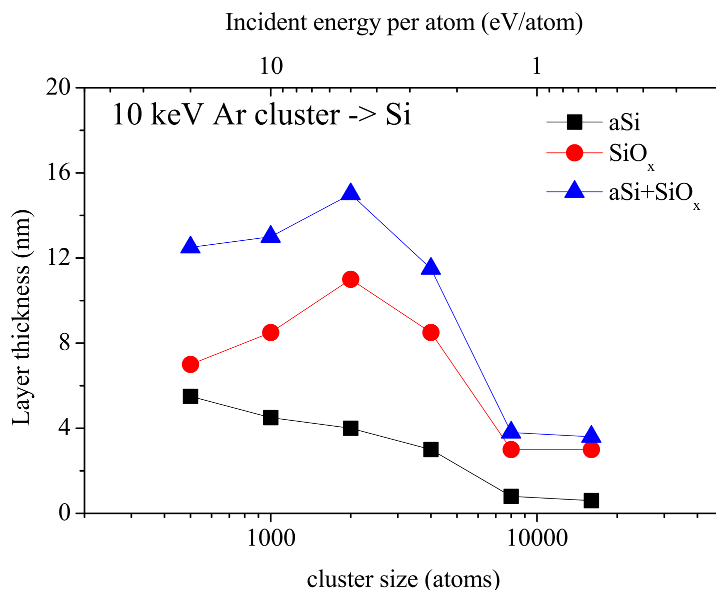

Figure 4.6: The effect of incident cluster size on the thickness of oxide(SiO_x) and amorphous(aSi) layer on Si substrates by 10 keV Ar GCIB

incident energy per atom when the value of this parameter was lower than about 10 eV/atom, which is same behavor than for the other irradiation effects such as sputtering and secondary ion emission. The thickness of the damaged layer with small cluster ion bombardment was smaller than the penetration depth with 10 keV Ar atomic ion, about 20 nm, as calculated with TRIM. Crater-like damage remained after gas cluster bombardment as mentioned in Ch. 2.

The sputtering yield with 10 keV Ar cluster ion was found to be of 5atoms, and the estimated crater depth of 1 nm. In MD simulation, the damage depth depends only on the total incident cluster energy, and the damaged depth is much deeper than the crater depth [27)]. The MD simulation was in good agreement with the experimental data. Figure 4.7 presents the effect of varying energy per atom on the damaged layer thickness for 5-20 keV size-selected GCIB. The damaged layer thickness was calculated as the sum of the layer thicknesses of silicon oxide and a-Si, both of which

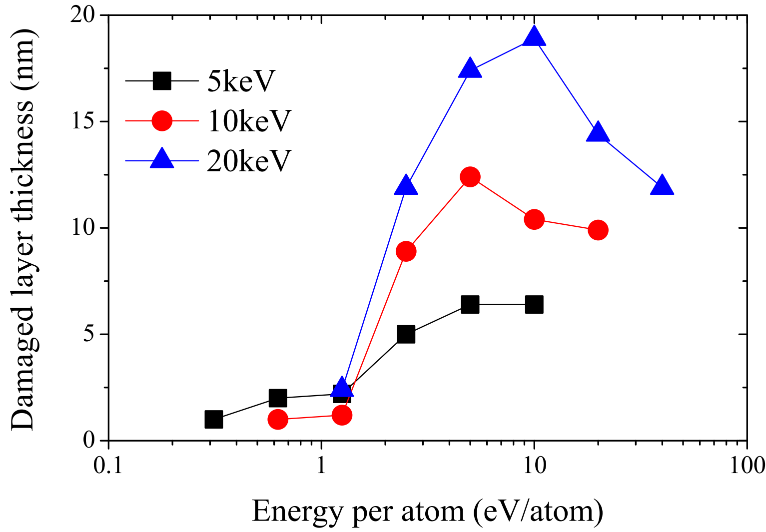

Figure 4.7: The effects of incident energy per atom on the damaged layer thickness on Si substrates for size-selected Ar GCIB with 5, 10, and 20keV

increased strongly between 1.2 and 2.5 eV/atom, regardless of the total incident energy. This result suggests that the threshold energy for atom displacement would be around 1 eV, although for atomic ions that value is 20 eV. In MD simulations, the threshold energy for displacement decreased with increasing incident cluster size and was around 1 eV for clusters larger than Ar_{1000}. The damaged layer thickness was almost proportional to the incident total energy.

Figure 4.8 represents the number of total displaced Si atoms with 20keV Ar cluster ion bombardment obtained experimentally and with MD simulation. The total number of displaced atoms was calculated from the thickness of amorphous layer and oxide layer and ion dose. In this calculation, the oxide layer was calculated as SiO_2 and the densities of the amorphous and silicon oxide layers were calculated as 2.33 and 2.2 g/cm^3, respectively.

MD simulations showed that the number of Si atoms displaced from their lattice sites increased with Ar cluster size, with a maximum around 2000 atoms/cluster, after which, a sudden decrease is observed with in-

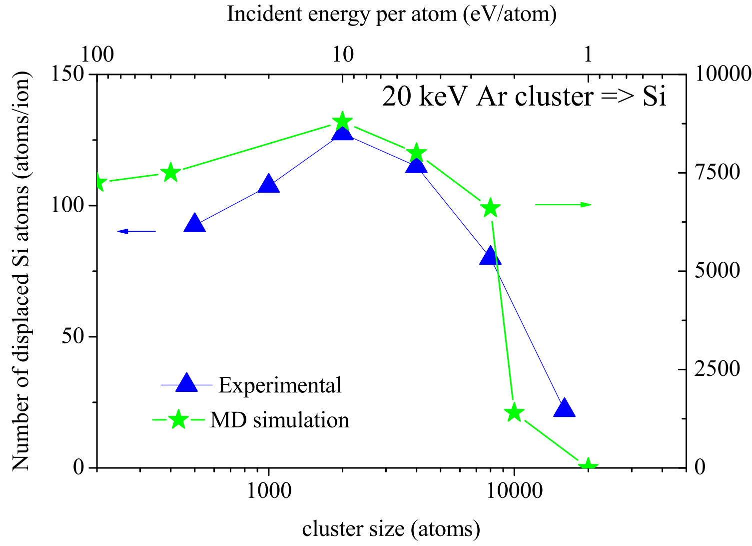

Figure 4.8: Number of total displacement atoms with 20 keV Ar cluster ion bombardment [27)]

creasing cluster size up to 8000 atoms/cluster. At a cluster size larger than 20000 atoms/cluster, no atom should be displaced. The same effect of cluster size on atom displacement was observed in experiment and MD simulation in both the small and the large cluster regions. The number of displaced atoms in MD simulation was about 50 times higher than in experimental results because surface atoms were affected more than once in this experiment. The affected area with 20 keV Ar GCIB was estimated to be 100 nm^2 in a previous report [65)], and therefore each surface atom was affected about 10 times at the dose of 10^{13} ions/cm^2(= 0.1 ions/nm^2). As mentioned in Ch. 2, if all affected ions would be displaced from the lattice, the true ratio between MD simulation and experiment would be about 5. As a result, the GCIB energy per atom should be less than 2 eV/atom in order to avoid the surface damage.

Figure 4.9 presents the number of Si atoms displaced and sputtering yield with 20 keV Ar GCIB. The threshold energy for displacement and sputtering was about the same, and both the sputtering and displacement yields increased with decreasing cluster size under large cluster ion bom-

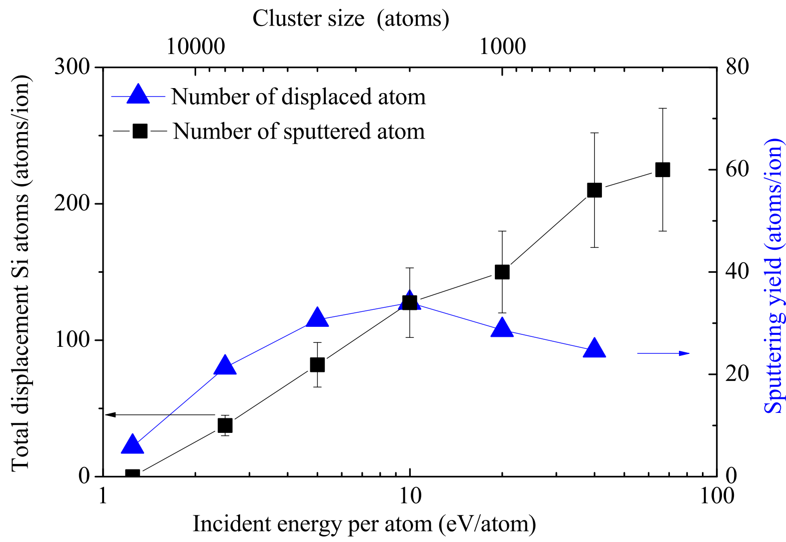

Figure 4.9: Number of total displaced atoms and sputtering yield with 20 keV Ar cluster ion bombardment

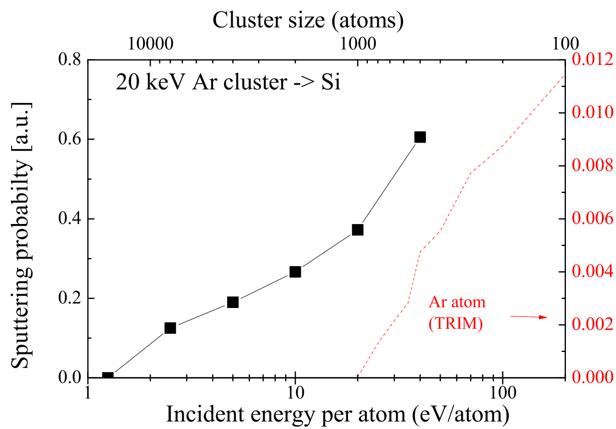

Figure 4.10: The sputtering probability of displaced Si with 20 keV Ar cluster ion bombardment

bardment. The sputtering yield continued to increase with decreasing incident cluster size under small cluster, although the displacement efficiency was saturated. The ratio of the number of sputtered atoms to that of displaced atoms under 20 keV GCIB of varying energy were shown in Fig.4.10. This value reflects the sputtering probability for a displaced atom. Red dotted line represents that of Ar atom calculated in TRIM. As shown, the sputtering probability decreased with increasing incident size. The energy of atoms displaced with cluster ions with high energy per atom would be higher than that of clusters with low energy-per-atom, and more particles would be ejected from the surface.

4.3 Surface damage-Organic materials

The surface damage with ion beam irradiation is a more serious problem in organic materials. Depth profiling with secondary ion mass spectrometry has become the most powerful interface analysis method for these nanostructures, and there is an increasing need for in-depth analysis with resolution of a few nanometer scale without damage to the underlying structure. However, as mentioned in the previous chapter, irradiation with atomic ions or small cluster ion beams at keV energies causes significant chemical damage accumulation on organic compound targets [66] because of the large energy transfer, deep penetration depth and low sputtering rate. Low energy (∼200 eV) reactive atomic ion beams, such as O^+ and Cs^+ have been used to avoid damage accumulation during irradiation [67, 68], but the sputtering rates of these beams are extremely low. GCIB has been reported to solve the problem of damage to biomolecules caused by incident ions [69, 70].

Figure 4.11 (a) presents the mass spectra of positively charged secondary ions emitted from a leucine ($C_6H_{13}NO_2$, 131 u) film with 8 keV Ar_{500}, which protonated leucine molecular ions and characteristic fragment ions were observed. Leucine films (about 4 μm-thick) were prepared on a Si substrate by evaporation. The secondary ion spectra of leucine films after Ar atomic ion and Ar cluster ion irradiation are shown in Figure 4.11 (b) and (c), respectively. The dose was 2×10^{15} ions/cm^2 and the etching depth was 400 nm and 1.7 μm, respectively. Large ions such as $m/z = 132$ and 86 were not observed after atomic ion bombardment because of damage accumulation. In contrast, the secondary ion spectra from before and after Ar cluster ion irradiation were completely similar. These results show that the leucine film was only a little damaged by Ar cluster ion irradiation despite its high sputtering yield. This indicates that large cluster ions can sputter leucine molecules with little damage, or that sputtering yields of large cluster ions are as large as the volume of damaged leucine molecules by irradiation.

To investigate the surface damage more precisely, we observed the secondary ions obtained with atomic primary ion irradiation in the energy range of MeV. When a MeV ion strikes a solid surface, it penetrates the

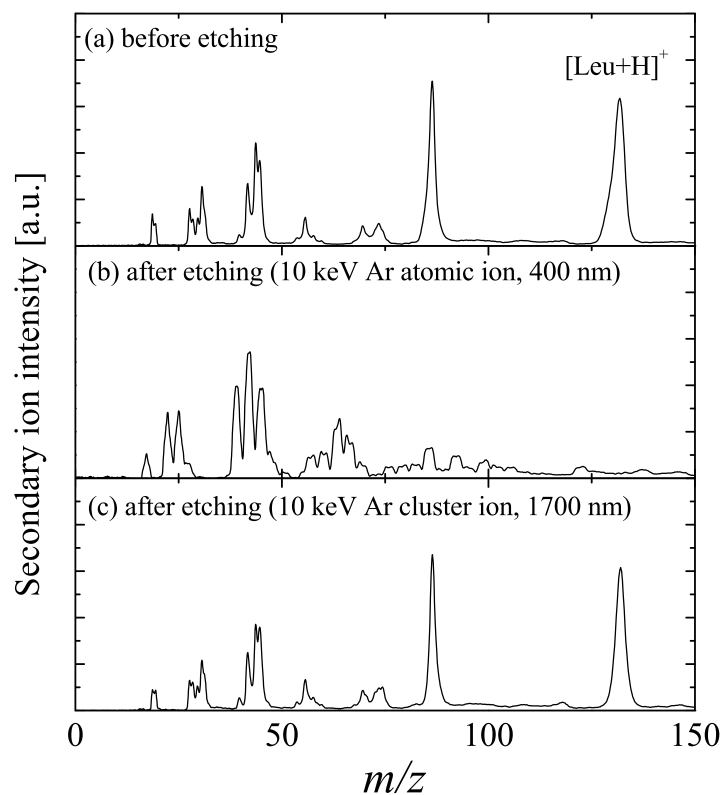

Figure 4.11: Secondary ion spectra of leucine (a) before, after 10 keV Ar (b) atomic ion and (c) cluster ion; the dose was 2×10^{15} ions/cm^2

surface and loses energy in a cylindrical region with intense ionizations and excitations due to direct Coulomb interactions, because the stopping power of a MeV ion is mostly due to the interaction with electrons in the target atoms. The high-energy electrons produce new generations of low-energy secondary electrons, and large molecules are ejected from the surface under action of these secondary electrons [71, 72]. Figure 4.12 (a) presents the mass spectra of positively charged secondary ions emitted from the Alq3 ($C_{27}H_{18}AlN_3O_3$, 459.4 u) film with 6 MeV Cu^{4+}. Before etching, Alq2 ($m/z = 315$) and Alq2+Al ($m/z = 342$) were observed with strong intensity. The mass spectra from Alq3 films irradiated with 10 keV Ar atomic ion and cluster ion are shown in Fig. 4.12 (b, c). The dose was 1×10^{15} ions/cm^2 and etching depth was 20 nm and 250 nm, respectively. After etching with atomic ions, no molecules were ejected from the Alq3 surface with 6 MeV Cu^{4+} bombardment, although the etching depth was only 20 nm. On the other hand, a perfectly unchanged spectrum was detected from the Alq3 surface etched with Ar cluster ions. Under irradiation with atomic and small cluster ion such as C_{60}, it has been difficult to sputter and analyze Alq3 continuously because the organic particles are sputtered selectively by energetic ion bombardment. In the case of Alq3, the target surface would be covered by the remaining Al after a few nm sputtering [73, 74]. However, we can offer a continuous analysis such as in-depth analysis by using GCIB, because no damage was accumulated on the surface after etching.

Figure 4.13 represents the $Alq2^+$ ion intensity from Alq3 thin films after etching with 10 keV Ar cluster and atomic ion bombardment. The $Alq2^+$ ion intensity did not decrease after etching with Ar cluster ion, but decreased drastically with increasing etching depth with Ar atomic ion, and only 20 % of initial intensity was detected after 1 nm etching. The calculated damaged cross-section with 10 keV Ar cluster ion was about 3×10^{-14} cm^2, i.e. one order of magnitude smaller than that with 10 keV Ar atomic ions.

To investigate the damage accumulation, secondary ion intensity of various organic films were measured by using the depth profiling technique. In this method, the surface is etched uniformly by Ar cluster ion beam irradiation between each SIMS measurement. We used arginine ($C_6H_{14}N_4O_2$,m

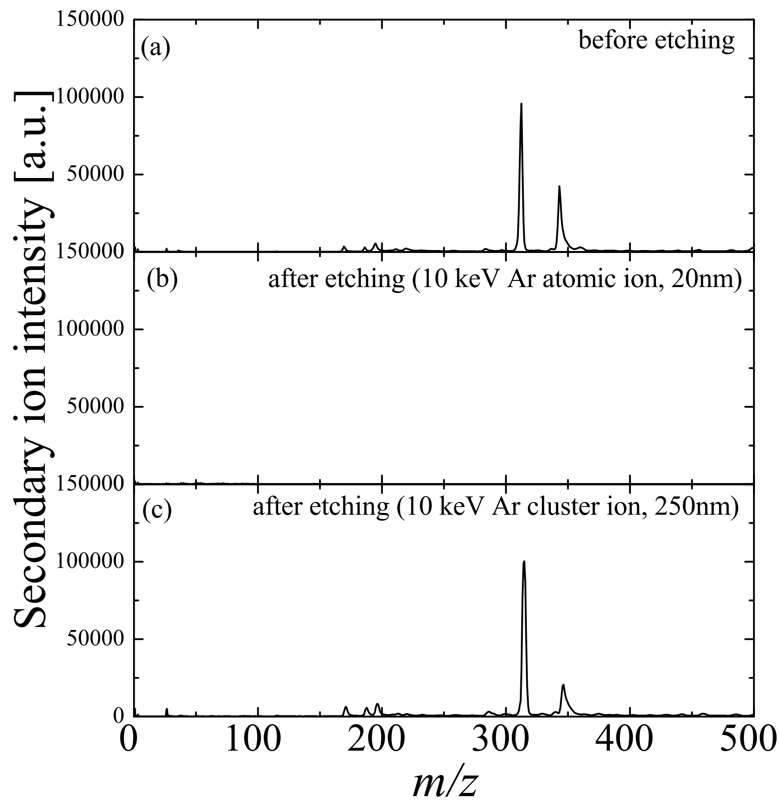

Figure 4.12: Secondary ion spectra of Alq3 (a) before, after bombardment with 10 keV Ar (b) atomic ion and (c) cluster ion; the dose was 1×10^{14} ions/cm^2

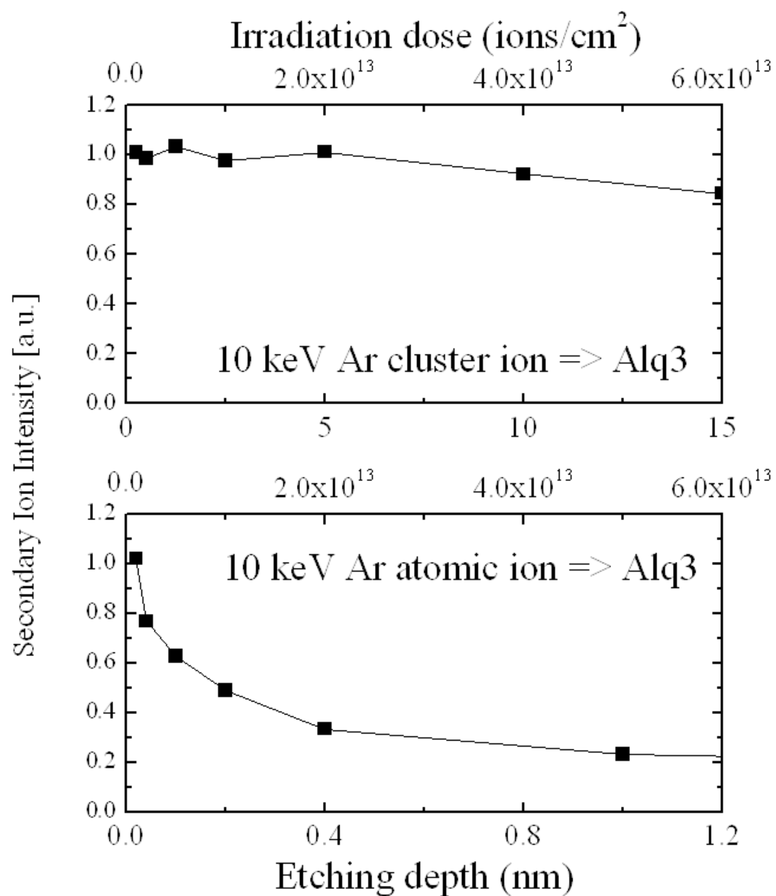

Figure 4.13: Secondary ion intensity of $Alq2^+$ with 10 keV Ar cluster and atomic ion.

= 174u), polycarbonate ($C_{16}H_{14}O_3$, PC, m = 254u) and C_{60} (m = 720u) in this study. The arginine film was the same as the sample in Ch. 3. PC and C_{60} were purchased from Nacalai Tesque Inc. (Kyoto, Japan) and Sigma Aldrich Inc. (St. Louis, MO, SA), respectively. The PC films were prepared by spin-casting and the C_{60} films were prepared by evaporation methods on Si substrate. The thickness of the arginine, PC and C_{60} films was 350, 70 and 50 nm, respectively. The targets were at ambient temperature.

Figure 4.14 presents the intensities of characteristic secondary ion from arginine(m/z = 175), PC(m/z = 135) and C_{60}(m/z = 720) as a function of etched film depth (lower horizontal axis) and Irradiation dose (upper horizontal axis). The secondary ion intensity was independent of the incident ion fluence until the film was etched completely, indicating that there was no surface accumulation and that the surface damage only depended on the incident cluster conditions. Figure 4.14 presents C1s and O1s X-ray photoelectron spectra (XPS) spectra of PMMA samples before and after Ar cluster ion beam irradiation. The molecular structure of PMMA was shown in Fig 3.16. The mean cluster size was 2000. The C1s peak can be deconvoluted into three components, and the O1s peak can be deconvoluted into two components. After etching with 20 keV Ar cluster ions, the C1s and O1s spectra changed and the peak intensity of O-C=O, C=O, C=O and C-O-C decreased slightly compared to the unirradiated PMMA sample. After etching with 5 and 10 keV Ar cluster ions, the locations and intensities of the C1s and O1s peaks alomost completely agreed with those of unirradiated PMMA sample [75]. This results agree with the results of SIMS spectra, shown in Ch. 3. Therefore, to avoid damage during irradiation the incident energy per atom should be lower than 5 eV/atom.

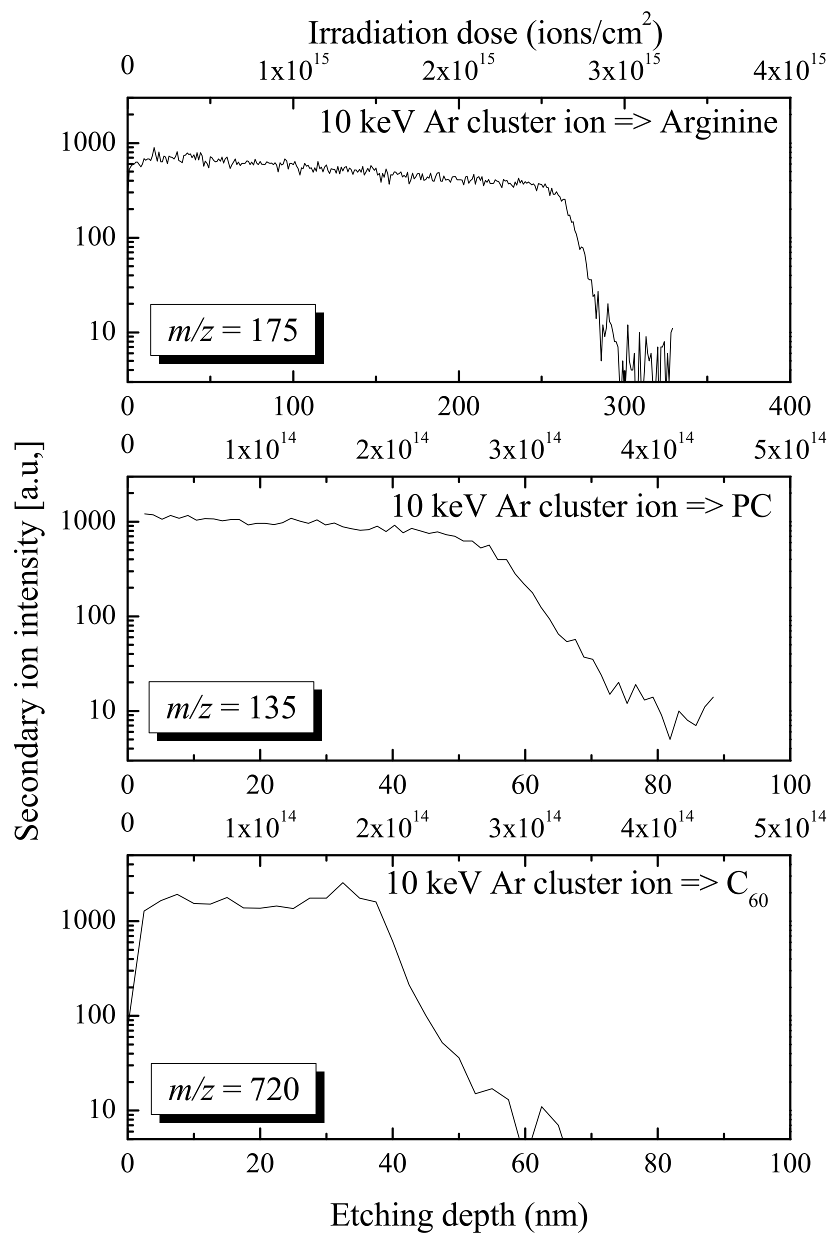

Figure 4.14: Secondary ion intensity of organic films after etching by 10 keV Ar cluster ion.

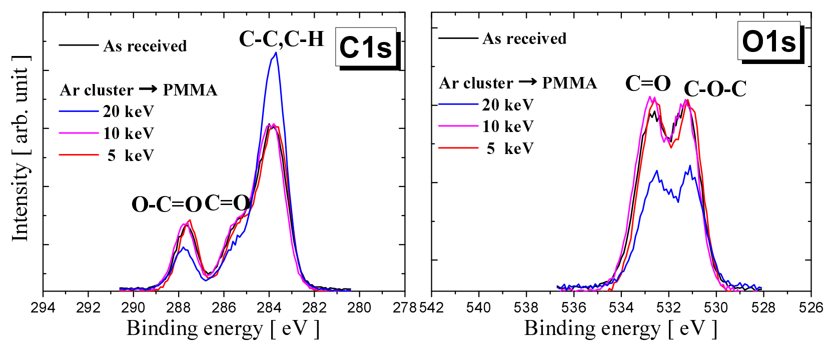

Figure 4.15: C1s and O1s XPS spectra of PMMA samples before and after irradiation with 5-20 keV Ar cluster ion.

Chapter 5

Surface morphology with GCIB

5.1 Surface smoothing with GCIB irradiation

When a large gas cluster ion bombards a surface, multiple collisions occur in the near surface region and a crater-like damage forms on the surface. Following the impact, surface atoms are displaced in a lateral direction along the surface, and some atoms are sputtered. As mentioned in Ch. 4, the volume of displaced atoms would be a few hundred nm^3 under 10 keV cluster ion bombardment. Therefore, surface grain structures are rapidly removed and the rough surface becomes smooth under GCIB irradiation [76, 77]. In conventional atomic ion bombardment, the ion beam penetrates the surface and causes a small hillock. To avoid roughening the surface, the ion beam energies need to be in the range of a few hundreds of eV. However, it is difficult to produce low-energy ion beams at high intensity because of their space-charge effects. On the other hand, with GCIB surface smoothing without any scratches has been reported for various inorganic targets such as Cu and CVD diamond [78]. Dry polishing and smoothing of hard or unreactive materials are feasible by using GCIB. Moreover, because of the low mass-to-charge ratio a large beam current can be produced. Therefore, GCIB has been proposed for surface smoothing applications [79, 80, 81]. Of course, the target surface would be different after fast or slow cluster ion irradiation,so that optimum condition has to be selected to apply GCIB most effectively. In this chapter, we discuss the incident cluster size and energy per atom effects on surface morphology for GCIB irradiation.

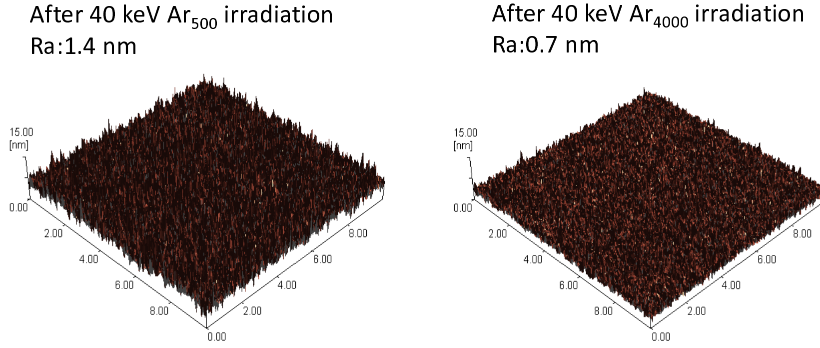

Figure 5.1: AFM images of a Si surface (a) after 40 keV Ar_{500} and (b) Ar_{4000} irradiation

5.2 Surface morphology-Si target

In this part of the study, crystalline Si (100) substrates were irradiated with Ar GCIB and the surface roughness was evaluated. The incident energy of the beam was in the range of 10-60 keV, and irradiation was carried out at normal incidence. The cluster size was from 1000 to 8000, and the ion dose was 5×10^{15} ions/cm^2. The apparatus and size-selection method were described in Ch. 2. To study the difference in surface irradiation effects caused by various cluster ions, the surface morphology of the Si target was observed ex situ with an atomic force microscope (AFM: Shimadzu, SPM-9500J2). The scan area of the AFM was 10 μm $\times$ 10 μm. Figure 5.1 shows AFM topography images of Si surface after 40 keV Ar_{500} and Ar_{4000} irradiation. The average roughness (Ra) of the Si surface before irradiation was about 0.11 nm. When the GCIB was irradiated onto Cu, the average roughness saturated at an etched depth above 30 nm in previous reports. The sputtering depth of the targets was about 300 nm after 40 keV Ar_{500} and 75 nm after 40 keV Ar_{4000} on Si, and therefore, uniform roughness should be obtained by cluster ion bombardment. After irradiation with 40keV Ar_{500} and Ar_{4000}, the average roughness of the Si surface was 1.4 and 0.7 nm, respectively.

In this study, the Si surface was roughened by Ar GCIB because the

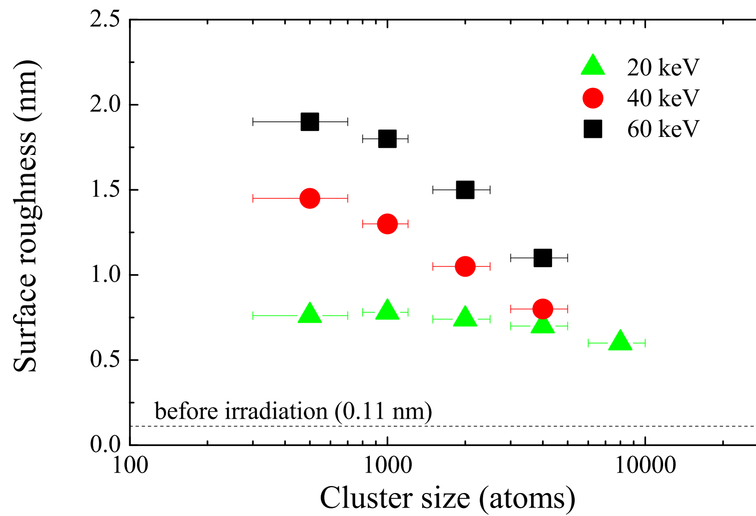

Figure 5.2: The effect of incident Ar cluster size on surface roughness

initial Si surface was atomically flat. The irradiated Si targets were also smooth, however after 40 keV Ar_{4000} the Si surface was clearly smoother than after Ar_{500} with the same total energy. Figure 5.2 shows the average surface roughness of Si after irradiation with 20, 40 and 60 keV Ar GCIB at varying size. All targets were sputtered at least 30 nm to obtain the uniform surface. The average roughness decreased monotonically with increasing incident cluster size under ion bombardment at the same total energy, and this is attributed to the decreasing incident energy per atom. The average roughness also decreased with decreasing total energy under the GCIB bombardment at the same cluster size. Both incident cluster size and energy per atom are thus important factors triggering irradiation effects of GCIB. However, as indicated in Ch. 4, the effect of energy per atom was found to be stronger than that of cluster size in many irradiation effects.

Figure 5.3 presents the effects of incident energy per atom on surface roughness. The surface roughness increased with increasing incident energy per atom. However, the Si surface was rougher after 60 keV Ar_{4000}

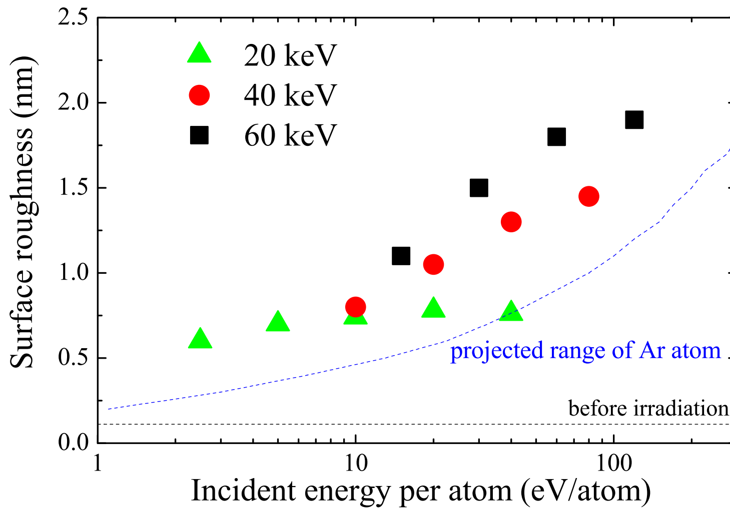

Figure 5.3: The effect of incident energy per atom on surface roughness for Ar cluster bombardment

(15eV/atom) than after 20 keV Ar_{500} (40 V/atom), although the incident energy per atom was less than half. Therefore, in regards with surface roughness, the irradiation effect does not depend mainly on incident energy per atom. The blue dotted line represents the projected range of Ar atoms calculated with TRIM. Surface roughness was a few times larger than the projection range of Ar atoms at the same velocity, but the effect of incident energy per atom on surface roughness seems to be weaker than that on projected range. As shown in Figs 2.11 and 5.2, the size affects sputtering yield and surface roughness with the a similar trend.

Figure 5.4 shows the correlation between surface roughness and the sputtering yield of Si with 20, 40 and 60 keV Ar cluster ion bombardment. They can be plotted on same curve independently of total incident energy. Under cluster ion bombardment, a crater-like shape forms on the surface because of the high-density energy deposition. The dependence of the crater dimensions on total incident energy was investigated in experiment and MD simulation, and has been previously reported [82, 83, 84]. The crater depth

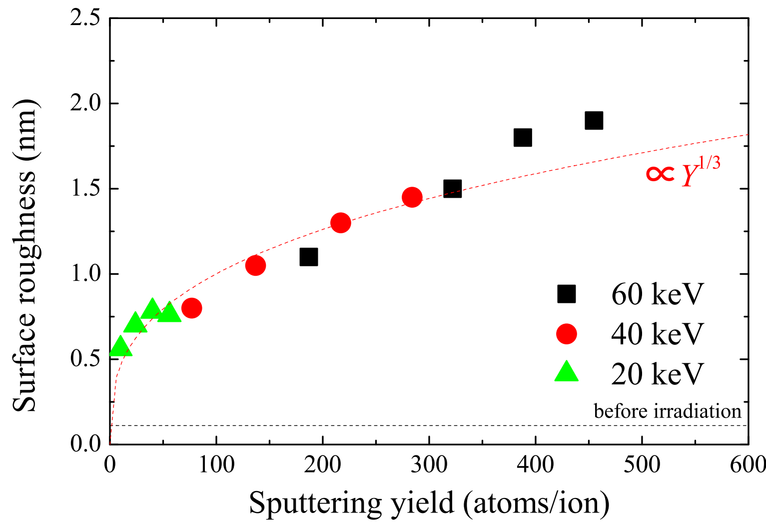

Figure 5.4: The effect of sputtering yield on surface roughness for Ar cluster bombardment

was found to be proportional to the cubic root of the total incident energy. The red dotted line presents the crater depth calculated from the Si sputtering yield and density (2.33 g/cm^3), and was in good agreement with the experimental data if the sputtering yield was lower than 300 atoms/ion. On the other hand, under high sputtering yield conditions, which includes 60 keV Ar_{500} and Ar_{1000}, the proportionality seems to be lost. The results under these conditions suggest that hemispherical craters were formed on the Si surface with GCIB, and the crater shape reflects the surface roughness. The crater shape remained unchanged for sputtering yield lower than 300 atoms/ion, and became vertically elongated with increasing sputtering yield above this value. In other words, this study indicates that small and fast cluster bombardment forms deep craters. The sputtering probability of fast clusters was higher than that of slow clusters, as mentioned in Ch. 4, and this means that the incident cluster conditions are reflected in the crater shape under small and fast cluster bombardment.

Figure 5.5 presents the correlations between surface roughness and sput-

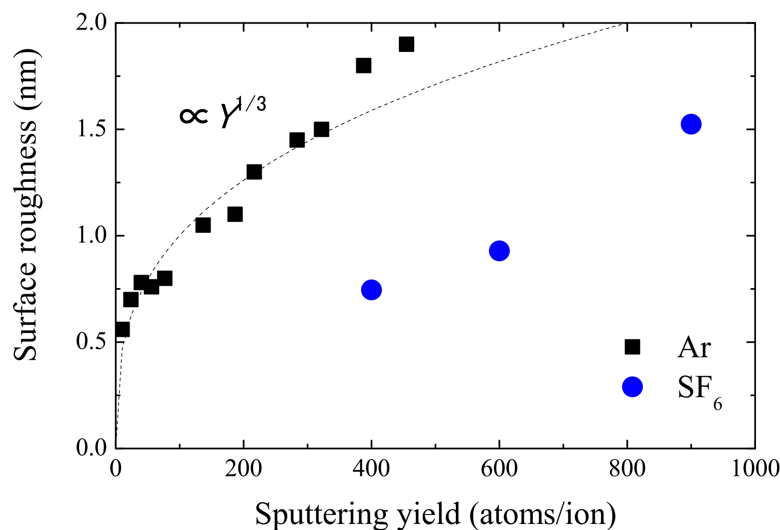

Figure 5.5: The effect of sputtering yield on surface roughness for Ar and SF_6 cluster bombardment

tering yield with Ar and SF_6 cluster ion bombardment. The energy of the SF_6 cluster was 20 keV, and the mean cluster sizes were 600, 1500 and 3000 molecules/ion. SF_6 cluster is a reactive cluster ion, and the Si sputtering yield with 20 keV SF_6 cluster was more than 10 times higher than that with 20 keV Ar cluster ion. The black and blue dots indicate the results for Ar and SF_6 cluster ions, respectively. The surface roughening processes with Ar cluster ion and SF_6 cluster ion were completely different. For example, Si surface roughness after irradiation with 20 keV $(SF_6)_{3000}$ and 60 keV Ar_{1000} was about 0.7 and 1.7 nm, although the Si sputtering yield was about the same (∼400 atoms/ion). For ion bombardment with the same velocity, after irradiation with 20 keV $(SF_6)_{600}$ (0.23 eV/u) and Ar_{2000} (0.25 eV/u) the surface roughness values were about 1.5 and 0.7nm, respectively. These results suggests that crater shapes obtained with Ar and SF_6 clusters is different.

Figure 5.6 presents a model of surface morphology with nonreactive and reactive cluster ion bombardment. Under nonreactive cluster ion bom-

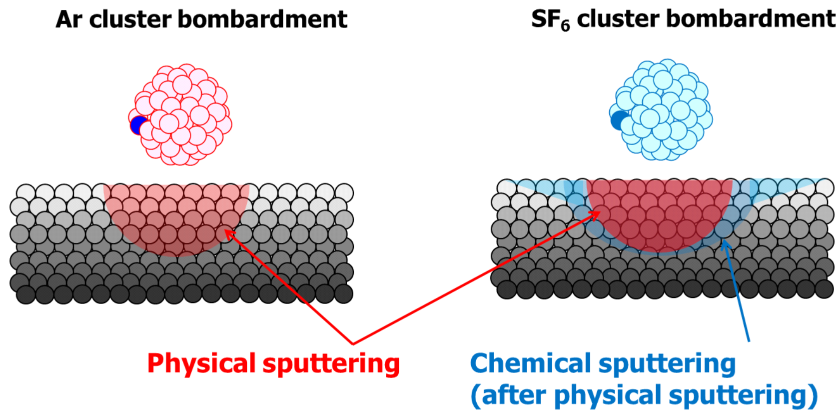

Figure 5.6: The model of sputtering for non-reactive(Ar) and reactive(SF_6) cluster bombardment

bardment, hemispherical crater damage has formed physically. The shape of this crater was roughly independent of incident cluster conditions, and the volume increased with increasing incident cluster size and energy per atom. The surface roughness after irradiation with nonreactive cluster ion was proportional to the crater depth, and therefore proportional to the cube root of the sputtering yield. Under reactive cluster ion bombardment, hemispherical crater damage is formed physically in the first stage. After the physical sputtering, the reactive constituent remains on the target surface and forms a chemical compound with the excited atoms. Finally, the chemical compound evaporates and leaves the surface. In MD simulation, the time scales of physical and chemical sputtering were reported to be a few ps and a few 10 ps, respectively [85)]. In the experiment, the diameter affected by a 20 keV Ar cluster was about 10 nm [86)]. Under such nonreactive bombardment, less than 1 % of affected atoms are sputtered. For instance, the volume of displaced atoms with 20 keV Ar_{1000} was 140 nm^3 per incident ion. Meanwhile, the volume of sputtered matteris of 0.7 nm^3, implying that the sputtering probability is only 0.5 %. The sputtered Si volume with 20 keV $(SF_6)_{3000}$ was 8 nm^3, which means no more than one layer of the surface craters (80 nm^2). Therefore, the actual crater depth

with nonreactive and reactive cluster ion impact was approximately the same, whereas the sputtering yield with reactive GCIB was one order of magnitude higher than with nonreactive GCIB.

5.3 Surface morphology-PMMA target

Analytical techniques for structural analysis of organic and polymeric materials have recently grown in importance, and there is an increasing need for in-depth analysis with resolution on the scale of a few nanometers without damage to the underlying structure. GCIB is expected to be the solution to the problem of sputtering without damage, and in fact, with GCIB a no-damage etching process has been realized, as mentioned earlier. The surface roughness is one of the most critical factors for analyzing multilayer thin films with high depth resolution, because depth resolution depends on surface roughness. For high resolution depth profiling, the sample surface must be maintained as smooth as possible after ion etching. The surface smoothing effect of GCIB could not be only applied for inorganic materials, but also for organic materials. Figure 5.7(a) presents the AFM image of the as-received leucine fil. The surface average roughness (Ra) was about 180nm. There were numerous large grains on the surface and the grain height was about 1 μm. The leucine surface after irradiation with Ar atomic ion at a dose of 2×10^{15} ions/cm^2 is shown in Fig. 5.7(b),and the surface roughness became 250 nm, which is rougher than before. Large grains still remained on the surface, and a small hillock was added. In contrast, after irradiation with Ar cluster ion at a dose of 2×10^{15} ion/cm^2, the surface roughness became 120 nm, and the grain size clearly decreased as can be seen in Fig. 5.7(c).

The surface damage and etching depth of the films with 10 keV Ar atomic and cluster ion irradiation are seen in Fig. 4.11. This result indicates that surface smoothing, low damage etching and fast etching could be achieved at the same time by using GCIB. In this section, we investigated the effect of cluster size and energy per atom on PMMA surface morphology under GCIB bombardment. The total energy of GCIB was in the range of 10-60 keV and irradiation was carried out at normal incidence. The cluster sizes varied within 1000 and 16000, and the ion dose was up to 1×10^{14} ions/cm^2. The irradiation equipment and size-selection method were described in Ch. 2. 100 nm-thick PMMA films were prepared by vapor deposition. Before irradiation, the average surface roughness of the

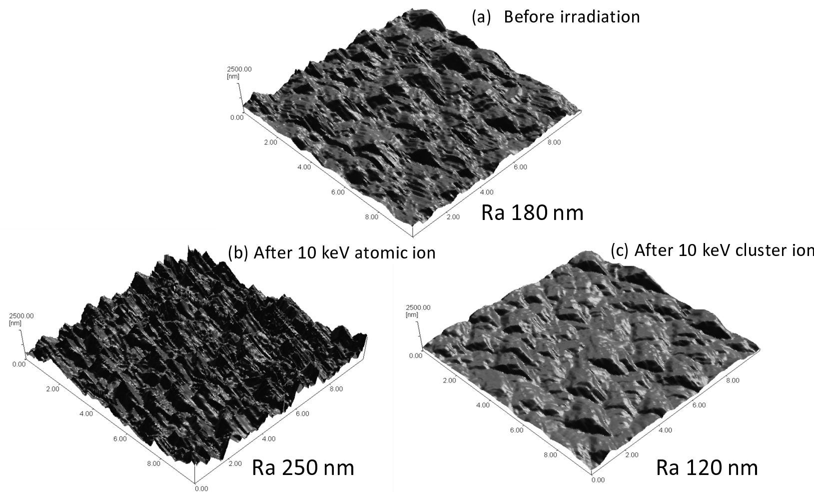

Figure 5.7: AFM images of the leucine films (a) before and after irradiation with at a dose of 2×10^{15} ions/cm^2 , 10 keV Ar (b) atomic ion and (c) cluster ion. (The scanned area is 10μm $\times$ 10 μm)

PMMA sample was about 0.22 nm.

Figure 5.8 presents AFM topography images of the PMMA samples after irradiation with 20 keV Ar_{1000} and Ar_{16000}. The etching depth of PMMA films was 60 and 40 nm, respectively. After irradiation with the two cluster sizes, Ar_{1000} and Ar_{16000}, the PMMA surface was roughened to 5.0 nm and 0.78 nm, respectively. Small grains were observed on both PMMA samples, but the grain with Ar_{1000} was higher than with Ar_{16000}.

Figure 5.9 shows the correlations between the surface roughness and sputtering depth of PMMA samples under cluster ion irradiation with 20keV for sizes Ar_{1000}, Ar_{4000} and Ar_{16000}. The surface roughness increased with increasing etching depth for each cluster ion, and saturated after 30nm sputtering. This result agrees with the report on Cu surface smoothing with Ar cluster ion.

Figure 5.10 shows the saturated surface roughness under 20 keV Ar cluster ion irradiation with size between Ar_{1000} and Ar_{16000}. All targets were sputtered at least 30 nm to saturate the surface roughness. The average roughness decreased monotonically with increasing incident cluster size.

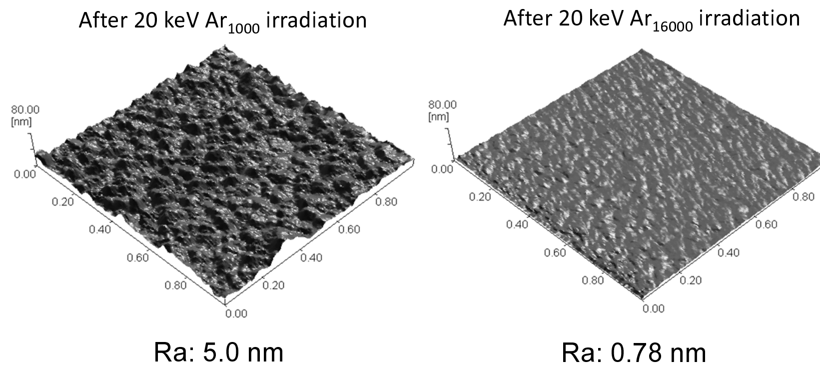

Figure 5.8: AFM images of the PMMA films after 20 keV GCIB irradiation with (a) Ar_{1000}, with the dose of 5 $\times$ 10^{13} ions/cm^2 ;(b) Ar_{16000}; with the dose of and 1 $\times$ 10^{14} ions/cm^2. (Scanned area is 1 μm $\times$ 1 μm)

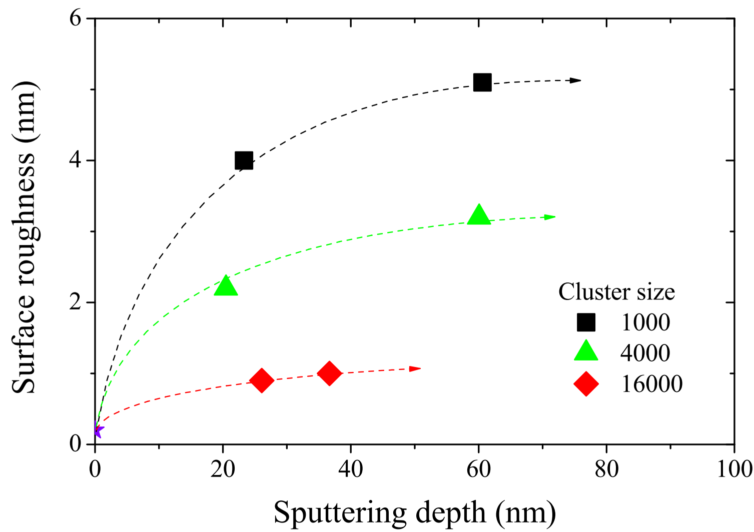

Figure 5.9: Surface roughness and sputtering depth of PMMA with 20 keV Ar cluster irradiation.

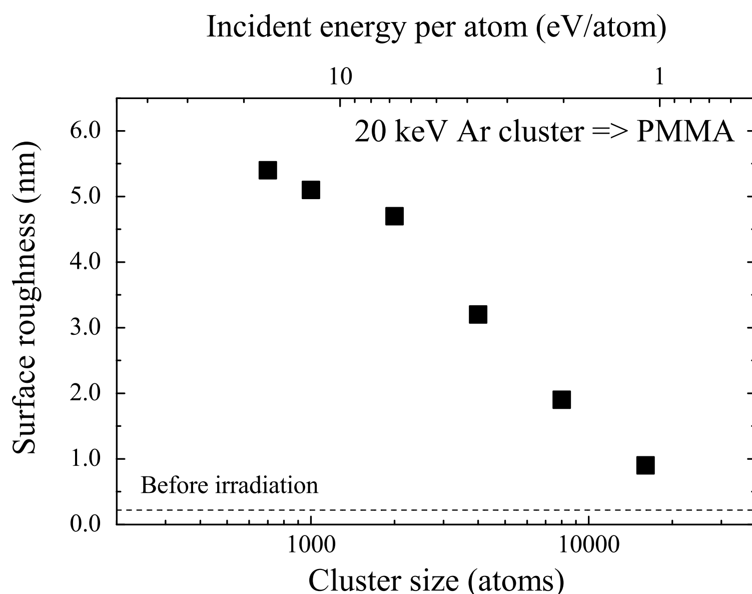

Figure 5.10: The effect of incident size on surface roughness

This result was similar to that obtained on Si targets, shown in Fig. 5.2, but the size effect on the PMMA surface was higher than on the Si surface. The ratio of Si surface roughness values after irradiation with 20keV Ar_{8000} and Ar_{1000} was about 0.7, whereas, the ratio of PMMA surface roughness values after irradiation of 20 keV Ar_{8000} and Ar_{1000} was only 0.3, suggesting that PMMA surface roughening during sputtering can be decreased drastically by using large clusters, which are thus more effective for the organic targets.

Figure 5.11 shows the correlation between the PMMA surface roughness values and sputtering yield in the range of 5-30 keV Ar GCIB. At the same total energy, surface roughness increased with increasing sputtering yield. However, the values cannot be fitted on the same graph with Si. Surface roughness after cluster ion irradiation was found to depend on the crater shape, which crater shape is strongly dependent on incident cluster size and energy per atom. The black dots in Fig. 5.12 represent the ef-

fect of incident energy per atom on surface roughness for Ar_{2000}, and the energy per atom is shown on the top horizontal axis. Surface roughness increased linearly with increasing incident energy per atom. On the other hand, the red circles in Figure 5.12 represent the effect of cluster size on surface roughness for Ar cluster ion bombardment with 5 eV/atom, and cluster size is presented on the bottom horizontal axis. Surface roughness increased with 5 eV/atom small Ar cluster bombardment, and was weakly dependent on incident cluster size under large cluster ion bombardment. These results indicate that for an organic target the crater depth strongly depends on the incident energy per atom. This result differs from that of Si, and is attributed to the difference in sputtering yield. In the case of Si, the sputtering probability was less than 1 %, and therefore the crater shape was independent of incident cluster conditions. In the case of PMMA, the sputtering probability was at least 20 %, and therefore GCIB with high energy per atom forms a deeper crater. The ion range in PMMA of an Ar atom with 12.5 eV energy as calculated by TRIM was less than 1 nm, at which sputtering does not occur because the binding energy between PMMA units is of the order of a few eVs. Compared with atomic ion bombardment with the same energy per atom, both the penetration depth and crater diameter would increase with incident cluster size under cluster ion bombardment because of the multiple collisions occurring on the surface. The crater radius and depth with 10 keV Ar_{800} bombardment were estimated to be about 2.5 and 2.9 nm from the sputtering rate and surface roughness, respectively. The penetration depth was more than twice that observed with atomic ion bombardment and the crater shape was hemispherical. The calculated radius for Ar_{800} was about 2.0 nm. This crater was bigger than the cluster, but shallower than the cluster diameter, suggesting that under 10 keV Ar_{800} bombardment a part of the cluster constituent atoms penetrate the PMMA surface, and therefore both sputtering volume and crater depth increased as cluster size increased under small-cluster GCIB. On the other hand, the crater radius and depth with 60 keV Ar_{4800} bombardment were estimated to be about 6.8 and 6.2 nm. In this case, the crater radius was larger than the crater depth.

Open circles in Figure 5.13 present the cubic root of the PMMA sput-

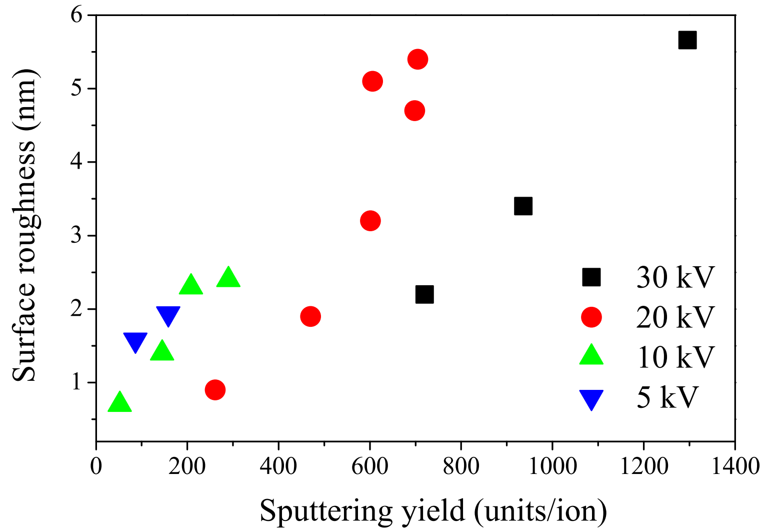

Figure 5.11: Correlations between sputtering yield and surface roughness for Ar cluster bombardment

tering yield with Ar GCIB. As shown, the surface roughness was in good agreement with the cubic root of the sputtering yield for sizes below Ar_{2400}, indicating that the crater shape with small cluster ion bombardment was similar. However, surface roughness does not increase rapidly with GCIB above Ar_{3200}. Under large cluster ion bombardment, the crater shape was wider than that with small cluster ion at constant energy per atom. As reported from MD simulation, the crater depth with large cluster bombardment obeyed the power law of total cluster energy and the power index was about 1/3 for constant cluster size. In addition, the crater depth decreased with increasing incident cluster size under the same-energy cluster ion.

Three models of the PMMA surface after Ar cluster ion bombardment are shown in Figure 5.14. The parameters r and d represent the crater radius and depth, respectively. The ratio of d/r was similar in the size range of 800-2400. In contrast, for Ar_{4800} it would be smaller than with Ar_{2400}, suggesting that the effect of incident cluster size on crater depth was low with large clusters, and that surface roughness strongly depends on the

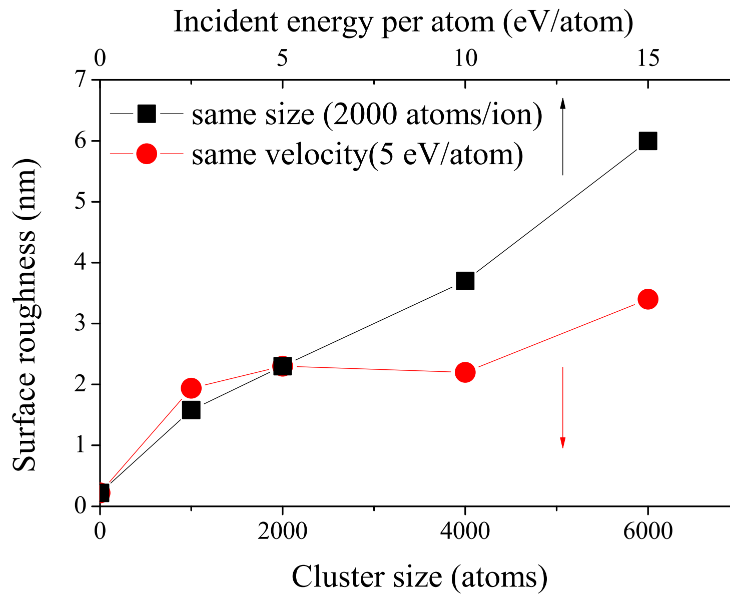

Figure 5.12: The effect of Ar cluster size and energy per atom on surface roughness

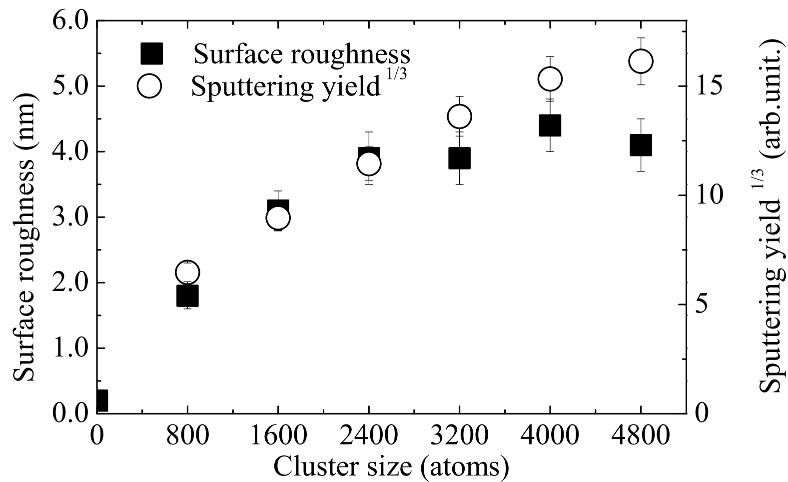

Figure 5.13: The effect of acceleration voltage on surface roughness for Ar cluster ion.

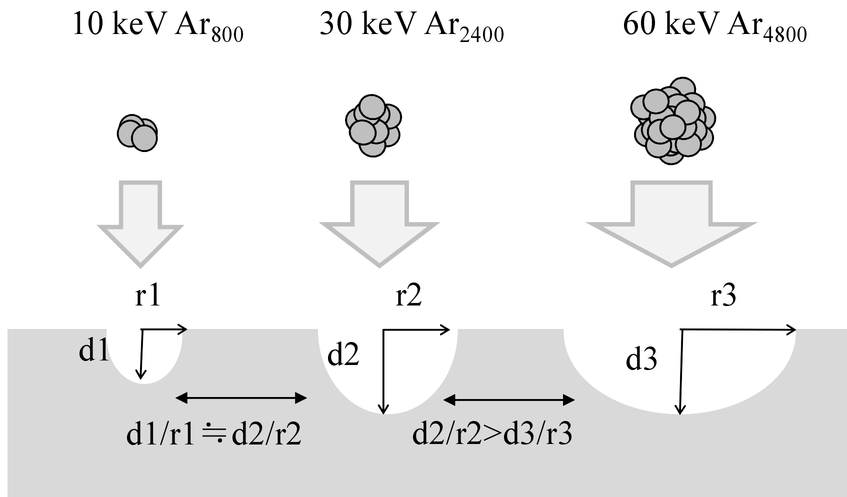

Figure 5.14: Models of the PMMA surface after 12.5 eV/atom Ar cluster ion bombardment. The crater shape with Ar_{800} and Ar_{2400} was similar. the crater shape with Ar_{4800} had a wider opening than that with Ar_{2400}.

crater depth. Therefore, the PMMA surface roughness after irradiation with 60 keV Ar_{4800} was about same as with 30 keV Ar_{2400}. The results indicated that high sputtering yield without important roughening of the surface is possible with large cluster ions.

Chapter 6

Summary and conclusions

In this study, we have explored the effects of cluster size and energy per constituent on cluster interactions with the surface of Si and organic targets. GCIB has various unique irradiation effects, and it is necessary to understand the surface physics for its effective use in various applications. To evaluate the optimum cluster conditions, the phenomena of sputtering, secondary ion emission, surface damaging and surface morphology were investigated under impact of Argon GCIB at various conditions.

In the case of Si, the thickness of the damaged layer increased proportionally to the total incident energy, while the sputtering and secondary ion yields increased nonlinearly and faster than damage amount. These results showed that the incident energy was efficiently transferred from the GCIB to the solid surface, probably due a thermal spike occuring under cluster bombardment. With decreasing incident energy per atom, both the damaged layer thickness and sputtering yield decreased. The threshold energy per atom for apparition of a damaged layer and for sputtering was about 1 and a few eV/atom respectively. These values are much lower than that with atomic ions. We assume that this is the result of multiple collisions between the cluster ion's constituent atoms and surface atoms. On the other hand, the threshold energy of incident cluster ion for Si^+ emission was found to be about 8 eV/atom because a certain kinetic energy is necessary for the emitted particles to be ionized. It has also been found that hemispherical craters are formed by gas cluster ion bombardment, by surface roughness after cluster irradiation which unveiled topography build-up whose features dimentions were similar to the calculated crater radius.

Under Ar GCIB bombardment of Si targets, Si secondary ion cluster such as Si_2^+ and Si_3^+ were measured with high intensity. For example, 95 % of the total Si secondary ion counts obtained under 40 keV Ar_{1100}^+ irradiation were from Si cluster ions. The intensity ratio of the Si clusters decreased with increasing incident energy per atom. This result is in good agreement with Si emission with laser ablation and suggests that the Si cluster ions are emitted directly as clusters from the surface. Sputtering yield and secondary ion yield are enhanced by cluster ion bombardment. Si sputtering yield with 60 keV Ar_{300}^+ was about 2 atoms/ constituent atom, which is about 10 times higher than with 0.2 keV Ar. This enhancement is as large as that with C_{60} bombardment. This indicate that the enhancement of Si sputtering yield with cluster ion bombardment is saturated at about 10.

In the case of organic targets, sputtering yield and secondary ion intensity did not decrease with increasing dose after GCIB irradiation, but they decreased rapidly under atomic ion beam. It indicates that damage accumulation did not occur with Ar GCIB. Indeed the organic surface was not damaged by GCIB irradiation when the incident energy per atom was less than 5 eV/atom because it is much easier to break the van der Waals bonding between Ar atoms ($\leq$ 0.1 eV) than the bonding in molecules such as C-C and C-O ($\geq$ 2 eV). The surface roughness of irradiated organic materials was thus strongly dependent on incident energy per atom and weakly dependent on incident cluster size. On the other hand, the sputtering yield was proportional to the incident cluster size. Therefore, fast etching without damaging and roughening are feasible with GCIB with low energy per atom and large size.

Chapter 7

Appendix

7.1 Energy loss during transportation

Energy loss during transportation is one of the serious problems with gas cluster ion beam irradiation. The collision frequency of gas cluster ion beams with residual gas during transportation is two orders of magnitude higher than that of an atomic ion beam [87] because a gas cluster is an aggregate of thousands of atoms.

In atomic ion beam irradiation, the collision with residual gas is elastic, and incident velocity decreases. In gas cluster ion beam irradiation, the total energy of the cluster ion decreases after collision, but the incident velocity does not decrease [88], indicating that the energy loss of cluster is mainly the result of the scattering of constituent atoms. The constituent atoms in the cluster are bound by van der Waals attraction, which is much lower than the acceleration energy of the cluster ion, and thus cluster easily collapse in collision with residual gas. Thus, it is necessary to reduce the chamber pressure in cluster ion beam irradiation. However, the chamber pressure would increase with an increase in incident cluster beam intensity because almost all incident ions turn to residual gas after bombardment.

For example, under 1 mA of Ar_{1000} irradiation evacuated with a 4000liter/sec pump, chamber pressure is about 6×10^{-3} Pa. It is difficult to achieve high current intensity and good chamber pressure. It is important to study the effect of chamber pressure for irradiation efficiency and determine the pressure range under cluster ion irradiation. In this study, we investigated the effect of varying incident energy and chamber pressure on the sputtering

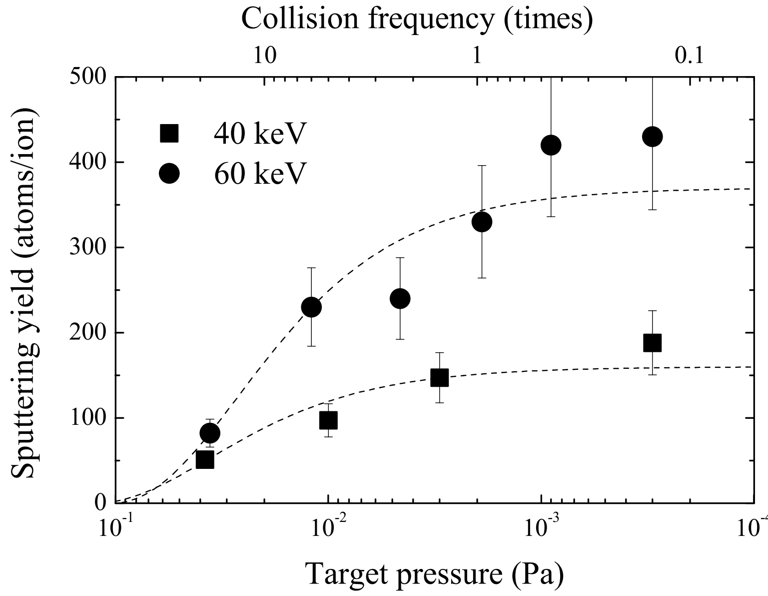

Figure 7.1: The effect of target pressure on Si sputtering yield with 40 and 60 keV Ar cluster ion beam

yield obtained with large gas cluster ion beam.

Figure 7.1 shows the effect of varying target pressure on Si sputtering yield with 40 and 60 keV Ar cluster ion bombardment. Mean cluster size was about 2000 atoms. The lower horizontal axis represents the pressure in the target chamber and the upper horizontal axis represents the calculated frequency of collisions between the cluster ion and residual gas in the target chamber. The collision frequency (n_c) was calculated by dividing flight length (L) by the mean free path of the cluster ion (L_c). The mean free path was calculated from the cross-section and the density of residual gas (ρ). The density of residual gas was proportional to chamber pressure. The radius of the cluster ion was proportional to the 1/3 power of size (N). Collision frequency was calculated with the following formula [87]:

$$n_c = \frac{L}{L_c} = Lr^2 \left(1 + N^{1/3}\right)^2 \rho \tag{7.1}$$

where r is the radius of the Ar atom. In this experiment, L was 120

mm and r was calculated as 0.19 nm. If the target chamber pressure was 2 $\times$ 10^{-3} Pa, the expected collision frequency would be about 1. In collisions with residual gas, some atoms in the cluster scatter and the total energy of the cluster ion decreases. Then, the sputtering yield after collision (Y_c) can be shown as follows:

$$Y_c(E) = Y(k^n E) \tag{7.2}$$

where $Y(E)$ is calcluted by the equation (2.4) and k is the ratio of cluster energy before and after the collision. Dotted line in Figure 7.1 represents the calculated $Y_c(E)$ from the equation (7.2). For 40 and 60 keV ion bombardment, the k were 0.95 $\pm$ 0.01 and 0.96 $\pm$ 0.01, respectively. The cluster ion size decreased about 5% of the whole size at 1 collision, and these results agreed well with the previous study [88]. This indicates that the sputtering yield with scattered atoms was nil or very low. After 10 collisions, the primary ion energy became about 2/3 and the sputtering yield decreased to about 1/2. To use gas cluster ion beams efficiently, the number of collisions between the incident cluster ion and residual gas should be kept to less than a few times. For example, chamber pressure has to better than a few 10^{-4} Pa if the flight length in the process chamber is about 100 mm.

List of Figures

1.1 The size and structure of typical clusters 3
1.2 Schematic representation of gas cluster formation and ionization 4
1.3 GCIB applications for nano-processing 7
1.4 Size distribution of Ar cluster ion beam 8

2.1 Irradiation effect with (a)atomic and (b)cluster bombardment 13
2.2 MD simulation of atomic bombardment and cluster bombardment into diamond with 2 keV/atom incident energy [19] 15
2.3 MD simulation of Si sputtering with 20 keV Ar_{2000} and Ar_{10000} [22] 17
2.4 Photograph of GCIB irradiation equipment 18
2.5 The experimental setup for size-selected GCIB irradiation . 19
2.6 Photograph of the ionizer 20
2.7 Schematic diagram of cluster size selection with the TOF method 20
2.8 Cluster size distributions of the unselected and size-selected Ar cluster ions 21
2.9 The surface profile of Si measured with an interferometric surface profiler after irradiation with 20 keV unselected Ar GCIB with mean size of 2000 atoms/cluster at the fluence of 3×10^{13} ions 24
2.10 Variation of sputtered volume of Si with irradiation dose for 20 keV Ar cluster ions 24
2.11 Si sputtering yield with varying incident cluster size for 20, 40 and 60 keV Ar cluster ions 25
2.12 The sputtering yields of Si with 20-60 keV Ar cluster ion . . 26

2.13 Si sputtering yield with cluster ion bombardment at low energy per atom . . . 27
2.14 Si sputtering threshold energy with varying cluster size . . . 28
2.15 Si sputtering yield with varying incident energy cluster ions 28
2.16 The nonlinear effects of Si sputtering with Ar GCIB irradiation 29
2.17 The nonlinear effects of sputtering with varying cluster ion bombardment . . . 30
2.18 Model of Si sputtering yield with Ar cluster ion . . . 32
2.19 Variation in sputtered depth of PMMA with irradiation dose for 5.5 keV Ar cluster and atomic ions . . . 33
2.20 Surface profile image of PMMA irradiated with 10 keV Ar cluster ion . . . 34
2.21 Variation in PMMA sputtering yield with incident Ar cluster size for 20 keV Ar cluster ions . . . 35
2.22 Variation in PMMA sputtering yield with varying incident Ar cluster energy-per-atom for 5-30 keV Ar cluster ions. . . . 36
2.23 Variation in PMMA sputtering yield with varying energy per atom for Ar_{1000} and Ar_{4000} clusters. . . . 37

3.1 Secondary ion spectra of Si obtained with cluster and Ar atomic ions at 20 keV [47] . . . 41
3.2 The experimental setup for size-selected SIMS . . . 43
3.3 Schematic diagram of the size-selected SIMS . . . 43
3.4 The secondary ion deflector . . . 44
3.5 Size distribution of Ar cluster ion beam with total energy of 40 keV . . . 45
3.6 Schematic diagram of the electronic components used in this TOF-SIMS . . . 45
3.7 Secondary ion spectra of Si with various sizes of 40 keV Ar cluster ions . . . 47
3.8 Secondary Si_n^+/Si^+ intensity ratio with Ar cluster ion bombardment at 40 keV . . . 48
3.9 Effects of incident size and energy-per-atom on secondary cluster ion intensity . . . 49

3.10 The effect of incident energy per atom on the intensity ratio Si_3^+/Si^+ . . . 50
3.11 Models of secondary cluster particle emission . . . 52
3.12 The effect of deposited energy density on the intensity of Si_3^+/Si^+ (V_a is 'acceleration energy') . . . 53
3.13 Si^+ intensity with various sizes of 40 keV Ar cluster ion . . . 54
3.14 Variation of Si and Si^+ yield with incident energy per atom and cluster size for size-selected 20 and 60 keV Ar cluster ion beams. . . . 55
3.15 Secondary ion spectra of leucine obtained with 8 keV Ar cluster and atomic ion bombardment . . . 58
3.16 Schematic diagrams of the molecular structures of the organic targets . . . 59
3.17 Secondary ion spectra of arginine with 11 keV Ar cluster ion bombardment . . . 61
3.18 Secondary ion spectra of phenylalanine with 11 keV Ar cluster ion bombardment . . . 62
3.19 Secondary ion intensity ratio between the characteristic fragment ion and the protonated molecular ion . . . 63
3.20 Secondary ion spectra of PMMA with 8 keV Ar cluster and atomic ion bombardment . . . 65
3.21 Secondary ion spectra of Alq3 with 13 keV Ar cluster and atomic ion bombardment . . . 67

4.1 XRR spectra of the Si surface before and after O_2 ion beam irradiation the dose of 1×10^{16} ioss/cm^2. . . . 70
4.2 XRR and simulated spectra of the Si target after oxidation obtained with 20 keV GCIB irradiation at a dose of 1×10^{16} ions/cm^2 (a) Ar cluster ion (size 2000) in O_2 atmosphere at 6.5×10^{-3} Pa; (b) 20 keV O_2 cluster ion. . . . 72
4.3 Secondary ion spectra of the Si target after oxidation obtained under irradiation with (a)20 keV Ar cluster ion irradiation in O_2 atmosphere at 6.5×10^{-3} Pa, and (b) 15 keV O_2 cluster ion. . . . 73

4.4 The SiO^+ intensities as a function of oxygen partial pressure during Ar cluster ion irradiation 74
4.5 Ψ and Δ plots of Si substrates by ellipsometry measurements after unselected and size-selected 10 keV Ar cluster ion beam irradiation with fluence of 1×10^{13} ions/cm^2 76
4.6 The effect of incident cluster size on the thickness of oxide(SiO_x) and amorphous(aSi) layer on Si substrates by 10 keV Ar GCIB 77
4.7 The effects of incident energy per atom on the damaged layer thickness on Si substrates for size-selected Ar GCIB with 5, 10, and 20keV 78
4.8 Number of total displacement atoms with 20 keV Ar cluster ion bombardment [27)] 79
4.9 Number of total displaced atoms and sputtering yield with 20 keV Ar cluster ion bombardment 80
4.10 The sputtering probability of displaced Si with 20 keV Ar cluster ion bombardment 80
4.11 Secondary ion spectra of leucine (a) before, after 10 keV Ar (b) atomic ion and (c) cluster ion; the dose was 2×10^{15} ions/cm^2 83
4.12 Secondary ion spectra of Alq3 (a) before, after bombardment with 10 keV Ar (b) atomic ion and (c) cluster ion; the dose was 1×10^{14} ions/cm^2 85
4.13 Secondary ion intensity of $Alq2^+$ with 10 keV Ar cluster and atomic ion. 86
4.14 Secondary ion intensity of organic films after etching by 10 keV Ar cluster ion. 88
4.15 C1s and O1s XPS spectra of PMMA samples before and after irradiation with 5-20 keV Ar cluster ion. 89

5.1 AFM images of a Si surface (a) after 40 keV Ar_{500} and (b) Ar_{4000} irradiation 92
5.2 The effect of incident Ar cluster size on surface roughness . 93
5.3 The effect of incident energy per atom on surface roughness for Ar cluster bombardment 94

5.4 The effect of sputtering yield on surface roughness for Ar cluster bombardment 95

5.5 The effect of sputtering yield on surface roughness for Ar and SF_6 cluster bombardment 96

5.6 The model of sputtering for non-reactive(Ar) and reactive(SF_6) cluster bombardment 97

5.7 AFM images of the leucine films (a) before and after irradiation with at a dose of 2×10^{15} ions/cm^2 , 10 keV Ar (b) atomic ion and (c) cluster ion. (The scanned area is 10μm $\times$ 10 μm) 100

5.8 AFM images of the PMMA films after 20 keV GCIB irradiation with (a) Ar_{1000}, with the dose of 5×10^{13} ions/cm^2 ;(b) Ar_{16000}; with the dose of and 1×10^{14} ions/cm^2. (Scanned area is 1 μm $\times$ 1 μm) 101

5.9 Surface roughness and sputtering depth of PMMA with 20 keV Ar cluster irradiation. 101

5.10 The effect of incident size on surface roughness 102

5.11 Correlations between sputtering yield and surface roughness for Ar cluster bombardment 104

5.12 The effect of Ar cluster size and energy per atom on surface roughness 105

5.13 The effect of acceleration voltage on surface roughness for Ar cluster ion. 105

5.14 Models of the PMMA surface after 12.5 eV/atom Ar cluster ion bombardment. The crater shape with Ar_{800} and Ar_{2400} was similar. the crater shape with Ar_{4800} had a wider opening than that with Ar_{2400}. 106

7.1 The effect of target pressure on Si sputtering yield with 40 and 60 keV Ar cluster ion beam 110

References

[1] R. Busani, M. Folkers and O. Cheshnovsky, Physical review letters **81** (1998) 3836–3839.

[2] H. Andersen and H. Bay, Journal of Applied Physics **45** (1974) 953.

[3] T. Fujimoto, T. Mizota, H. Nonaka, A. Kurokawa and S. Ichimura, Surface and interface analysis **37** (2005) 164–166.

[4] M. Tomita *et al.*, Applied physics letters **89** (2006) 053123.

[5] H. Kroto, J. Heath, S. O'Brien, R. Curl and R. Smalley, Nature **318** (1985) 162–163.

[6] W. Krätschmer, L. Lamb, K. Fostiropoulos and D. Huffman, Nature **347** (1990) 354–358.

[7] I. Yamada, J. Matsuo, N. Toyoda and A. Kirkpatrick, Materials Science and Engineering: R: Reports **34** (2001) 231–295.

[8] N. Toyoda, Y. Fujiwara and I. Yamada, Nuclear Instruments and Methods in Physics Research Section B: Beam Interactions with Materials and Atoms **206** (2003) 875–879.

[9] T. Seki and J. Matsuo, Nuclear Instruments and Methods in Physics Research Section B: Beam Interactions with Materials and Atoms **257** (2007) 666–669.

[10] A. Yoshida, M. Deguchi, M. Kitabatake, T. Hirao, J. Matsuo, N. Toyoda and I. Yamada, Nuclear Instruments and Methods in Physics Research Section B: Beam Interactions with Materials and Atoms **112** (1996) 248 – 251.

[11] R. MacCrimmon, J. Hautala, M. Gwinn and S. Sherman, Nuclear Instruments and Methods in Physics Research Section B: Beam Interactions with Materials and Atoms **242** (2006) 427–430.

[12] J. F. Ziegler, J. P. Biersack and U. Littmark, *The stopping and range of ions in solids* (Pergamon Press, ADDRESS, 1985).

[13] P. Sigmund, Physical review **184** (1969) 383–416.

[14] H. H. Andersen and H. L. Bay, Journal of Applied Physics **46** (1975) 2416–2422.

[15] S. Bouneau, A. Brunelle, S. Della-Negra, J. Depauw, D. Jacquet, Y. Le Beyec, M. Pautrat, M. Fallavier, J. C. Poizat and H. H. Andersen, Phys. Rev. B **65** (2002) 144106.

[16] P. Sigmund and C. Claussen, Journal of Applied Physics **52** (1981) 990–993.

[17] M. H. Shapiro and T. A. Tombrello, Phys. Rev. Lett. **65** (1990) 92–95.

[18] V. Shulga and P. Sigmund, Nuclear Instruments and Methods in Physics Research Section B: Beam Interactions with Materials and Atoms **47** (1990) 236 – 242.

[19] T. Aoki, Tand Seki, J. Matsuo, Z. Insepov and I. Yamada, Mat. Res. Soc. Symp. Proc **504** (1998) 81.

[20] H. H. Andersen, A. Brunelle, S. Della-Negra, J. Depauw, D. Jacquet, Y. Le Beyec, J. Chaumont and H. Bernas, Phys. Rev. Lett. **80** (1998) 5433–5436.

[21] D. A. Thompson, Journal of Applied Physics **52** (1981) 982–989.

[22] T. Aoki, J. Matsuo, G. Takaoka and I. Yamada, Nuclear Instruments and Methods in Physics Research Section B: Beam Interactions with Materials and Atoms **206** (2003) 861–865.

[23] I. Yamada, J. Matsuo, Z. Insepov, D. Takeuchi, M. Akizuki and N. Toyoda, Journal of Vacuum Science & Technology A: Vacuum, Surfaces, and Films **14** (1996) 781–785.

[24] N. Toyoda, S. Houzumi and I. Yamada, Nuclear Instruments and Methods in Physics Research Section B: Beam Interactions with Materials and Atoms **242** (2006) 466–468.

[25] K. Nakamura, S. Houzumi, N. Toyoda, K. Mochiji, T. Mitamura and I. Yamada, Nuclear Instruments and Methods in Physics Research Section B: Beam Interactions with Materials and Atoms **261** (2007) 660–663.

[26] Y. Yamamura and H. Tawara, Atomic Data and Nuclear Data Tables **62** (1996) 149–253.

[27] T. Aoki, J. Matsuo and G. Takaoka, Nuclear Instruments and Methods in Physics Research Section B: Beam Interactions with Materials and Atoms **202** (2003) 278–282.

[28] D. J. Oostra, R. P. van Ingen, A. Haring, A. E. de Vries and G. N. A. van Veen, Applied Physics Letters **50** (1987) 1506–1508.

[29] P. C. Zalm, Journal of Applied Physics **54** (1983) 2660–2666.

[30] M. Balooch, M. Moalem, W.-E. Wang and A. V. Hamza, Journal of Vacuum Science & Technology A: Vacuum, Surfaces, and Films **14** (1996) 229–233.

[31] R. Hill and P. Blenkinsopp, Applied Surface Science **231-232** (2004) 936 – 939.

[32] T. Aoki, T. Seki, J. Matsuo, Z. Insepov and I. Yamada, Nuclear Instruments and Methods in Physics Research Section B: Beam Interactions with Materials and Atoms **153** (1999) 264–269.

[33] Y. Iida, H. Okabayashi and K. Suzuki, Japanese Journal of Applied Physics **16** (1977) 1313–1318.

[34] H. Dong and T. Bell, Surface and Coatings Technology **111** (1999) 29–40.

[35] W. E. Vanderlinde and A. L. Ruoff, Journal of Vacuum Science & Technology B: Microelectronics and Nanometer Structures **6** (1988) 1621–1625.

[36] J. Cheng, A. Wucher and N. Winograd, The Journal of Physical Chemistry B **110** (2006) 8329–8336.

[37] C. Szakal, S. Sun, A. Wucher and N. Winograd, Applied surface science **231** (2004) 183–185.

[38] C. Mahoney, A. Fahey, G. Gillen, C. Xu and J. Batteas, Applied surface science **252** (2006) 6502–6505.

[39] C. Mahoney, Mass spectrometry reviews **29** (2010) 247–293.

[40] S. Ninomiya, Y. Nakata, K. Ichiki, T. Seki, T. Aoki and J. Matsuo, Nuclear Instruments and Methods in Physics Research Section B: Beam Interactions with Materials and Atoms **256** (2007) 493–496.

[41] S. Ninomiya, K. Ichiki, H. Yamada, Y. Nakata, T. Seki, T. Aoki and J. Matsuo, Rapid Communications in Mass Spectrometry **23** (2009) 1601–1606.

[42] K. Ichiki, S. Ninomiya, Y. Nakata, Y. Honda, T. Seki, T. Aoki and J. Matsuo, Applied Surface Science **255** (2008) 1148–1150.

[43] A. Delcorte, B. Garrison and K. Hamraoui, Analytical chemistry **81** (2009) 6676–6686.

[44] L. Rzeznik, R. Paruch, B. Czerwinski, B. Garrison and Z. Postawa, Vacuum **83, Supplement 1** (2009) S155 – S158.

[45] J. P. Thomas, P. E. Filpus-Luyckx, M. Fallavier and E. A. Schweikert, Phys. Rev. Lett. **55** (1985) 103–106.

[46] M. Benguerba, A. Brunelle, S. Della-Negra, J. Depauw, H. Joret, Y. L. Beyec, M. Blain, E. Schweikert, G. Assayag and P. Sudraud, Nuclear Instruments and Methods in Physics Research Section B: Beam Interactions with Materials and Atoms **62** (1991) 8 – 22.

[47] S. Ninomiya, T. Aoki, T. Seki and J. Matsuo, Applied surface science **252** (2006) 6550–6553.

[48] S. Akhunov, S. Morozov and U. Rasulev, Nuclear Instruments and Methods in Physics Research Section B: Beam Interactions with Materials and Atoms **203** (2003) 146 – 150, ¡ce:title¿14th International Workshop on Inelastic Ion-Surface Collisions¡/ce:title¿.

[49] A. Okano and K. Takayanagi, Applied Surface Science **127 窶?29** (1998) 362 – 367.

[50] A. Wucher and M. Wahl, Nuclear Instruments and Methods in Physics Research Section B: Beam Interactions with Materials and Atoms **115** (1996) 581 – 589.

[51] J. Don E. Harrison and C. B. Delaplain, Journal of Applied Physics **47** (1976) 2252–2259.

[52] N. Winograd, D. E. H. Jr. and B. J. Garrison, Surface Science **78** (1978) 467 – 477.

[53] R. Heinrich and A. Wucher, Nuclear Instruments and Methods in Physics Research Section B: Beam Interactions with Materials and Atoms **207** (2003) 136 – 144.

[54] T. Muramoto, M. Okai, Y. Yamashita, K. Yorizane and Y. Yamamura, Nuclear Instruments and Methods in Physics Research Section B: Beam Interactions with Materials and Atoms **180** (2001) 222 – 229.

[55] S. Morozov and U. Rasulev, Nuclear Instruments and Methods in Physics Research Section B: Beam Interactions with Materials and Atoms **258** (2007) 238 – 241.

[56] A. Okano and K. Takayanagi, Applied Surface Science **127-129** (1998) 362 – 367.

[57] A. Bulgakov, I. Ozerov and W. Marine, Applied Physics A: Materials Science & Processing **79** (2004) 1591–1594.

[58] N. Ray, P. Rajasekar, P. Chakraborty and S. Dey, Surface Science **301** (1994) 337 – 345.

[59] M. J. Vasile, Phys. Rev. B **29** (1984) 3785–3794.

[60] P. Mazarov, A. Samartsev and A. Wucher, Applied Surface Science **252** (2006) 6452 – 6455.

[61] S. Sun, C. Szakal, N. Winograd and A. Wucher, Journal of the American Society for Mass Spectrometry **16** (2005) 1677–1686.

[62] G. Nagy, L. Gelb and A. Walker, Journal of the American Society for Mass Spectrometry **16** (2005) 733–742.

[63] K. Moritani, M. Hashinokuchi, J. Nakagawa, T. Kashiwagi, N. Toyoda and K. Mochiji, Applied Surface Science **255** (2008) 948–950.

[64] K. ichi Shirai, Y. ji Fujiwara, R. Takahashi, N. Toyoda, S. Matsui, T. Mitamura, M. Terasawa and I. Yamada, Japanese Journal of Applied Physics **41** (2002) 4291–4294.

[65] N. Toyoda, N. Hagiwara, J. Matsuo and I. Yamada, Nuclear Instruments and Methods in Physics Research Section B: Beam Interactions with Materials and Atoms **161-163** (2000) 980 – 985.

[66] Y. Yamamoto, K. Ichiki, S. Ninomiya, T. Seki, T. Aoki and J. Matsuo, in *AIP Conference Proceedings* (PUBLISHER, ADDRESS, 2011), Vol. 1321, p. 298.

[67] N. Mine, B. Douhard, J. Brison and L. Houssiau, Rapid Communications in Mass Spectrometry **21** (2007) 2680–2684.

[68] H.-G. Cramer, T. Grehl, F. Kollmer, R. Moellers, E. Niehuis and D. Rading, Applied Surface Science **255** (2008) 966 – 969.

[69] M. Hada, S. Ibuki, Y. Hontani, Y. Yamamoto, K. Ichiki, S. Ninomiya, T. Seki, T. Aoki and J. Matsuo, Journal of Applied Physics **110** (2011) 094701–094701.

[70] M. Hada, S. Ninomiya, T. Seki, T. Aoki and J. Matsuo, Surface and Interface Analysis **43** (2011) 84–87.

[71] Y. Nakata, Y. Honda, S. Ninomiya, T. Seki, T. Aoki and J. Matsuo, Journal of Mass Spectrometry **44** (2009) 128–136.

[72] M. Bailey, B. Jones, S. Hinder, J. Watts, S. Bleay and R. Webb, Nuclear Instruments and Methods in Physics Research Section B: Beam Interactions with Materials and Atoms **268** (2010) 1929–1932.

[73] A. Shard, P. Brewer, F. Green and I. Gilmore, Surface and interface analysis **39** (2007) 294–298.

[74] W. Chen, Y. Ling, B. Chen, H. Shih and C. Cheng, Applied surface science **252** (2006) 6594–6596.

[75] S. Ninomiya, K. Ichiki, H. Yamada, Y. Nakata, T. Seki, T. Aoki and J. Matsuo, Surface and Interface Analysis **43** (2011) 221–224.

[76] I. Yamada, J. Matsuo, Z. Insepov, T. Aoki, T. Seki and N. Toyoda, Nuclear Instruments and Methods in Physics Research Section B: Beam Interactions with Materials and Atoms **164** (2000) 944–959.

[77] C. Kim, A. Kubota and D. Economou, Journal of Applied Physics **86** (1999) 6758.

[78] N. Toyoda, H. Kitani, N. Hagiwara, T. Aoki, J. Matsuo and I. Yamada, Materials Chemistry and Physics **54** (1998) 262 – 265.

[79] S. Kakuta, S. Sasaki, T. Hirano, K. Ueda, T. Seki, S. Ninomiya, M. Hada and J. Matsuo, Nuclear Instruments and Methods in Physics Research Section B: Beam Interactions with Materials and Atoms **257** (2007) 677–682.

[80] X. Li, W. Goodhue, C. Santeufeimio, T. Tetreault, R. MacCrimmon, L. Allen, D. Bliss, K. Krishnaswami and C. Sung, Applied surface science **218** (2003) 251–258.

[81] J. Song, D. Choi and W. Choi, Nuclear Instruments and Methods in Physics Research Section B: Beam Interactions with Materials and Atoms **196** (2002) 275–278.

[82] Z. Postawa, B. Czerwinski, M. Szewczyk, E. Smiley, N. Winograd and B. Garrison, The Journal of Physical Chemistry B **108** (2004) 7831–7838.

[83] T. Aoki, T. Seki and J. Matsuo, Vacuum **84** (2010) 994 – 998.

[84] L. Allen, Z. Insepov, D. Fenner, C. Santeufemio, W. Brooks, K. Jones and I. Yamada, Journal of applied physics **92** (2002) 3671.

[85] T. Aoki, J. Matsuo and I. Yamada, Nuclear Instruments and Methods in Physics Research Section B: Beam Interactions with Materials and Atoms **180** (2001) 164–170.

[86] Z. Insepov, R. Manory, J. Matsuo and I. Yamada, Physical Review B **61** (2000) 8744.

[87] T. Seki and J. Matsuo, Nuclear Instruments and Methods in Physics Research Section B: Beam Interactions with Materials and Atoms **241** (2005) 604 – 608.

[88] N. Toyoda, Y. Maeshima and I. Yamada, Nuclear Instruments and Methods in Physics Research Section B: Beam Interactions with Materials and Atoms **257** (2007) 662 – 665.

List of Publications

Publications

1. S. Ninomiya, K. Ichiki, H. Yamada, Y. Nakata, T. Seki, T. Aoki, J. Matsuo “Analysis of organic semiconductor multilayers with Ar cluster secondary ion mass spectrometry” Surface and Interface Analysis Vol. 43[1-2],(2011) pp.95-98

2. S. Ninomiya, K. Ichiki, H. Yamada, Y. Nakata, T. Seki, T. Aoki, J. Matsuo “The effect of incident energy on molecular depth profiling of polymers with large Ar cluster ion beams” Surface and Interface Analysis Vol. 43[1-2],(2011) pp.221-224

3. K. Ichiki, S. Ninomiya, Y. Nakata, H. Yamada, T. Seki, T. Aoki, J. Matsuo “Surface morphology of PMMA surfaces bombarded with size-selected gas cluster ion beams” Surface and Interface Analysis Vol. 43[1-2] (2011) pp. 120-122

4. M. Hada, K. Ichikiand J. Matsuo “Characterization of vapor-deposited L-leucine nanofilm” Thin Solid Films 519, (2011) pp.1993-1997

5. S. Ninomiya, K. Ichiki, H. Yamada, Y. Nakata, T. Seki, T. Aoki, J. Matsuo “SIMS Depth Profiling of Organic Materials with Ar Cluster Ion Beam”, Transactions of the MRS-J 35 [4] (2010) pp. 785-788

6. K. Ichiki, S. Ninomiya, T. Seki, T. Aoki, J. Matsuo “Sputtering Properties of Si by Size-Selected Ar Gas Cluster Ion Beam” Transactions of the MRS-J 35 [4] (2010) pp. 789-792

7. H. Yamada, K. Ichiki, Y. Nakata, S. Ninomiya, T. Seki, T. Aoki, J. Matsuo, “Processing Techniques of Biomaterials: Using Gas Cluster Ion Beam for Imaging Mass Spectrometry” Transactions of the MRS-J 35 [4] (2010) pp. 793-796

8. M. Hada, Y. Hontani, S. Ibuki, K. Ichiki, S. Ninomiya, T. Seki, T. Aoki and J. Matsuo “Evaluation of Surface Damage of Organic Films

due to Irradiation with Energetic Ion Beams" AIP Conference Proceedings Vol. 1321 (IIT2010), (2010) pp. 314-316

9. K. Ichiki, S. Ninomiya, T. Seki, T. Aoki, and J. Matsuo "Energy Effects on the Sputtering Yield of Si Bombarded with Gas Cluster Ion Beams" AIP Conference Proceedings Vol. 1321 (IIT2010) , (2010) pp. 294-297

10. Y. Yamamoto, K. Ichiki, S. Ninomiya, T. Seki, T. Aoki and J. Matsuo "Evaluation of surface damage on organic materials irradiated with Ar cluster ion beam" AIP Conference Proceedings Vol. 1321 (IIT2010) , (2010) pp. 298-301

11. J. Matsuo, S. Ninomiya, H. Yamada, K. Ichiki, Y. Wakamatsu, M. Hada, T. Seki and T. Aoki "SIMS with highly excited primary beams for molecular depth profiling and imaging for organic and biological materials" Surface and Interface Analysis Vol. 42 [10-11], (2010) pp. 1612-1615

12. H. Yamada, K. Ichiki, Y. Nakata, S. Ninomiya, T. Seki, T. Aoki and J. Matsuo "MeV-Energy Probe SIMS Imaging of Major Components in Animal Cells Etched Using Large Gas Cluster Ions" Nuclear Instruments and Methods in Physics Research B, 268, (2010) pp. 1736-1740

13. K. Ichiki, S. Ninomiya, T. Seki, T. Aoki and J. Matsuo "Sputtering Yield Measurements with Size-selected Gas Cluster Ion Beams" MRS Symposium Proceedings (2009 MRS Spring Meetings)

14. S. Ninomiya, K. Ichiki, H. Yamada, Y. Nakata, T. Seki, T. Aoki and J. Matsuo "Molecular depth profiling of multilayer structures of organic semiconductor materials by secondary ion massspectrometry with large argon cluster ion beams" Rapid Communications in Mass Spectrometry, 23, (2009) pp. 3264-3268

15. S. Ninomiya, K. Ichiki, T. Seki, T. Aoki, J. Matsuo, "The emission process of secondary ions from solids bombarded with large gas cluster ions" Nuclear Instruments and Methods in Physics Research B, 267,(2009) pp. 2601-2604,

16. H. Yamada, K. Ichiki, Y. Nakata, S. Ninomiya, T. Seki, T. Aoki and J. Matsuo, "A Processing Technique for Cell Surfaces Using Gas Cluster Ions for Imaging Mass Spectrometry" Journal of the Mass Spectrometry Society of Japan vol. 57, No. 3 (2009) pp.117-121,

17. S. Ninomiya, K. Ichiki, H. Yamada, Y. Nakata, T. Seki, T. Aoki, J. Matsuo "Precise and fast secondary ion mass spectrometry depth profiling of polymer materials with large Ar cluster ion beams" Rapid Communications in Mass Spectrometry, Vol.23, (2009) pp.1601-1606

18. S. Ninomiya, K. Ichiki, H. Yamada, Y. Nakata, T. Seki, T. Aoki and J. Matsuo "Low Damage Etching of Polymer Materials for Depth Profile Analysis Using Large Ar Cluster Ion Beam" Journal of Surface Analysis Vol.15, No.3, (2009) pp.275-278

19. J. Matsuo, S. Ninomiya, Y. Nakata, Y. Honda, K. Ichiki, T. Seki and T. Aoki "What size of cluster is most appropriate for SIMS?" Applied Surface Science 255, (2008) pp.1235-1238

20. S. Ninomiya, K. Ichiki, Y. Nakata, Y. Honda, T. Seki, T. Aoki and J. Matsuo "Secondary ion emission from Si bombarded with large Ar cluster ions under UHV conditions" Applied Surface Science 255, (2008) pp 880-882

21. K. Ichiki, S. Ninomiya, Y. Nakata, Y. Honda, T. Seki, T. Aoki and J. Matsuo "High sputtering yields of organic compounds by large gas cluster ions" Applied Surface Science 255, (2008) pp 1148-1150

22. S. Ninomiya, Y. Nakata, Y. Honda, K. Ichiki, T. Seki, T. Aoki and J. Matsuo, "A Fragment-free ionization technique for organic mass spectrometry with large Ar cluster ions" Applied Surface Science 255, (2008) pp 1588-1590

23. S. Ninomiya, J. Matsuo, K. Ichiki, H. Yamada, Y. Nakata, Y. Honda, T. Seki and T. Aoki "Low Damage Etching and SIMS Depth Profiling with Large Ar Cluster Ions" Transactions of the MRS-J 33 [4] (2008) pp.1043-1046

24. S. Ninomiya, K. Ichiki, Y. Nakata, T. Seki, T. Aoki and J. Matsuo "The Effect of Incident Cluster Ion Size on Secondary Ion Yields Produced from Si" Transactions of the MRS-J 32 [4] (2007) pp.895-898

25. J. Matsuo, S. Ninomiya, Y. Nakata, K. Ichiki, T. Aoki, T. Seki "Size effect in cluster collision on solid surfaces" Nuclear Instruments and Methods in Physics Research B 257 (2007) 627-631

26. S. Ninomiya, K. Ichiki, Y. Nakata, T. Seki, T. Aoki, J. Matsuo "The effect of incident cluster ion energy and size on secondary ion yields emitted from Si" Nuclear Instruments and Methods in Physics Research B, 256 (2007)pp. 528-531

27. S. Ninomiya, Y. Nakata, K. Ichiki, T. Seki, T. Aoki, and J. Matsuo, "Measurements of secondary ions emitted from organic compounds bombarded with large gas cluster ions", Nuclear Instruments and Methods in Physics Research B, 256 (2007)pp. 493-496

28. K. Ichiki, S. Ninomiya, T. Seki, T. Aoki, and J. Matsuo, "Surface oxidation of Si assisted by irradiation with large gas cluster ion beam in an oxygen atmosphere", Nuclear Instruments and Methods in Physics Research B, 256 (2007) pp. 350-353

International Conference

1. K. Ichiki, T. Seki, T. Aoki and J. Matsuo "The effects of cluster size and energy on sputtering with gas cluster ion beams" E-MRS 2011 Spring Meeting (Nice, France, 2011/5/9, Poster)

2. K. Ichiki, S. Ninomiya, T. Seki, T. Aoki and J. Matsuo "The effects of cluster size on sputtering and surface smoothing with gas cluster ion beams" 20th MRS-J Symposium (International Session) (Yokohama, Japan, 2010/12/22, Poster)

3. K. Ichiki, S. Ninomiya, T. Seki, T. Aoki and J. Matsuo "The effects of cluster size and energy on surface smoothing with gas cluster ion beams" 17th International Conference on Ion Beam Modification of Materials (IBMM2010), (Montreal, Canada, 2010/8/23, Poster)

4. K. Ichiki, S. Ninomiya, T. Seki, T. Aoki and J. Matsuo "The effects of incident cluster size and energy on Si sputtering yield" 10th Workshop on Cluster Ion Beam Technology (Kyoto, Japan, 2010/6/14, Oral)

5. K. Ichiki, S. Ninomiya, T. Seki, T. Aoki and J. Matsuo "Size and energy dependence of the sputtering yield of Si bombarded with gas cluster ion beams" 18th International Conference on Ion Implantation Technology (Kyoto University, Japan, 2010/6/7, Poster)

6. K. Ichiki, S. Ninomiya, Y. Nakata, H. Yamada, T. Seki, T. Aoki and J. Matsuo "Sputtering and morphology of solid surfaces bombarded with size-selected gas cluster ion beams" 16th International Conference on Surface Modification of Materials by Ion Beams (SMMIB2009) (AIST Tokyo Waterfront, Japan, 2009/9/16, Oral)

7. K. Ichiki, S. Ninomiya, T. Seki, T. Aoki and J. Matsuo "Size effects of sputtering yields with large cluster ion beams" 17th International

Conference on Secondary Ion Mass Spectrometry (Toronto, Canada, 2009/9/14, Poster)

8. K. Ichiki, S. Ninomiya, M. Hada, T. Seki, T. Aoki and J. Matsuo "Sputtering yield measurement with size-selected gas cluster ion beams" 2009 MRS spring meeting (San Francisco, CA, 2009/4/16, Poster)

9. K. Ichiki, S. Ninomiya, T. Seki, T. Aoki and J. Matsuo "Size-selected High Density Large Gas Cluster Ion Beam Irradiation" The IUMRS International Conference in Asia (Nagoya Congress Center, Japan, 2008/12/11, Poster)

10. K. Ichiki, S. Ninomiya, Y. Nakata, Y. Honda, T. Seki, T. Aoki and J. Matsuo, "High sputtering yields of organic compounds by large gas cluster ions" The 16th International Conference on Secondary Ion Mass Spectrometry(Kanazawa, Japan, 2007/10/29-11/2)

11. K. Ichiki, S. Ninomiya, T. Seki, T. Aoki and J. Matsuo, "Nonlinear effects of secondary ion yields emitted from Si by Ar cluster ion beam irradiation" The 16th International Conference on Secondary Ion Mass Spectrometry(Kanazawa, Japan, 2007/10/29-11/2)

12. K. Ichiki, S. Ninomiya, T. Seki, T. Aoki and J. Matsuo, "Surface oxidation of Si assisted by irradiation with large gas cluster ion beam in an oxygen atmosphere", 22nd International Conference on Atomic Collisions in Solids, (Berlin, Germany, 2006/7/21-26).

Awards

1. Award for Encouragement of Research
The IUMRS International Conference in Asia 2008, Nagoya, Japan, November 2008.

2. Surface Science Western SIMS Research Award for Poster
The 17th International Conference on Secondary Ion Mass Spectrometry, Toronto, Canada, September 2009.

3. Award for Encouragement of Research
20th Symposium of Material Research Society of Japan,Tokyo, Japan, December 2010.